FLUID TRANSPORT PHENOMENA IN FIBROUS MATERIALS

N. Pan and W. Zhong

doi:10.1533/tepr.2006.0002

Abstract: Fluid transport is one of the most frequently observed phenomena in the processing and end uses of fibrous materials. Fibrous materials have a unique structure of complex geometry, characterized by system anisotropy and heterogeneity. The characterization of fibrous materials, therefore, is critical in the understanding of transport behavior through fibrous structures, and is discussed after an introductory section. Subsequent sections cover topics of various transport processes through fibrous structures, including wicking and wetting, resin impregnation in liquid composite molding, filtration and separation in geotextiles, aerosol filtration in fibrous filters, micro/nano scale transport phenomena, and biomedical applications. The fibrous structure is also known for its multi-scale pore distribution from intra-fiber to inter-fiber spaces. This multi-scale effect is even more prominent when micro or nano fibrous materials are concerned, and so multi-scale approaches to address the scale effects of transport behavior in fibrous materials are discussed. Finally, the Ising model of statistical mechanics, a robust computer-simulation tool dealing with the fluid transport problems in fibrous materials, is introduced.

Key words: Transport, fibrous materials, structure characterization, wetting, multi-scale, Ising model.

1. INTRODUCTION

Transport study had its origin from astrophysics which, in the late 19th century dealt with light diffusion by the atmosphere [1, 2]. The work expanded into the larger scope of radiation transfer from a star through the atmosphere, formulated into what is known as the transport equation of Boltzmann in the early part of 20th century [3]. Transport phenomena were defined in [3] as the interactions and changes in the properties and states of a particle when it is passing through a medium. By substituting the particle with any concrete object concerned in practical problems, one can enable the theory to be applicable in tackling such issues as diffusion, permeation, and spreading widely existed in biology, chemistry, physics and engineering processes, as documented in numerous books [3–12].

When a fibrous material serves as the medium, and air, moisture, physical or biological entities or heat and even various rays (in a quantum sense) [13, 14] as the particle moving through the fibrous medium, the significance of the transport theories in understanding these fundamental issues becomes instantly self-evident.

In general, study of liquid transport phenomenon in fibrous materials deals with a wide array of issues; most of them are complex and intricate and still inadequately

understood. For instance, air and fiber react differently with liquids, so a wetting process in a fibrous material cannot proceed uniformly. Likewise, since liquid molecules are trapped by the air and fiber in different mechanisms, they evaporate in a non-uniform ways as well.

Next, when a material absorbs moisture, several things can happen. First the material will release heat which will inevitably interact with the moisture; second, a moistened material will often swell, leading to a change of material dimensions which in turn will alter the internal structure of the material. Moistened air and fiber exhibit distinctive changes in their behaviors, leading to drastically different overall material properties.

What can be transported in a fibrous system may include heat, fluids or solids, as in filtering processes, or even magnetic waves as mentioned above. Furthermore, the geometrical or topological structure of a fibrous material is, in general, highly intricate; even more complex is that the material structure is highly susceptible to external actions, be they mechanical or otherwise.

This monograph consists of eight main sections including this one serving as an introduction. As mentioned above, fibrous materials have a unique structure of complex geometry, typified by system anisotropy and heterogeneity. The characterization of fibrous materials, is therefore, critical for understanding transport behavior through fibrous structures, and is discussed in Section 2.

Sections 3 to 7 cover topics of various transport processes through fibrous structures, namely:

3 Wetting and wicking
4 Resin impregnation in liquid composite molding
5 Filtration and separation in geotextiles
6 Aerosol filtration by fibrous filters
7 Micro/nano-scale transport phenomena in fibrous structures: biomedical applications

Heat and moisture transfer behavior through fibrous materials, as thoroughly reviewed by an earlier issue of *Textile Progress* (Vol. 31, No. 1–2, *The Science of Clothing Comfort*, by Y. Li), will not be discussed in the present review.

Another example of the complexity is the multi-scale nature usually involved in practical problems, and the fibrous structure is also known for its vast range of pore distribution from intra-fiber to inter fiber spaces. Figure 1 shows the different structure levels when tackling the problem of clothing comfort; different approaches have to be taken corresponding to different scales for the mechanisms of the transport dependent on the scale [15, 16]. This multi-scale effect is even more prominent when micro or nano fibrous materials are concerned and consequently Section 8 addresses the scale effects of transport behavior using statistical physics approaches in fibrous materials.

2. CHARACTERIZATION OF FIBROUS MATERIALS

Even for fibrous materials made of identical fibers, i.e. the same geometrical shapes and dimensions and physical properties, the pores formed inside the materials will exhibit huge complexities in terms of the sizes, shapes and the capillary geometries. The pores will even change as the material interacts with fluids or heat during the

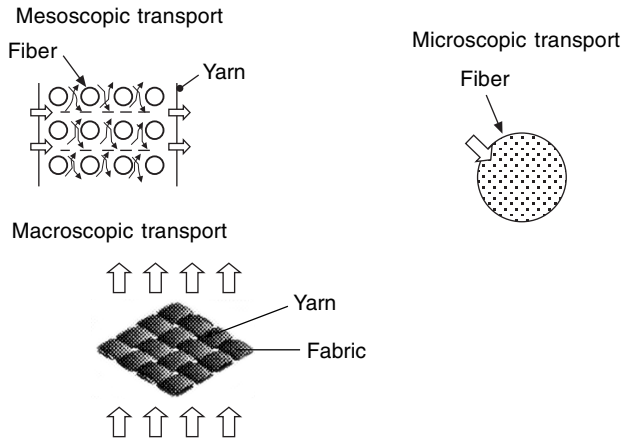

Fig. 1 Different structure levels in clothing modeling [16]

transport process; fibers swell and the material deforms due to the weight of the liquid absorbed.

Such a tremendous complexity inevitably calls for statistical or probabilistic approaches in description of the internal structural characteristics, such as the pore size distributions, as a prerequisite for studying the transport phenomena of the material.

2.1 Description of the Internal Structures of Fibrous Materials

Fibrous materials are essentially collections of individual fibers assembled via frictions into more or less integrated structures. Any external stimulus on such a system has to be transmitted between fibers through either the fiber contacts or/and the medium filling the pores formed by the fibers. As a result, a thorough understanding and description of the internal structure becomes indispensable in any serious attempt to study the system. In other words, the issue of structure versus property remains just as critical as in, say, polymers with complex internal structures, only differing in scale.

2.2 Characterization of the Geometric Structures of Fibrous Materials

Three fundamental parameters or features are required to specify a fibrous material.

2.2.1 Fiber Aspect Ratio, S

Fiber aspect ratio is defined as the fiber length l_f versus its radius r_f, an indicator of the slenderness of the fiber and one of the key variables in describing a fibrous material:

$$S = \frac{l_f}{r_f} \tag{1}$$

Obviously, for a fiber the value of the radius has to be small, usually measured in 10^{-6} m for textile fibers.

2.2.2 Total Fiber Amount – The Fiber Volume Fraction, V_f

For any mixture, the relative proportion of each constituent is the most essential information. There are several ways to specify the proportions including fractions or percentages by weight or by volume.

For practical purpose, weight fraction is most straightforward. For a mixture of n components, the weigh fraction W_i for component i (= 1, 2, …, n) is defined as

$$W_i = \frac{M_i}{M_t} \tag{2}$$

where M_i is the net weight of the component i, and M_t is the total weight of the mixture.

However, it is the volume fraction that is most often used in analysis, which can be readily calculated once the corresponding weight fractions M_i and M_t, and the corresponding densities ρ_i and ρ_t are known.

$$V_i = \frac{(M_i/\rho_i)}{(M_t/\rho_t)} = \frac{M_i}{M_t}\frac{\rho_t}{\rho_i} = W_i\frac{\rho_t}{\rho_i} \tag{3}$$

For a fibrous material consisting of fiber and air, it should be noted that although the weight fraction of the air is small, its volume fraction is not, due to its low density.

2.2.3 Fiber Arrangement – The Orientation Probability Density Function

Various analytic attempts have been made to characterize the fiber orientations in fibrous materials. There are three groups of slightly different approaches, according to the specific materials being dealt with.

The first group is aimed at paper sheets. The generally acknowledged pioneer in this area is Cox. In his report [17], he tried to predict the elastic behavior of paper (a bonded planar fiber network) based on the distribution and mechanical properties of the constituent fibers. Kallmes [18–22] and Page [23–35] have contributed a great deal to this field through their research work on properties of paper. They extended Cox's analysis by using probability theory to study fiber bonding points, the free fiber lengths between the contacts, and their distributions. Perkins [36–41] applied micromechanics to paper sheet analysis. Dodson *et al*. [42–53] tackled the problems by a more mathematical statistics route.

Another group focused on general fiber assemblies, mainly textiles and other fibrous products. Van Wyk [54] was probably among the first to study the mechanical properties of a textile fiber mass by looking into the microstructural units in the system, establishing the widely applied compression formula. A more complete work in this aspect, however, was carried out by Komori and his colleagues [55–60]. Through a series of papers, they predicted the mean number of fiber contact points and the mean fiber lengths between contacts [56, 59, 60], the fiber orientations [57] and the pore size distributions [59] of the fiber assemblies. Their results have broadened our understanding of fibrous systems and provided new means for further research work on the properties of fibrous assemblies. Several papers have since followed, more or less based on their results, to deal with the mechanics of fiber assemblies. Lee and Lee [61] and Duckett and Chen [62, 63] further developed the theories on the compressional properties [63, 64]. Carnaby and Pan studied the fiber slippage and the

compressional hysteresis [65] and shear properties [66]. Pan also discussed the effects of the so called 'steric hinge' [67] and the fiber blend [68]. A more comprehensive mechanical model has been proposed by Narter *et al.* [69].

The third group is mainly concerned with fiber-reinforced composite materials. Depending on the specific cases, either of the two approaches discussed above may be chosen, with modification to better fit the problems [70–73].

Since the discussion on fiber orientation requires some of the concepts below, more specific information in this topic is provided in Section 2.3, after the introduction of an analytical approach to characterize the internal geometrical and structural details.

Although Komori and Makishima's results [59, 60] are adopted hereafter, we need to caution that their results are valid only for very loose structures, for as the fiber contact density increases, the effects of the steric hinge have to be accounted for to reflect the fact that the contact probability changes with the number of fibers involved [67, 74].

2.2.4 Characterization of the Internal Structure of a Fibrous Material

A general fibrous structure is illustrated in Fig. 2. We assume that all the properties of such a system are determined collectively by the fiber–fiber contacts, free fiber segments between the fiber contact points, and the volume fractions of fibers and voids in the structure. Therefore, attention has to be focused first on the characterization of the density and distribution of the contact points and the free fiber segment between two contacts on a fiber in the system of given volume V.

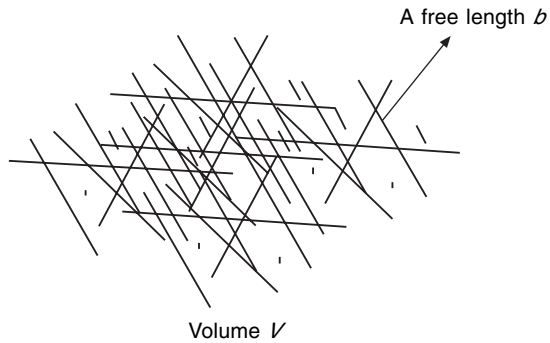

Fig. 2 General illustration of a fibrous material

According to the approach explored by Komori and Makishima in [59, 60], let us first set a Cartesian coordinate system X_1, X_2, X_3 in a fibrous structure, and let the angle between the X_3 axis and the axis of an arbitrary fiber be θ, and that between the X_1 axis and the normal projection of the fiber axis onto the X_1X_2 plane be ϕ. Then the orientation of any fiber can be defined uniquely by a pair (θ, ϕ), provided that $0 \leq \theta \leq \pi$ and $0 \leq \phi \leq \pi$, as shown in Fig. 3.

Suppose the probability of finding the orientation of a fiber in the infinitesimal range of angles $\theta \sim \theta + d\theta$ and $\theta \sim \phi + d\phi$ is $\Omega(\theta, \phi) \sin \theta d\theta d\phi$, where $\Omega(\theta, \phi)$ is the still unknown density function of fiber orientation and $\sin \theta$ is the Jacobian of the vector of the direction cosines corresponding to θ and ϕ. The following normalization condition must be satisfied

 doi:10.1533/tepr.2006.0002

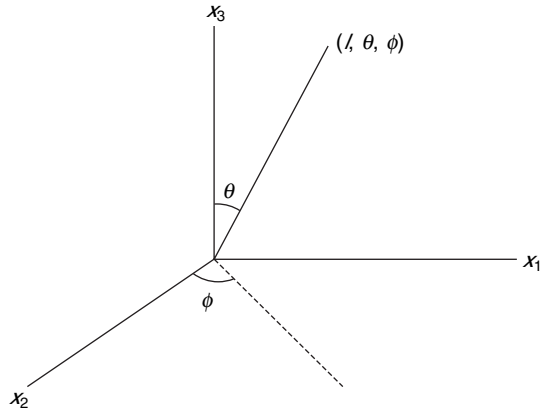

Fig. 3 Coordinates of a fiber in the system

$$\int_0^{\pi} d\theta \int_0^{\pi} d\phi \Omega(\theta, \phi) \sin\theta = 1$$

Assume there are N fibers of straight cylinders of diameter $D = 2r_f$ and length l_f in the fibrous system of volume V. According to the analysis in [60], the average number of contacts on an arbitrary fiber, $\overline{n}$, can be expressed as

$$\overline{n} = \frac{2DNl_f^2}{V} I \tag{4}$$

where I is a factor reflecting the fiber orientation and is defined as

$$I = \int_0^{\pi} d\theta \int_0^{\pi} d\phi J(\theta, \phi) \Omega(\theta, \phi) \sin\theta \tag{5}$$

where

$$J(\theta, \phi) = \int_0^{\pi} d\theta' \int_0^{\pi} d\phi' \Omega(\theta', \phi') \sin\chi(\theta, \phi, \theta', \phi') \sin\theta' \tag{6}$$

and

$$\sin\chi = [1 - (\cos\theta\cos\theta' + \sin\theta\sin\theta'\cos(\phi - \phi'))^2]^{\frac{1}{2}} \tag{7}$$

is the angle between the two arbitrary fibers. The mean number of fiber contact points per unit fiber length has been derived as

$$n_l = \frac{\overline{n}}{l_f} = \frac{2DNl_f}{V} I = \frac{2DL}{V} I \tag{8}$$

where $L = Nl_f$ is the total fiber length within the volume V. This equation can be further reduced to

$$n_l = \frac{2DL}{V} I = \frac{\pi D^2 L}{4V} \frac{8I}{\pi D} = 8I \frac{V_f}{\pi D} \tag{9}$$

where $V_f = \frac{\pi D^2 L}{4V}$ is the fiber volume fraction and usually a given parameter. It is seen from the result that the parameter I can be considered as an indicator of the density of contact points. The reciprocal of n_l is the mean length $\bar{b}$ between the two neighboring contact points on the fiber, i.e.

$$\bar{b} = \frac{\pi D}{8IV_f} \tag{10}$$

The total number of contacts in a fiber assembly containing N fibers is then given by

$$n = \frac{N}{2}\bar{n} = \frac{DL^2}{V} I \tag{11}$$

The factor $\frac{1}{2}$ was introduced to avoid the double counting of one contact. Clearly these predicted results are the basic microstructural parameters and the indispensable variables for studying any macrostructural properties of a fibrous system.

2.2.5 Fiber Distribution Uniformity – The Pore Distributions

2.2.5.1 Mathematical Description of the Anisotropy of Fibrous Materials

As demonstrated above, the fiber contacts and pores in a fibrous materials are entirely dependent on the way fibers are put together.

Let us cut a representative element of unit volume from a general fibrous material in such a way that this element possesses the identical system properties, for example the fiber volume fraction V_f. However, because of the anisotropic and heterogeneous nature of the material, other properties will vary at different directions and locations of the element.

Consider on the representative element a cross section of unit area, with direction (Θ, Φ) as in Fig. 4. Here we assume all fibers are identical, with length l_f and radius r_f. If we ignore the contribution of air in the pores, the properties of the material in any given direction are then determined completely by the amount of fiber involved in that particular direction. Since for an isotropic material the number of fibers at any direction should be the same, the anisotropy of the material structure is hence reflected

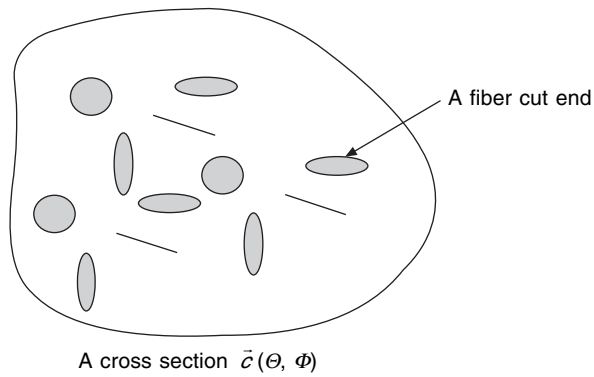

Fig. 4 Cross section with direction (Θ, Φ)

by the fact that at different directions of the material, the number of fibers involved is a function of the direction, and possesses different values.

Let us designate the number of fibers traveling through a cross section of direction (Θ, Φ) as $\Psi(\Theta, \Phi)$. This variable, by definition, has to be proportionally related to the fiber orientation *pdf* in the same direction [71], i.e.

$$\Psi(\Theta, \Phi) = N\Omega(\Theta, \Phi) \tag{12}$$

where N is a coefficient. This equation, in fact, establishes the connection between the properties on a cross section and the fiber orientation. The total number of fibers contained in the unit volume can be obtained by integrating the above equation over the possible directions of all the cross sections of the volume to give

$$\int_{\Psi} \Psi(\Theta, \Phi)\, d\Psi(\Theta, \Phi) = \int_0^{\pi} d\Theta \int_0^{\pi} d\Phi\, N\Omega(\Theta, \Phi) \sin\Theta = N \tag{13}$$

That is, the constant N actually represents the total number of fibers contained in the unit volume, and is related to the system fiber volume fraction V_f by the expression

$$N = \frac{V_f}{\pi r_f^2 l_f} \tag{14}$$

Then, on the given cross section (Θ, Φ) of unit area, the average number of cut ends of the fibers having their orientations in the range of $\theta \sim \theta + d\theta$ and $\phi \sim \phi + d\phi$ is given, following Komori and Makishima [59], as

$$d\Psi = \Psi(\Theta, \Phi) l_f \mid \cos\chi \mid \Omega(\theta, \phi) \sin\theta d\theta d\phi \tag{15}$$

where, according to analytic geometry,

$$\cos\chi = \cos\Theta \cos\theta + \sin\Theta \sin\theta \cos(\phi - \Phi) \tag{16}$$

with χ being the angle between the directions (Θ, Φ) and (θ, ϕ). Since the area of a single cut fiber end at the cross section (Θ, Φ), ∇S, can be derived as

$$\nabla S = \frac{\pi r_f^2}{|\cos\chi|}, \tag{17}$$

the total area S of the cut fiber ends of all possible orientations on the cross section can be calculated as

$$\begin{aligned} S(\Theta, \Phi) &= \int_0^{\pi} d\theta \int_0^{\pi} d\phi \times \nabla S \times d\Psi \times \Omega(\theta, \phi) \sin\theta \\ &= \Psi(\Theta, \Phi) \int_0^{\pi} d\theta \int_0^{\pi} d\phi \pi r_f^2 l_f \Omega(\theta, \phi) \sin\theta = \Omega(\Theta, \Phi) N \pi r_f^2 l_f \end{aligned} \tag{18}$$

As $S(\Theta, \Phi)$ is in fact equal to the fiber area fraction on this cross section of unit area, i.e.

$$S(\Theta, \Phi) = A_f(\Theta, \Phi), \tag{19}$$

we can therefore find the relationship at a given direction (Θ, Φ) between the fiber area fraction and the fiber orientation *pdf* from Equations 18 and 19

$$A_f(\Theta, \Phi) = \Omega(\Theta, \Phi) N \pi r_f^2 l_f = \Omega(\Theta, \Phi) V_f \tag{20}$$

This relationship has two practical implications. First, it could provide a means to derive the fiber orientation *pdf*; at each cross section (Θ, Φ), once we obtain through experimental measurement the fiber area fraction, A_f (Θ, Φ), we can calculate the corresponding fiber orientation *pdf* $\Omega(\Theta, \Phi)$ for a given constant V_f. So a complete relationship of $\Omega(\Theta, \Phi)$ versus (Θ, Φ) can be established from which the overall fiber orientation *pdf* can be deduced. Note that a fiber orientation *pdf* is by definition the function of direction only. Secondly, it shows in Equation 20 that the only case where $A_f = V_f$ is when the density function $\Omega(\Theta, \Phi) = 1$; this happens only in an assembly made of fibers unidirectionally oriented at direction (Θ, Φ). In other words, the difference between the fiber area and volume fractions is caused by fiber misorientation.

The pore area fraction on the other hand can be calculated as

$$A_p(\Theta, \Phi) = 1 - A_f(\Theta, \Phi) = 1 - V_f \Omega(\Theta, \Phi) \tag{21}$$

In addition, the average number of fiber cut ends on the plane, $\nu(\Theta, \Phi)$, is given as

$$\begin{aligned} \nu(\Theta, \Phi) &= \int_0^{\pi} d\theta \int_0^{\pi} d\phi \times d\Psi \times \Omega(\theta, \phi) \sin\theta \\ &= N\Omega(\Theta, \Phi) l_f \int_0^{\pi} d\theta \int_0^{\pi} d\phi \, |\cos\chi| \, \Omega(\theta, \phi) \sin\theta \\ &= \frac{V_f}{\pi r_f^2} \Omega(\Theta, \Phi) \Upsilon(\Theta, \Phi) \end{aligned} \tag{22}$$

where

$$\Upsilon(\Theta, \Phi) = \int_0^{\pi} d\theta \int_0^{\pi} d\phi \, |\cos\chi| \, \Omega(\theta, \phi) \sin\theta \tag{23}$$

is the statistical mean value of $|\cos\chi|$.

Hence, the average radius of the fiber cut ends, $\rho(\Theta, \Phi)$, can be defined as

$$\rho(\Theta, \Phi) = \sqrt{\frac{S(\Theta, \Phi)}{\pi \nu(\Theta, \Phi)}} = r_f \sqrt{\frac{1}{\Upsilon(\Theta, \Phi)}} \tag{24}$$

Since $\Upsilon(\Theta, \Phi) \leq 1$, there is always $\rho(\Theta, \Phi) \geq r_f$.

All these variables, S, ν and ρ, are important indicators of the anisotropic nature of the fibrous structure, and they can be calculated once the fiber orientation *pdf* is given. Of course, the fiber area fraction can also be calculated using the mean number of the fiber cut ends and the mean radius from Equations 19 and 24, i.e.

$$A_f(\Theta, \Phi) = \nu(\Theta, \Phi) \, \pi\rho^2 (\Theta, \Phi) \tag{25}$$

It should be pointed out that all the parameters derived here are the statistical mean values at a given cross section. These parameters are useful therefore in calculating some overall system properties to reflect the anisotropy of the material behavior.

2.2.5.2 The Pore Distributions in Fibrous Materials

In all the previous studies on fibrous materials, the materials are assumed, explicitly or implicitly, to be quasi-homogeneous such that the relative proportions of the fiber and pores (the volume fractions) are constant throughout the system. This is to assume that fibers are uniformly spaced at every location in the material, and the distance between fibers and hence the space occupied by pores between fibers are identical throughout. Obviously this is a highly idealized situation. In practice, because of the inherent limits of processing techniques, the fibers, even at the same orientation, are rarely uniformly spaced in a fibrous material. Consequently, the local fiber/pore concentrations will vary from point to point, although the system fiber volume fraction V_f remains constant.

In many cases, if we only need to calculate the average properties at given directions, a knowledge of $A_f(\Theta, \Phi)$ alone will be adequate. However, in order to investigate local heterogeneity and to realistically predict other extreme properties, we have to look into the local variation of the fiber fraction or the distribution of the pores between fibers.

In general, the distribution of pores in fibrous material is not uniform, nor is it continuous, due to the existence of fibers. If we cut a cross section of the assembly, the areas occupied by the pores may vary from location to location. According to Ogston, [75] and Komori and Makishima [76], we can use the concept of the 'aperture circle' of various radii r, the maximum circle enclosed by fibers or the area occupied by the pores in between fibers, to describe the distribution of the pores on a cross section, as shown in Fig. 5.

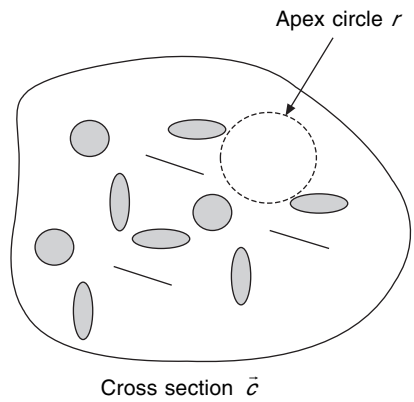

Fig. 5 Concept of 'aperture circle' of various radii on the cross section

In order to derive the distribution of the variable r, let us examine Fig. 6 where an aperture circle of radius r is placed on the cross section (Θ, Φ) of unit area along with a fiber cut end of radius $\rho(\Theta, \Phi)$.

According to Komori and Makishima [76], these two circles will contact each other when the center of the latter is brought into the inside of the circle of radius $r + \rho$, concentric with the former. The probability $f(r)dr$, that the aperture circle and the fiber do not touch each other, but that the former, of slightly larger radius $r + dr$, does touch the latter, is approximately equal to the probability when $\nu(\Theta, \Phi)$ points

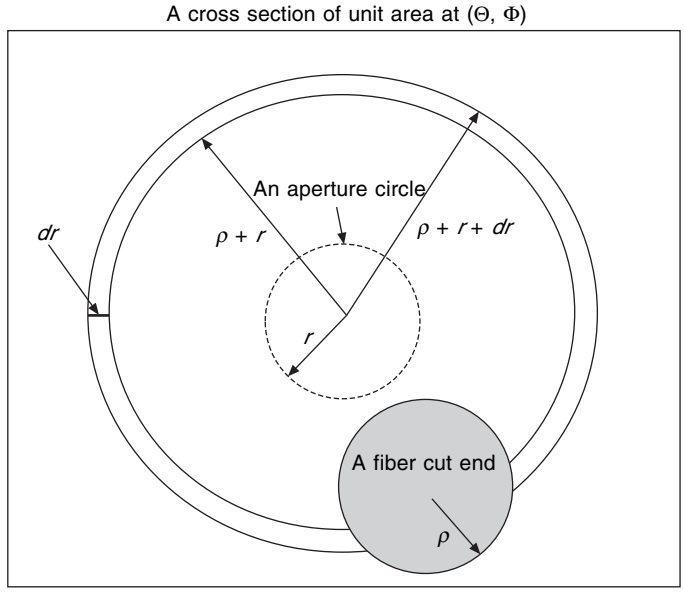

Fig. 6 Fiber cut end and pores

(the fiber cut ends) are scattered on the plane, no point enters the circle of radius $r + \rho$, and at least one point enters the annular region, two radii of which are $r + \rho$ and $r + \rho + dr$.

When x fiber cut ends are randomly distributed in a unit area, taking into account the area occupied by the fiber, the probability that at least one point enters the annular region $2\pi(r + \rho)dr$ is

$$\frac{2x\pi(r+\rho)\,dr}{1-[\pi(r+\rho)^2-\pi\rho^2]} \qquad (x = 0, 1, 2,\ldots) \tag{26}$$

and the probability of no point existing in the area $\pi(r + \rho)^2 - \pi\rho^2$ is

$$\{1-[\pi(r+\rho)^2-\pi\rho^2]\}^x \tag{27}$$

Then the joint probability, $f_x(r)dr$, that no point is contained in the circle of radius $r + \rho$ but at least one point is contained in the circle of radius $r + \rho + dr$, is given by the product of the two expressions as

$$f_x(r)dr = 2x\pi(r+\rho)dr\{1-[\pi(r+\rho)^2-\pi\rho^2]\}^{x-1} \tag{28}$$

Because the number of fiber cut ends is large and they are distributed randomly, their distribution can be approximated by the Poisson's function

$$\frac{v^x}{x!}e^{-v} \tag{29}$$

Therefore, the distribution function of the radii of the aperture circles $f(r)$ is given by

$$f(r)dr = \sum_{x=0}^{\infty} \frac{\nu^x}{x!} e^{-\nu} f_x(r)dr = 2\pi\nu(r+\rho)e^{-\nu}dr \sum_{x=1}^{\infty} \frac{[\nu + \pi\nu\rho^2 - \pi\nu(r+\rho)^2]^{x-1}}{(x-1)!}$$

$$= 2\pi\nu(r+\rho)e^{-\nu}e^{\nu+\pi\nu\rho^2-\pi\nu(r+\rho)^2}dr$$

$$= 2\pi\nu(r+\rho)e^{\pi\nu\rho^2}e^{-\pi\nu(r+\rho)^2}dr \tag{30}$$

It can be readily proved that

$$\int_0^{\infty} f(r)dr = \int_0^{\infty} 2\pi\nu(r+\rho)e^{\pi\nu\rho^2}e^{-\pi\nu(r+\rho)^2}dr = e^{\pi\nu\rho^2}e^{-\pi\nu\rho^2} = 1$$

So this function is valid as the *pdf* of distribution of the aperture circles made of the pores, and it provides the distribution of the pores at a given cross section. The result in Equation 30 is different from that of Komori and Makishima in [76], which ignored the area of fiber cut ends and hence does not satisfy the normalization condition.

The average value of the pore radius, $\bar{r}(\Theta, \Phi)$, can then be calculated as

$$\bar{r}(\Theta,\Phi) = \int_0^{\infty} rf(r)dr = \int_0^{\infty} 2r\pi\nu(r+\rho)e^{\pi\nu\rho^2}e^{-\pi\nu(r+\rho)^2}dr$$

$$= e^{\pi\nu\rho^2}\int_{\rho}^{\infty} 2\pi\nu t(t-\rho)e^{-\pi\nu t^2}dr \approx e^{\pi\nu\rho^2}\int_0^{\infty} 2\pi\nu t^2 e^{-\pi\nu t^2}dt$$

$$= \frac{e^{\pi\nu\rho^2}}{2\sqrt{\nu}} \tag{31}$$

where $t = (r + \rho)$ has been used to facilitate the integration. Similarly the variance $\Xi_r(\Theta, \Phi)$ of the pore radius can be calculated as

$$\Xi_r(\Theta,\Phi) = \int_0^{\infty} r^2 f(r)dr$$

$$= \int_0^{\infty} 2r^2\pi\nu(r+\rho)e^{\pi\nu\rho^2}e^{-\pi\nu(r+\rho)^2}\,dr = \frac{e^{\pi\nu\rho^2}}{\pi\nu} = \frac{2}{\pi\sqrt{\nu}}\bar{r}(\Theta,\Phi) \tag{32}$$

Note that for a given structure, the solution of the equation

$$\frac{d\Xi_r(\Theta,\Phi)}{d(\Theta,\Phi)} = 0 \tag{33}$$

gives us the cross sections in which the pores distribution variation reaches the extreme values, or the cross sections with the extreme distribution non-uniformity of the pores. As a result, these cross sections are most likely to be the directions of interest.

2.2.5.3 Tortuosity Distributions in Fibrous Materials

The variable *r* specifies only the areas of the spaces occupied by the pores. The actual volumes of the spaces are also determined by the depth of the spaces, known as the tortuosity.

Tortuosity is also defined as the ratio of the length of a true flow path for a fluid and the straight-line distance between inflow and outflow. This is, in effect, a kinematical quantity as the flow itself may alter the path.

In fibrous materials, the space occupied by pores is often interrupted because of the existence or interference of fibers, as seen in Fig. 7.

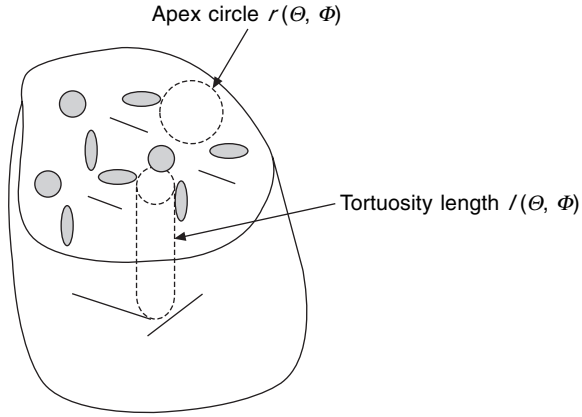

Fig. 7 Concept of 'tortuosity' of pores

If we examine a line of unit length in the direction (Θ, Φ), the average number of fiber intersections on this line is provided by Komori and Makishima [76] and Pan [71] as

$$n(\Theta, \Phi) = 2r_f N l_f J(\Theta, \Phi) = 2\frac{V_f}{\pi r_f} J(\Theta, \Phi) \tag{34}$$

where $J(\Theta, \Phi)$ is the mean value of $|\sin \chi|$,

$$J(\Theta, \Phi) = \int_0^{\pi} d\theta \int_0^{\pi} d\phi |\sin \chi| \Omega(\theta, \phi) \sin \theta$$

a parameter reflecting the fiber misorientation.

Following [76], we define the free distance as the distance along which the pores travel without interruption by the constituent fibers, or the distance occupied by the pores between two interruptions by the fibers, at a given direction. Here we assume that the interruptions occurred independently.

Suppose that $n(\Theta, \Phi)$ segments of the free distance are randomly scattered on this line of unit length. The average length of the free distance, l_m, is given as

$$l_m(\Theta, \Phi) = \frac{1 - V_f}{n(\Theta, \Phi)} \tag{35}$$

According to Kendall's analysis [77] of non-overlapping intervals on a line, the distribution of the free distance l is given as

$$f(l)dl = \frac{l}{l_m} e^{-\frac{l}{l_m}} dl \tag{36}$$

 doi:10.1533/tepr.2006.0002

It is easy as well to prove that

$$\int_0^\infty f(l)dl = \int_0^\infty \frac{l}{l_m} e^{-\frac{l}{l_m}} dl = 1 \tag{37}$$

This is also a better result than the one given by Komori and Makishima [76], for their result again does not satisfy the normalization condition. We already have l_m in Equation 35 as the mean of l, and the variance of l is thus given by

$$\Xi_l(\Theta, \Phi) = \int_0^\infty l^2 f(l)dl = \int_0^\infty l^2 \frac{l}{l_m} e^{-\frac{l}{l_m}} dl = 2l_m^2 \tag{38}$$

These statistical variables can be used to specify the local variations of the fiber and pore distribution or the local heterogeneity of a fibrous material. Also, because of the association of the local concentration of the constituents and some system properties, these variables can be utilized to identify the irregular or abnormal features caused by the local heterogeneity in the material.

Finally, when dealing with a fibrous material with local heterogeneity whose properties are location-dependent owing to the distributions of the fibers and the pores, we have to examine the specific places in the material where the local volumes occupied by the pores, as functions of the aperture circles and the free distance, are not constant but follow statistical distributions. Therefore, in this case, using the system or overall volume fraction V_f alone will not be adequate, and the concept of local fiber volume fraction is more relevant.

2.3 Results for Special Cases

Since we have all the results of the parameters defining the distributions of the constituents in a fibrous material, it becomes possible to predict the irregularities of the system characteristics once a fiber orientation *pdf* is given.

2.3.1 Determination of Fiber Orientation, pdf

It has to be admitted that, although the statistical treatment using the fiber orientation *pdf* is a powerful tool, the major difficulty comes from the determination of the probability density function for a specific case. Cox [17] proposed for a fiber network that such a density function can be assumed to be in the form of Fourier series. The constants in the series are dependent on the specific structures. For simple and symmetrical orientations, the coefficients are either eliminated or determined without much difficulty. However, it becomes problematic for more complex cases where asymmetrical terms exist. Because of the central limit theorem, the present author has proposed in [78] to apply the Gaussian function or its equivalence in the periodic case, the von Mises Function [79], to approximate the distribution in question, provided that the coefficients in the functions can be determined through, most probably, experimental approaches. Sayers [80] suggested that the coefficients of the fiber orientation function of any form be determined by expanding the orientation function into the generalized Legendre functions. Recently MRI technique [81] and Fourier transformation [82] have also been proposed that can be used to establish the fiber orientation *pdf*. To demonstrate the application of the theoretical results obtained in this study however, we will employ one simple and hypothetic case below.

2.3.2 A Random Distribution Case

Let us first consider an ideal case where all fibers in a material are oriented in a totally random manner with no preferential direction; the randomness of fiber orientation implies that the density function is independent of both coordinates θ and ϕ. Therefore this density function would have the form of

$$\Omega(\theta, \phi) = \Omega_0 \tag{39}$$

where Ω_0 is a constant whose value is determined from the normalization condition as

$$\Omega_0 = \frac{1}{2\pi} \tag{40}$$

Using this fiber orientation *pdf*, we can calculate the system parameters by replacing (Θ, Φ) with (0, 0) for the isotropy so that

- $\cos \chi = \cos(\Theta, \theta, \Phi, \phi) = \cos \theta$;
- $\sin \chi = \sin \theta$;
- $\Upsilon(\Theta, \Phi) = \frac{1}{2}$;
- $J(\Theta, \Phi) = \frac{\pi}{4}$;
- $A(\Theta, \Phi) = \frac{1}{2\pi} V_f$;
- $v(\Theta, \Phi) = \frac{V_f}{4\pi\pi r_f^2}$;
- $\rho(\Theta, \Phi) = \sqrt{2} r_f$;
- $n(\Theta, \Phi) = \frac{V_f}{2r_f}$;
- $\bar{r}(\Theta, \Phi) = \frac{\pi r_f}{\sqrt{V_f}} e^{\frac{V_f}{2\pi^2}}$;
- $\Xi_r(\Theta, \Phi) = \frac{4\pi r_f^2}{V_f} e^{\frac{V_f}{2\pi^2}}$;
- $l_m(\Theta, \Phi) = 2r_f \left(\frac{1}{V_f} - 1 \right)$;
- $\Xi_l(\Theta, \Phi) = 8r_f^2 \left(\frac{1}{V_f} - 1 \right)^2$;

The following discussion provides detailed information on the distributions of both the fibers and pores in this isotropic system. As seen from the above calculated results, for this given fiber orientation *pdf*, all of the distribution parameters are

dependent on the system fiber volume fraction V_f and fiber radius r_f, regardless of the fiber length l_f. Therefore, we will examine the relationships between the distribution parameters and these two factors.

Figure 8 depicts the effects of these two factors on the number of fiber cut ends v per unit area on an arbitrary cross section, using the calculated results. It is seen from the figure that, as expected, for a given system fiber volume fraction V_f, the thinner the fiber, the more cut fiber ends per unit area, whereas for a given fiber radius r_f, increasing the system fiber volume fraction will lead to more cut fiber ends.

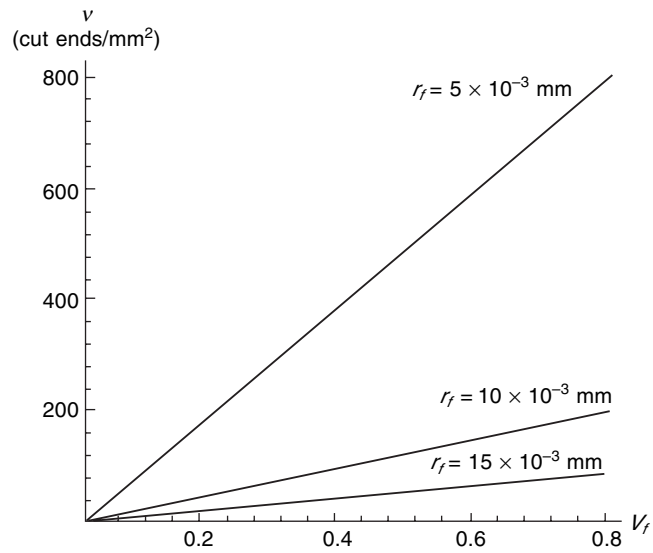

Fig. 8 Mean cut fiber ends v versus the volume fraction V_f at different fiber radius levels

The distribution density function $f(r)$ of the radius r of the aperture circles is constructed, based on Equation 30, and the illustrated results are produced accordingly. Figure 9(a) shows the distribution of $f(r)$ at three fiber radius r_f levels when the overall fiber volume fraction $V_f = 0.6$, whereas Fig. 9(b) is the result at three V_f levels when the fiber radius is fixed at $r_f = 5.0 \times 10^{-3}$ mm.

It is seen in Fig. 9(a) that when the fiber becomes thicker, there are more aperture circles with smaller radius values and fewer ones with larger radius values. Decreasing the overall fiber volume fraction V_f has a similar effect as seen in Fig. 9(b).

The effects of both V_f and fiber radius r_f on the variance Ξ of the aperture circle radius distribution is calculated using Equation 32, as shown in Fig. 9(c). Again, a finer fiber or a greater V_f will lower the variation of the aperture circle radius r.

Finally, Fig. 9(d) is plotted based on Equation 31, showing the average radius $\bar{r}$ of the aperture circles as a function of the system fiber volume fraction at three fiber size levels. The average radius of the aperture circles will decrease when either the fiber radius reduces (meaning more fibers for a given fiber volume fraction V_f), or the system fiber volume fraction increases.

Figure 10(d) shows the effects of the two factors on the average free distance l_m of the pores using Equation 35. It follows the same trend as $\bar{r}$ in Fig. 9(d), i.e. for a

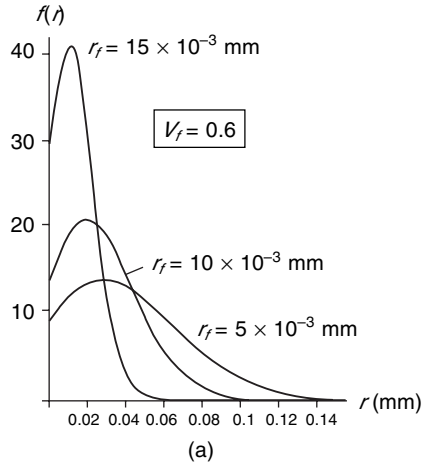

Fig. 9(a) Distribution of r at three r_f levels

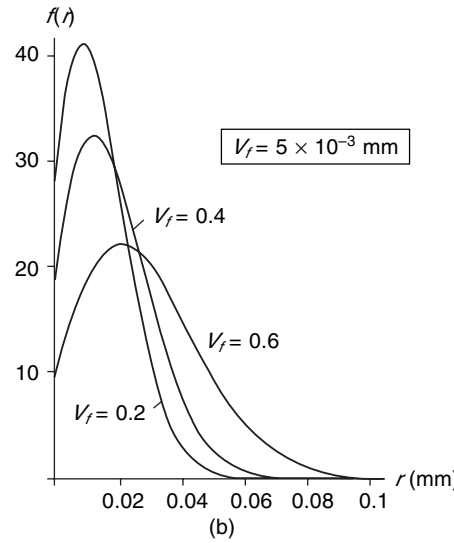

Fig. 9(b) Distribution of r at three V_f levels

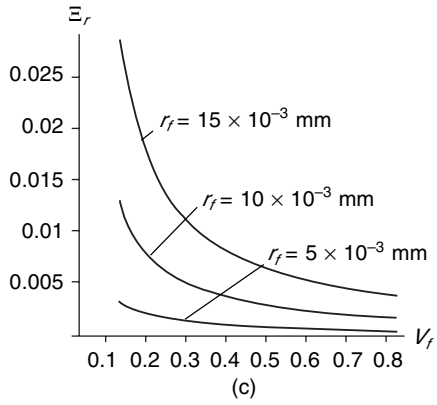

Fig. 9(c) Variance of r vs. V_f at three r_f levels

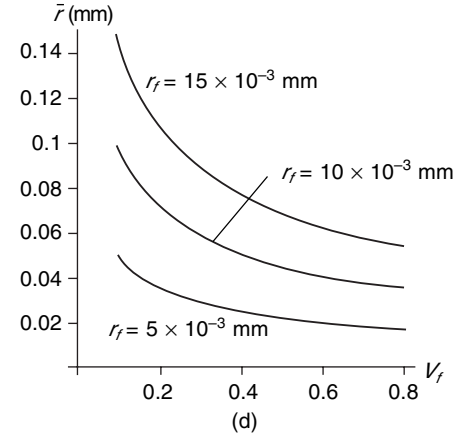

Fig. 9(d) Mean value of $\bar{r}$ against V_f at three r_f levels

given fiber volume fraction V_f, thinner fibers (more fibers contained) will lead to a shorter l_m value. The reduction of l_m value can also be achieved when we increase the system fiber volume fraction, while keeping the same fiber radius.

The distribution function $f(l)$ of the free distance l is from Equation 36, and the results are illustrated in Figures 10(a) and (b). When increasing either the fiber size r_f or the system fiber volume fraction V_f, the portion of free distance with shorter length will increase and that with longer length will decrease.

The variance Ξ_l of the free distance distribution is provided in Fig. 10(c), and the effects of r_f and V_f on Ξ_l are similar but more significant compared to the case of r in Fig. 9(c). Furthermore, it is interesting to see that although the fibrous material dealt with here is an isotropic one in which all the fibers are oriented in a totally

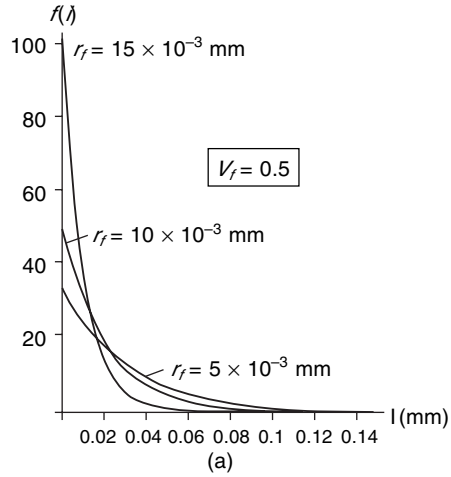

Fig. 10(a) Distribution of l at three r_f levels

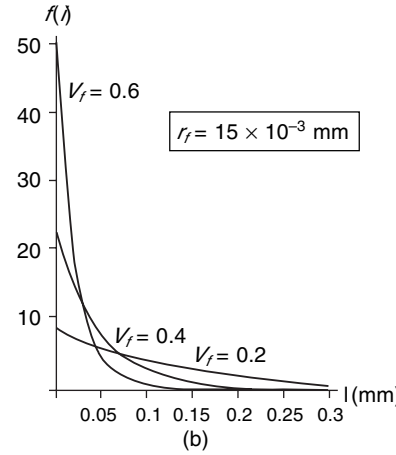

Fig. 10(b) Distribution of l at three V_f levels

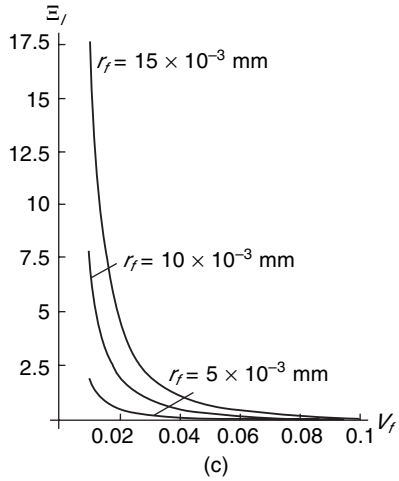

Fig. 10(c) Variance of l against V_f at three r_f levels

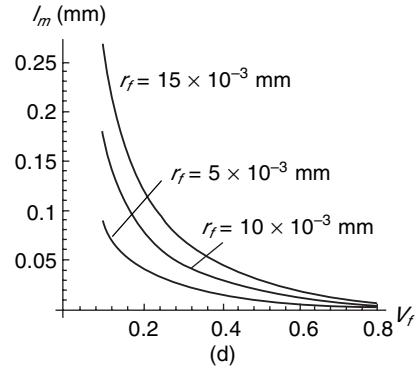

Fig. 10(d) Mean l_m vs. the fiber volume fraction V_f at three r_f levels

random manner with no preferential direction, there still exist variations or irregularities in both r and l, leading to a variable local fiber volume fraction from location to location. In other words, the material is still a heterogeneous one.

3. WETTING AND WICKING

3.1 Introduction

Wetting and wicking are among the most frequently observed phenomena in the processing and use of fibrous materials, when water or any other liquid chemical comes into contact with and is transported through fibrous structures. Besides their involvement in such processes as scouring, dyeing and finishing, wetting and wicking properties of fibrous materials are also paramount factors in evaluating the comfort and performance of clothing fabrics, hygiene products, etc. Accordingly, extensive

research has been carried out in this field to study the theories, characterization and testing methods, and modeling and simulation techniques of the wetting and wicking phenomena.

3.2 Surface Tension and Interfacial Interaction: Wetting and Wicking Theories

3.2.1 Wetting

The term 'wetting' is usually used to describe the displacement of a solid–air interface with a solid–liquid interface. When a small liquid droplet is put in contact with a flat solid surface, two distinct equilibrium regimes may be found: partial wetting with a finite contact angle θ, or complete wetting with a zero contact angle [83], as shown in Fig. 11.

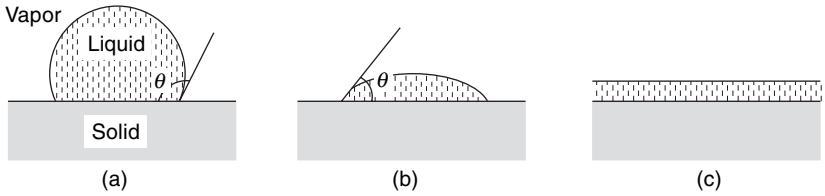

Fig. 11 A small liquid droplet in equilibrium over a horizontal surface: (a) partial wetting, mostly non wetting, (b) partial wetting, mostly wetting, (c) complete wetting

The forces in equilibrium at a solid–liquid boundary are commonly described by the Young's equation:

$$\gamma_{SV} - \gamma_{SL} - \gamma_{LV} \cos\,\theta = 0 \tag{41}$$

where γ_{SV}, γ_{SL}, and γ_{LV} denotes interfacial tensions between solid/vapor, solid/liquid and liquid/vapor, respectively, and θ is the equilibrium contact angle.

The parameter that distinguishes partial wetting and complete wetting is the so called spreading parameter S, which measures the difference between the surface energy (per unit area) of the substrate when dry and wet:

$$S = [E_{\text{substrate}}]_{\text{dry}} - [E_{\text{substrate}}]_{\text{wet}} \tag{42}$$

or

$$S = \gamma_{SO} - (\gamma_{SO} + \gamma) \tag{43}$$

where γ_{SO} is surface tension of a vapor free or 'dry' solid surface, γ is surface tension of the liquid. Usually, we know $\gamma \equiv \gamma_{LV}$ by separate measurements [83].

If the parameter S is positive, the liquid spreads completely in order to lower its surface energy ($\theta = 0$). The final outcome is a film of nano-scopic thickness resulting from competition between molecular and capillary forces.

If the parameter S is negative, the drop does not spread out, but forms at equilibrium a spherical cap resting on the substrate with a contact angle θ. A liquid is said to be 'mostly wetting' when $\theta \leq \pi/2$, and 'mostly non-wetting' when $\theta > \pi/2$ [84]. When contacted with water, a surface is usually called 'hydrophilic' when $\theta \leq \pi/2$, and 'hydrophobic' when $\theta > \pi/2$.

3.2.2 Wicking

Wicking is the spontaneous flow of a liquid in a porous substrate, driven by capillary

forces. As capillary forces are caused by wetting, wicking is a result of spontaneous wetting in a capillary system [85].

In the simplest case of wicking in a single capillary tube, as shown in Fig. 12, a meniscus is formed. The surface tension of the liquid causes a pressure difference across the curved liquid/vapor interface. The value for the pressure difference of a spherical surface was deduced in 1805 independently by Thomas Young (1773–1829) and Pierre Simon de Laplace (1749–1827), and is represented with the so called Young–Laplace equation [86]:

$$\Delta P = \gamma_{LV}\left(\frac{1}{R_1} + \frac{1}{R_2}\right) \tag{44}$$

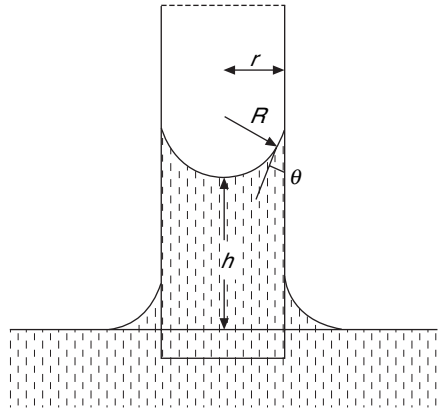

Fig. 12 Wicking in a capillary

For a capillary with a circular cross section, the radii of the curved interface R_1 and R_2 are equal. Thus:

$$\Delta P = 2\gamma_{LV}/R \tag{45}$$

where

$$R = r/\cos\,\theta \tag{46}$$

and r is the capillary radius. As the capillary spaces in a fibrous assembly are not uniform the effective capillary radius r_e is used instead. This is usually determined indirectly.

3.2.3 Surface Tension and Interfacial Interactions

The above discussions show that both wicking and wetting behaviors are determined by surface tensions (of solid and liquid) and liquid/solid interfacial tensions. These surface/interfacial tensions, in macroscopic concepts, can be defined as the energy that must be supplied to increase the surface/interface area by one unit. In microscopic concepts, however, they are originated from such intra-molecular bonds as covalent, ionic or metallic, and such long range intermolecular forces as van der Waals forces. Therefore, the physical bases of wetting and wicking are these molecular interactions within a solid or liquid, or across the interface between liquid and solid.

3.2.3.1 Macroscopic: Wettability

From studies on the bulk cohesive energy, we learn that there are two main types of solids: hard solids (bound by covalent, ionic or metallic bonds) with so called 'high energy surfaces', and weak molecular crystals (bound by van der Waals forces, or in some special cases by hydrogen bonds) with 'low energy surfaces'. The surface tension, γ_{SO}, is in the range of 500 to 5000 mN/m for high energy surfaces, and 10 to 50 mN/m for low energy surfaces [87]. Most organic fibers belong to the 'low energy surfaces' category.

Most low MW liquids (simple liquids with low molecular weight) achieve complete wetting with high-energy surfaces [83]. In the idealized case where liquid/liquid and liquid/solid interactions are purely of the van der Waals type (no chemical bonding), solid/liquid energy can be deduced as follows:

If a semi-infinite solid and a semi-infinite liquid are brought together, they start with an energy $\gamma + \gamma_{SO}$, and end in γ_{SL}, as the van der Waals interaction energy between solid and liquid V_{SL} is consumed. This process can be expressed as:

$$\gamma_{SL} = \gamma_{SO} + \gamma - V_{SL} \tag{47}$$

To a first approximation, the van der Waals couplings between two species are simply proportional to the product of the corresponding polarizabilities α [83]:

$$V_{SL} = k\alpha_S\alpha_L \tag{48}$$

Similarly, if two liquid portions are brought together, they start with energy $2\gamma_{LV}$, and end up with zero interfacial energy:

$$2\gamma - V_{LL} = 0 \tag{49}$$

The same applies to solids:

$$2\gamma_{SO} - V_{SS} = 0 \tag{50}$$

Equation (43) combined with (47)–(50) gives:

$$S = \gamma_{SO} - (\gamma_{SL} + \gamma) = V_{SL} - V_{LL} = k(\alpha_S - \alpha_L)\alpha_L \tag{51}$$

Therefore, a liquid spreads completely if $\alpha_S > \alpha_L$ so as to make S positive.

Low-energy surfaces can give rise to partial or complete wetting, depending on the liquid chosen [83]. The empirical criterion of Zisman [84, 88] is that each solid substrate has a critical surface tension γ_C, and there is partial wetting when the liquid surface tension $\gamma > \gamma_C$ and total wetting when $\gamma < \gamma_C$.

The critical surface tension can be determined by the so called Zisman plot. A series of homologous liquids (usually *n*-alkanes, with *n* the variable) is chosen for the study. Cos θ as a function of γ is plotted to give the critical surface tension, as shown in Fig. 13. Critical surface tension of some solid polymers is shown in Table 1 [83, 84].

3.2.3.2 Microscopic: Van der Waals Forces

Molecules can attract each other at moderate distances and repel each other at close range, as denoted by the Lennard–Jones potential:

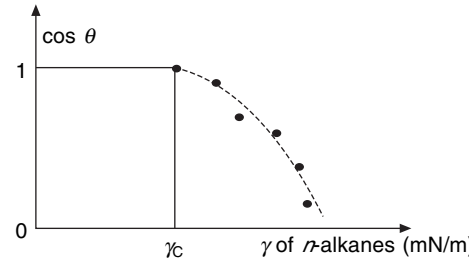

Fig. 13 Typical Zisman plot to determine critical surface tension γ_C

Table 1 Critical surface tension γ_C of several solid polymers

Solid	Nylon	PVC	PE	PVF	PTFE
γ_C (mN/m)	46	39	31	28	18

$$w(r) = \frac{A}{r^{12}} - \frac{C}{r^6} \tag{52}$$

where $w(r)$ is the interactive potential between two molecules at distance r, and A and C are the intensities of the repellency and attraction, respectively.

The attractive forces, represented by the second term at the right hand side of Equation (52), are collectively called 'van der Waals forces'. This is one of the most important long-range forces between macroscopic particles and surfaces. Van der Waals forces are much weaker than chemical bonds, and random thermal agitation, even around room temperature, can usually overcome or disrupt them. However, they play a central role in all phenomena involving intermolecular forces, including those actions between electrically neutral molecules [89].

When those intermolecular forces are between like molecules, they are referred to as cohesive forces. For example, the molecules of a water droplet are held together by cohesive forces. The cohesive forces between molecules inside a liquid are shared with all neighboring atoms. Those on the surface have no neighboring atoms beyond the surface, and exhibit stronger attractive forces upon their nearest neighbors on the surface. This enhancement of the intermolecular attractive forces at the surface is called surface tension, as shown in Fig. 14.

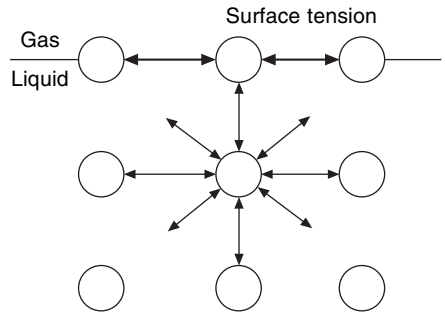

Fig. 14 Liquid surface tension caused by cohesive forces between liquid molecules

Intermolecular forces between different molecules are known as adhesive forces. They are responsible for wetting and capillary phenomena. For example, if the adhesive forces between a liquid and a glass tube inner surface are larger than the cohesive forces within the liquid, the liquid will rise upwards along the glass tube to show capillary phenomenon, as shown in Fig. 12.

To derive the van der Waals interaction energy between two bodies/surfaces from the pair potential $w(r) = -C/r^6$, Hamaker [90] introduced an additivity assumption that the total interaction can be seen as the sum over all pair interactions between any atom in one body and any atom in the other, thus obtaining the 'two body' interaction energy, such as that for two spheres (Fig. 15a), for a sphere near a surface (Fig. 15b), and for two flat surfaces (Fig. 15c) [89]. And the Hamaker Constant A is given as a function of the densities of the two bodies:

$$A = \pi^2 C \rho_1 \rho_2 \tag{53}$$

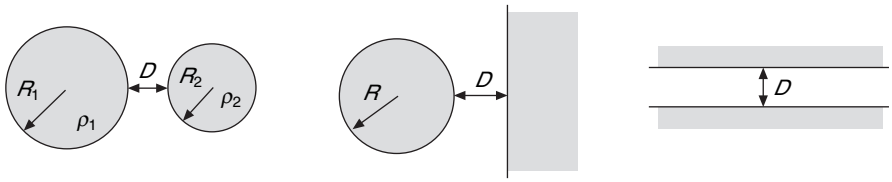

(a) Two spheres

$$W = -\frac{A}{6D}\frac{R_1 R_2}{R_1 + R_2}$$

(a)

(b) Sphere–surface

$$W = -\frac{AR}{6D}$$

(b)

(c) Two surfaces

$$W = -\frac{A}{12\pi D^2}$$

(c)

Fig. 15 Van der Waals interaction free energies between selected bodies

Hamaker's theory has been used widely in studies of surface/interface interactions and wetting phenomena, although there have been concerns about its additivity assumption and its ignoring of the influence of neighboring atoms on the interaction between any atom pair [89, 91].

The problem of additivity is completely avoided in Lifshitz's theory [89, 91–93]. The atomic structure is ignored, and interactive bodies are regarded as dielectric continuous media. Then, the forces between large bodies can be derived in terms of such bulk properties as their dielectric constants and refractive indices. And the net result of a rather complicated calculation is that Lifshitz regained the Hamaker expressions in Fig. 15, but with a different interpretation of the Hamaker constant A. An approximate expression for the Hamaker constant of two bodies (1 and 2) interacting across a medium 3, none of them being a conductor, is [89, 91]

$$A_{1,2} = \frac{3hv_e(n_1^2 - n_3^2)(n_2^2 - n_3^2)}{8\sqrt{2}(n_1^2 + n_3^2)^{1/2}(n_2^2 + n_3^2)^{1/2}[(n_1^2 + n_3^2)^{1/2} + (n_1^2 + n_3^2)^{1/2}]} + \frac{3}{4}kT\frac{\varepsilon_1 - \varepsilon_3}{\varepsilon_1 + \varepsilon_3}\frac{\varepsilon_2 - \varepsilon_3}{\varepsilon_2 + \varepsilon_3} \tag{54}$$

where h is the Planck's constant, v_e is the main electronic adsorption frequency in the

UV (assumed to be the same for the three bodies, and typically around 3×10^{15} s^{-1}), n_i is the refractive index of phase i, ε_i is the static dielectric constant of phase i, k is the Boltzmann constant, and T the absolute temperature.

3.3 Liquid Penetration Through Fibrous Materials

There has been much research work published on the wetting process on solid surfaces, including several comprehensive reviews [83, 94] that cover topics from contact angle, contact line, liquid/solid adhesion, to wetting transition (from partial wetting to complete wetting) and dynamics of spreading. However, wetting of fibrous materials becomes an even more complex process due to at least two factors:

(i) There is the interaction of liquid with a porous medium with an *intricate, tortuous* and yet *soft* surface, instead of a simple solid one.
(ii) There are often imbibitions of liquid into the *interior* of the fibers, which may cause changes in the structure and properties of the fibrous materials.

3.3.1 Wicking Dynamics

Most textile processes are time limited, so the kinetics of wicking becomes very important. The classical Washburn–Lucas equation [95] describes the liquid's velocity, *dh/dt*, moving up or down in a perpendicular capillary with radius r, neglecting the inertia of the liquid column.

$$\frac{dh}{dt} = \frac{r\gamma\cos\theta}{4\eta h} \tag{55}$$

where η is the viscosity of liquid, γ the surface tension and ρ the density of liquid.

To apply the Washburn equation into wicking studies, Minor [96, 97] used several kinds of liquid in his wicking experiments and established that the wicking height of a liquid in a fiber or yarn is proportional to the square root of the time

$$h = W_c t^{\frac{1}{2}} = \left(\frac{r\gamma\cos\theta}{2\eta} t\right)^{\frac{1}{2}} \tag{56}$$

According to Equation (56), the height of the liquid front will keep rising with time. Actually, however, the liquid column will cease to rise after a certain period of time due to the balance of surface tension and gravity. And the parameter r is hard to determine as the yarn is not geometrically equivalent to a capillary tube. Furthermore, the equation incorrectly assumes a constant advancing contact angle for the moving liquid front. Despite these limitations, a variety of liquids are reported to obey the Washburn kinetics [98].

Also, much effort has been dedicated to the modification of the Washburn equation. In some early work, constants or coefficients were adopted to account for the difference between wicking theories and experiments, such as a hydraulic constant [99], which represents the porous structure of fibrous materials.

Other work tries to accommodate the effect of gravity [100–103]. The Washburn equation that includes the effect of gravity contains two constants:

$$At = -Bt \ln(1 - Bt) \tag{57}$$

where $$A = \frac{\rho^2 g^2 r^3}{16\eta\gamma\cos\theta}, \quad B = \frac{\rho g r}{2\gamma\cos\theta} \tag{58}$$

where g is the gravitational constant.

Equation (57) is not analytically solvable, and usually requires approximation or experimental fit. Recently, some researchers have been trying to incorporate the gravity effect into the wicking process by means of statistical mechanics (i.e. modeling and simulation) [104–108]. Details of these modeling and simulation techniques are discussed in Section 3.5.

In addition, dynamic contact angle has been discussed in studies of wicking dynamics. It can be found either with an empirical equation [101, 109] or experimental analysis [110–112]. Quere and Di Meglio [109] showed that, in a capillary rise of silicone oil along a vertical thin fiber, most of the rising time is spent in a long regime of relaxation towards equilibrium, where θ varies to $t^{-1/2}$. Clanet and Quere [112] experimentally studied the dynamical phenomenon of capillary rise in a vertical fiber with liquids of low and high viscosity, and also found the dynamic angle θ scales to $t^{-1/2}$. More recently, various modeling methods, such as molecular kinetics, molecular hydrodynamics [113], and molecular dynamics [114–116] have been used to study the dynamic evolution of the contact angle during the wicking process. And Seveno [114] predicts that there are two different time scale behaviors within the wicking process related to the two dissipation channels: friction between the liquid and the solid, leading to t^{-1}, and hydrodynamics, leading to $t^{-1/2}$.

Wicking is also affected by the morphology of fibrous assemblies. Fibrous structures are never of a perfect capillary, and are changeable due to swelling of fibers (if hydrophilic) [117, 118], and this can therefore further complicate the problem [119]. Although there have been reported studies on deriving equivalent capillary radii and equivalent contact angles for wicking problems in fibrous materials [120], as well as wicking flow on periodically irregular capillaries [121], an efficient and precise way of representing the intricate structure of fibrous structures is still awaited.

3.3.2 Wetting Dynamics

The wetting of fibrous materials is dramatically different from the wetting process on a flat surface due to the geometry of the cylindrical shape. A liquid that fully wets a material in the form of a smooth planar surface may not wet the same material when presented as a smooth fiber surface.

Brochard [122] discussed the spreading of liquids on thin cylinders and stated that, for nonvolatile liquids, a liquid drop cannot spread out over the cylinder if the spreading coefficient S is smaller than a critical value S_c, instead of 0. At the critical value S_c, there is a first order transition from a droplet to a sheath structure ('manchon'). The critical value was derived as

$$S_c = \frac{3}{2}\gamma\left(\frac{a}{b}\right)^{2/3} \tag{59}$$

where a is the molecular size, b is the radius of the cylinder.

There is also plenty of research work on the equilibrium shapes of liquid drops on fibers [123–132]. It was reported that two distinctly different geometric shapes of droplet are possible: a barrel and a clam shell, as shown in Fig. 16.

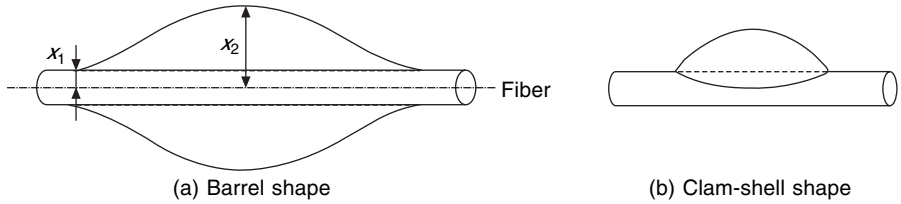

Fig. 16 Equilibrium liquid droplet shapes on a fiber

In the absence of gravity, the equilibrium shape of a drop surface is such that the Laplace excess pressure, as shown in Equation (44), across the drop surface is everywhere constant. Carroll [129] solved this equation for the axially symmetric barrel shape subject to the boundary condition that the profile of the fluid surface meets the solid at an angle given by the equilibrium contact angle θ:

$$\Delta P = \frac{2\gamma_{LV}(n - \cos\theta)}{x_1(n^2 - 1)} \tag{60}$$

where $n = x_2/x_1$, is the reduced radius as shown in Fig. 16 (a).

Carroll's solution for the barrel shape droplet was subsequently used to compute the surface free energy, defined as [124]:

$$F = \gamma_{LV}A_{LV} + (\gamma_{SL} - \gamma_{SV})A_{SL} \tag{61}$$

where A_{LV} and A_{SL} are the liquid/vapor and solid/liquid interfacial areas, respectively.

In contrast to the barrel shape droplet problem, no solution to Laplace's equation for the asymmetric clam-shell shape is reported except for such numerical approaches as finite element methods [132]. There are, however, papers discussing the roll-up (barrel to clam-shell) transition [132, 133] in the wetting process on a fiber.

In addition, there is work with respect to the gravitational distortion of barrel-shape droplets on vertical fibers [134]. To represent the heterogeneous nature of fibrous materials in the wetting process, Mullins *et al*. [135] incorporated a microscopic study of the effect of fiber orientation on the fiber wetting process when subjected to gravity, trying to account for the asymmetry of wetting behavior due to fiber orientation and gravity. The theory concerning the droplet motion and flow on fibers is based on the balance between drag force, gravitational force and the change in surface tension induced by the change in droplet profile as the fiber is angled. As a result, there comes out an angle where droplet flow will be maximized.

In reality, fibrous materials are porous media with *intricate*, *tortuous* and yet *soft* surfaces, further complicating the situation. As a result, a precise description of the structure of a fibrous material can be tedious. Therefore, much research work has adopted Darcy's law, an empirical formula that describes laminar and steady flow through a porous medium in terms of the pressure gradient and the intrinsic permeability of the medium [136–138]:

$$u = -\frac{K}{\mu}\nabla p \tag{62}$$

where u is the average velocity of liquid permeation into fibrous materials, μ the

newtonian viscosity of the liquid, K the permeability, and ∇_p the pressure gradient. In the case of wetting, the driving pressure is usually the capillary pressure as calculated by the Laplace equation. The permeability K is either determined by experiment or the empirical Kozeny–Carman relations as a function of the fiber volume fraction [138].

This approach, as adopted dominantly in solving problems of resin flow through fibrous preforms during composite fabrication, will be discussed in greater details in the next chapter. Darcy's law reflects the relationship of pressure gradient and average velocity only on a macroscopic scale, and it cannot reach the microscopic details of the liquid penetration in fibrous media. Accordingly, many researchers have tried to solve these problems by various modeling and simulation techniques, which will be discussed in details in Section 3.5.

3.4 Characterization Techniques for Wetting and Wicking Behavior of Fibrous Materials

Incorporated with various theories for wicking and wetting behaviors of fibrous materials, a series of characterization techniques have been developed to measure such important parameters as interfacial tension/energy, contact angle, liquid transport rate (either in volume or weight) or the liquid profile of fibrous materials. These techniques provide information for better understanding of wicking/wetting behaviors of fibrous materials, as well as for validation of the wicking/wetting theories.

3.4.1 Measuring Liquid/Fiber Contact Angle

The most common method of measuring the contact angle is to observe a sessile drop with a telescope or microscope, as shown in Fig. 17. The contact angle is either determined directly with a goniometer, or the image is recorded by a video system and the contour is fitted by a computer using the Laplace equation. For small drops where hydrostatic effects are negligible, the contact angle can be calculated from the height of the drop h and contact radius a [139]:

$$\tan\left(\frac{\theta}{2}\right) = \frac{h}{a} \tag{63}$$

Alternatively, the contact angle can be measured at the edge of a bubble, as shown in Fig. 17 (b). A bubble is positioned usually at the top of a cell which is otherwise filled with liquid. This method is less sensitive to interface pollution [140].

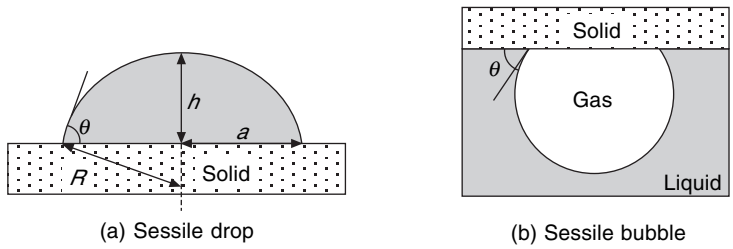

Fig. 17 Sessile drop and sessile bubble on a planar surface for measuring contact angle

The above methods can be used to measure the contact angle of a liquid on a planar fabric, but is difficult to deal with contact angle of a liquid on a filament due to the steep change in drop profile near the drop edge.

Bascom [141] avoided this problem by suspending a relatively large drop of liquid in a slit platinum loop, as shown in Fig. 18. The fiber is secured on a micro-positioner so that the fiber can be precisely moved through a slit in the loop into the center of the drop, where the surface is relatively flat, thus avoiding the curvature problem of a single droplet. The fiber can be moved in the vertical direction so that both receding and advancing angles can be observed. This technique can easily resolve contact angles of 40° or higher, but optical interference problems near the drop edge are encountered for lower angles.

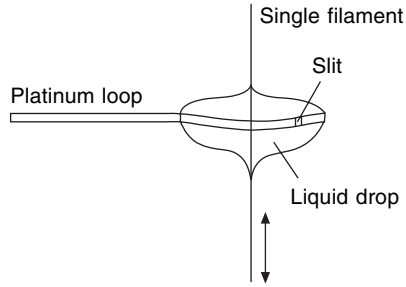

Fig. 18 Single filament contact angle measurement

More recently, measurement of contact angles on a single fiber are carried out by extracting droplet-on-fiber profiles, using various digital image processing techniques [142–145], or using such advanced techniques as ESEM (environmental scanning electron microscopy) [146, 147] to improve the reliability and accuracy of the results obtained. The geometry of the extracted droplet-on-fiber profile provides diverse characteristic drop parameters for the calculation of contact angles, including maximum drop length and height, drop volume, contact area, and inflection angle. Various methods are available based on different combination of these parameters [125, 148].

3.4.2 Measuring Liquid/Fiber Interfacial Tension/Energy

The most sensitive and widely used methods of measuring the wettability of single filaments is to measure the interfacial adhesion tension by using a recording electro-microbalance, the 'Wilhelmy method' [141, 149–151], as shown in Fig. 19. The fiber is suspended from one arm of an electro-balance and is partially submerged in a beaker of the test liquid. The platform holding the test liquid is mechanically moved in the vertical direction so that the advancing and receding angles can be measured.

The total force on the fiber is

$$F_T = 2\pi r\gamma_{LV} \cos\,\theta - \rho_L g\pi \mathrm{r}^2 h \tag{64}$$

where r is the fiber radius, h the depth of the fiber immersion and g the gravitational constant.

The first term on the right-hand side of Equation (64) represents the adhesion tension of the liquid on the fiber. The second term is the buoyant weight of the

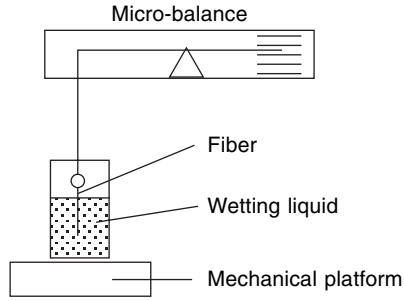

Fig. 19 Wilhelmy method for measuring interfacial tension between liquid/fiber

submerged fiber segment. The weight of the rest of the fiber (not submerged) and its support system, is tared off before the wetting test starts.

Also, the buoyancy term is negligible for thin fibers ($r < 50\mu$m). Consequently, for thin fibers the measured force is independent of fiber depth:

$$F_T = 2\pi r\gamma_{LV} \cos\,\theta \tag{65}$$

The contact angle can then be calculated as

$$\cos\,\theta = \frac{mg}{\pi d\gamma_{LV}} \tag{66}$$

where m is the balance output. This is also an indirect way of determining the contact angle. However, results obtained with this method often lack reproducibility [152].

3.4.3 Measuring Liquid Transport Rate or Profile in Fibrous Materials

Harnett *et al*. have published a comprehensive review on the laboratory test methods for measuring wicking. They include strip test, plate test, spot test, and siphon test [153]. Among these, the most frequently used is the strip test [154–157]. A strip of test fabric (or a single filament/yarn) is suspended vertically with its lower end immersed in a reservoir of liquid, to which a dye may be added for tracking the movement of the liquid. The height reached by the liquid in the fabric (filament/yarn) above the liquid surface level in the reservoir is measured either after a certain period of time, or recorded continuously by some image analysis/data collecting apparatus.

In addition to the above direct visualization test methods, indirect measuring methods such as electrical capacity/resistance techniques [158, 159], have also been used to assess the wicking behavior of fibrous materials. With these, rise of liquid water in the yarn triggers an electrical circuit that can be coupled with a personal computer so that the distance of water rise as a function of time can be determined.

3.5 Computer Experiments: Simulation Techniques for Liquid Transport in Fibrous Materials

Preceding sections have already dealt with theories and experimental testing techniques for liquid transport in fibrous materials. In a typical experiment, the system is subjected to measurements, and results, expressed in numeric form, are obtained. Now in theory, a model of the system can be constructed, usually in the form of a set of

mathematical equations, which can then be validated by its ability to describe the system behavior in certain selected cases; however, this generally implies a considerable amount of simplification in order to eliminate some of the complexities associated with real world problems, and to make the problem mathematically tractable.

To be specific, the simplifications involved in many liquid transport models include substituting the intricate and tortuous fibrous structure with an average parameter such as porosity, solidity or permeability. This will give rise to error during calculation and prediction of transport behavior of liquid in fibrous materials, especially micro/nano scale materials. Accordingly, various computer simulation techniques have been applied in this field to accommodate more complexity so as to investigate more realistic systems, and to better understand and explain experiment results. These techniques are also known as computer experiments.

Molecular Dynamics (MD) and Monte Carlo (MC) are best-known, standard simulation formulas emerging from the last decades [160] and, accordingly, most of the simulation for clarifying liquid wetting and transport behavior falls into these two categories.

Fundamentally, wetting and transport behaviors of liquid in fibrous materials stem from interactions between liquid/solid and within the liquid, at the microscopic level. The most important task for the various models and simulations is, therefore, to define and treat these interactions.

In Molecular Dynamics, all potentials between atoms, solid as well as liquid, are described with the standard pairwise Lennard–Jones interactions:

$$V_{ij}(r) = 4\varepsilon_{ij}\left(\left(\frac{\sigma_{ij}}{r}\right)^{12} - \left(\frac{\sigma_{ij}}{r}\right)^{6}\right) \tag{67}$$

where r is the distance between any pair of atoms i and j, ε_{ij} is an energy scale (actually the minimum of the potential), and σ_{ij} is a length scale (the distance at which the potential diminishes to zero).

Large scale MD simulations have been adopted to study the spreading of liquid drops on top of flat solid substrates [115, 116, 161]. If the system contains enough liquid molecules, the macroscopic parameters, such as the density, surface tension, viscosity, flow patterns and dynamic contact angle, can be 'measured' in the simulation. However, the computational cost for MD simulations is huge, as they are dealing with the individual behavior of a great number of single molecules. Also, the application of MD simulations for liquid spreading on a fiber or transport in intricate fibrous structures is still not fully developed.

To solve the problem of huge computation, simulation techniques have been invented to cope with the so called 'cell', or small unit of the system, instead of single molecules. The statistical genesis of the process of liquid penetration in fibrous media can be regarded as the interaction and the resulting balance among the media and liquid cells that comprise the ensemble. This process is driven by the difference of internal energy of the system after and before a liquid moves from one cell to the other.

In the 1990s, Manna *et al.* [162] presented a 2D stochastic simulation of the shape of a liquid drop on a wall due to gravity. The simulation was based on the so called

Ising model and Kawasaki dynamics. Lukkarinen [163] studied the mechanisms of fluid droplets spreading on flat solids using a similar model. However, these studies dealt only with flow problems on a flat surface instead of a real heterogeneous structure. Only recently has the Ising model been used in the simulation of wetting dynamics in heterogeneous fibrous structures [104–108]:

Ising's model was combined with Monte Carlo (MC) simulation in the study of liquid penetration through fibrous media. This transport process, in a discrete system, is driven by the difference of system energies after and before a liquid moves from one cell to another, subject to random effect. Accordingly, Monte Carlo method was incorporated to represent the stochastic nature of the evolvement of the system. Therefore, the actual configuration was determined by the competition of a deterministic factor (energy difference) and a random factor represented in MC simulation. By repeating discrete time steps in the simulation, a picture of the system evolvement, that is, the transport process, can be predicted.

As a 'meso-scale' approach, stochastic models and simulations deal with discrete and digitalized cells or subsystems instead of individual molecules. They lead to considerable reduction of computational cost, naturally. Detailed information about these simulation techniques will be discussed in Section 8, dedicated to multi-scale approaches, which represent examples of micro- and meso-scale methods in the study of liquid transport phenomena in fibrous materials.

3.6 Summary

Wicking and/or wetting are among the most frequently encountered phenomena when processing and using fibrous materials. Wetting is a process of displacing a solid–air interface with a solid–liquid interface, while wicking is a result of spontaneous wetting in a capillary system.

The subject of wetting and capillary wicking has been a complex topic attracting extensive research interests in both theoretical and experimental physics. The special structure of fibrous materials further complicates the problem of liquid transport behaviors in porous media of intricate, tortuous and yet soft structure, which may be subject to change due to imbibitions.

In this section, recent advances in studying wetting and wicking behaviors on a single fiber/filament as well as through fibrous assemblies have been reviewed. In addition to wetting theories and the various testing techniques, a couple of computer simulation methods have been briefly mentioned. Additional, more intensive research work is demanded, of course, before a comprehensive understanding of the behaviors of liquid wetting/wicking in fibrous materials can be achieved.

4. RESIN IMPREGNATION IN LIQUID COMPOSITE MOLDING (LCM)

4.1 Introduction

Liquid composite molding (LCM) includes resin transfer molding (RTM) and its variants such as vacuum assisted resin transfer molding (VARTM) and structural reaction injection molding (SRIM), during which behavior of the resin flowing through reinforced fiber networks in mold filling is an essential factor that influences the ultimate quality of products. Extensive amounts of research have therefore been

concentrated on the process of resin impregnation in LCM, which is characterized by high fluid viscosity as well as high temperature and pressure during the process.

4.2 Mechanisms of Resin Impregnation in Fibrous Structures

For example, RTM consists of a mold cavity that is in the shape of the part to be manufactured (see Fig. 20). The fibrous preform is placed in the cavity. Then the mold is closed and clamped or held under pressure in a press. The resin is injected into the compressed preform through one or several inlets. The air that has been expelled by resin from the voids and interstices in the fibrous preform is released by one or several vent ports. The whole process of impregnation for a thermoplastic binder occurs above its melting temperature [164, 165]. After the mold is filled, it is cooled before the finished solidified composite part is taken out by demolding. For liquid thermosetting resins, the liquid resin cures (solidifies) with continued heat application and so the part can be demolded hot.

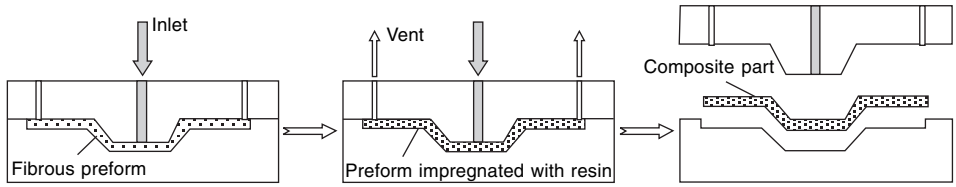

Fig. 20 Schematic resin transfer molding (RTM) process

During the impregnation process in RTM, the high viscosity resin flows to fill a maze of flow channels and paths created by the heterogeneous, porous fiber structures. Fiber preforms with different geometries or fiber arrangements will offer different resistances to the flow. Even in a single fibrous preform, diameters of the flow channels or pores may distribute in different scales: macro-scale pores formed by inter-tow spaces and meso-scale pores formed by intra-tow spaces. Also, fluid viscosity will vary throughout the mold due to its dependence on temperature and shear rate of the fluid, which change throughout the mold. Lastly, the capillary and surface tension effects may become significant in determining the flow pattern. This renders the physics of the process quite different from that of flow in an empty mold [166].

Fiber preforms for LCM composite fabrication are usually composed of knitted or woven layers from fiber tows, which allow for high fiber volume fractions and easy tailoring. This type of fiber preform includes dual scale pore structures; that is, spaces between the fibers in a single tow/yarn that are in the order of the fiber diameter (intra-tow spaces, 5-20μm), and spaces between the fibers tows/yarns that are of the order of millimeters (inter-tow spaces) [166].

Physically, the resin movement is prompted by the pressure gradient and capillary action, and is resisted by viscous forces. Therefore, the pressure experienced by the system of resin/fibrous preform during LCM processing can usually be separated into the hydrodynamic part (corresponding to the external applied pressure) and the capillary part (resulting from the surface tension effect) [167–173]. These two types of flow behaviors cause non-uniformity in the resin progression. This non-uniformity can occur in both directions, along and across the fiber tows.

In the flow along the fiber tows, where capillary action is much stronger than in

the flow across the tows, two situations can be found, namely, the wicking flow front inside the fiber tow can be either advanced or delayed with respect to the primary front in the inter-tow spaces, which results in either inter-tow or intra-tow void formation, respectively, as shown in Fig. 21 [169]. Capillary action is but a function of the resin surface tension, resin/fiber interfacial tension and geometry, and is independent of the applied external pressure. On the one hand, therefore, if the flow rate caused by the external pressure is relatively high, viscous action will dominant over capillary action, and inter-tow spaces, which have the higher permeability, will be filled first, leading to intra-tow voids, as shown in Fig. 21 (b). On the other hand, under lower external pressure and lower flow rate, wicking flow can dominate the flow driven by external pressure. As a result, resin will advance more rapidly inside the tow and inter-tow voids become more dominant, as shown in Fig. 21 (a). The balance between viscous flow and capillary flow is also of concern in practice during LCM manufacturing, for higher external pressure is known to be favorable in reducing the filling time as well as the cost, while lower external pressure contributes to a better impregnation and adhesion at the resin/fiber interface.

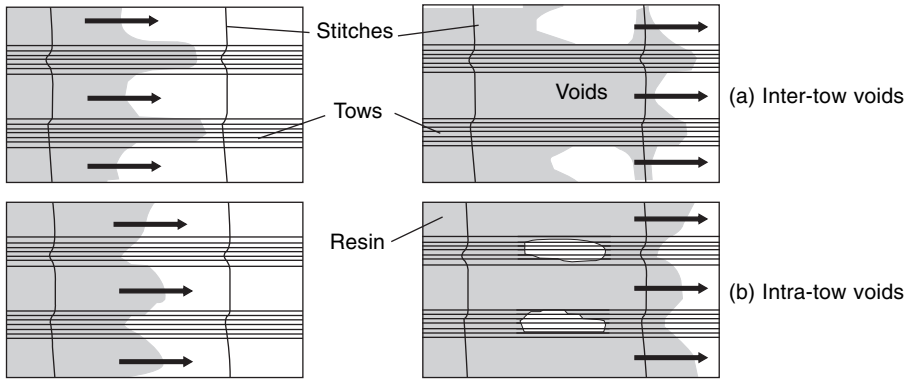

Fig. 21 Inter-tow and intra-tow voids formation in longitudinal direction

In the case of flow across the fiber tows, both experiment [174] and numerical prediction [175–177] show that filling into the fiber tows is delayed behind the flow front due to a much lower intra-tow permeability, as shown in Fig. 22. What is more, very high external pressure acting on the tows can significantly change the fiber positions and hence close some capillary channels between them, thus further decreasing the intra-tow permeability. Usually, only a thin layer of resin is penetrating the tows when the primary resin front encircles them, then the air is compressed inside the tow until it is balanced with the surrounding resin pressure. Hence, the capillary action becomes the only force that can drive the resin into the tow. When the air pressure grows higher than the surrounding pressure, the air can escape from the tow in the form of micro-voids, usually in the direction of higher permeability, which is along the fiber tow [169].

In fluid mechanics, distinctions are made between the saturated flow region, where the preform has been wetted through so that only a single phase fluid (resin) need to

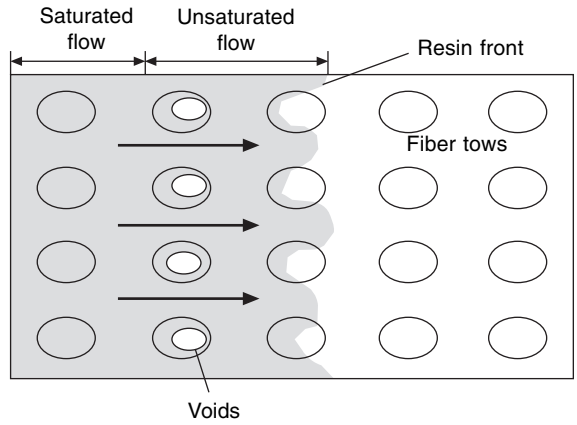

Fig. 22 Void formation in cross section of fiber tows

be considered, and the unsaturated region, where dry spots or voids exist and dual phase fluid (resin and air) should be considered, as shown in Fig. 22.

4.3 Theories and Computational Approaches in Studying Resin Impregnation Behaviors

Reported theories and models in studying resin impregnation behaviors can usually be divided into two categories: macroscopic process models to predict movement of the free surface flow front during flow of a shear thinning fluid through a complex 3D mold geometry, coupled with the heat transfer; and microscopic ones addressing issues such as insufficient fiber wetting and the local heterogeneous nature of fibrous preforms.

4.3.1 Theoretical Models

On the macroscopic scale, practice has been concentrated on describing resin flow through the fiber preform with the empirical Darcy's law. It assumes that the flow rate (u) of the fluid through a porous medium is directly proportional to the pressure gradient, ∇p:

$$u = \frac{K}{\mu} \cdot \nabla p \tag{68}$$

where u is the average velocity, μ the Newtonian viscosity of the fluid, ∇p the pressure gradient, and K the permeability. In the case of anisotropic media, the permeability K is a tensor.

The permeability K can be obtained experimentally [178], which will be discussed in the next section. Or it can be semi-empirically derived from the fiber volume fraction by the well-known Kozeny–Carman relation, treating the porous medium as a bundle of parallel tubes and resulting in the formula:

$$K_x = k_x \frac{(1 - v_f)^3}{v_f} \tag{69}$$

where K_x is the permeability in the fiber direction, v_f is the fiber volume fraction, and k_x is the Kozeny constant depending on the preform architecture, and has to be determined experimentally.

For flow transverse to the fiber tow, the Kozeny–Carman relation was modified to take into account the effect of the maximum packing limit (to prevent transverse flow of resin from fiber tows) of the fiber volume fraction [179]:

$$K_z = k_z \frac{(\sqrt{V_a/V_f} - 1)^3}{(V_a/V_f + 1)} \tag{70}$$

where V_a is the available fiber volume fraction at which the transverse flow stops.

There are also analytical models for calculating permeability of aligned-fabric reinforcement without empirical constants. Gebart [180] adopted a lubrication approximation in estimating pressure drop in the narrow gaps between adjacent fibers, and derived expressions of permeability for quadratic and hexagonal arrangements of fibers. Cai and Berdichevsky proposed a self-consistent method [181, 182], which assumes that a unit cell of a heterogeneous medium can be considered as being embedded in an equivalent homogeneous one whose properties are to be determined. Then the flow inside the unit cell satisfies the Navier–Stokes equation while the outside of the unit cell follows Darcy's law.

A preform will normally consist of a number of layers of fiber mats, sometimes of different materials, stacked in different orientations. Accordingly, models have been developed to predict the average in-plane permeability of the preform, given the orientations and permeabilities of the individual layers. One of the frequently adopted methods is to find the gap-wise averaged permeability by applying Darcy's law to saturated flow through parallel layers of different permeabilities, assuming that no through-thickness flow occurs. The gap-wise averaged permeability K for a lay-up of n layers, each of thickness h_i with permeability k_i, will be given by [183]

$$K = \frac{1}{H} \sum_{i=1}^{n} h_i k_i, \quad \text{where} \quad H = \sum_{i=1}^{n} h_i \tag{71}$$

However, this equation only provides satisfactory results for preforms in which the in-plane permeabilities of the different layers do not vary greatly, and may break down in the case where different layers have very different in-plane permeabilities, such as a (0, 90) lay-up of unidirectional fiber mats [166].

Early attempts in the study of the resin impregnation process usually described the flow in ideal fiber beds on the basis of perfectly spaced and aligned arrays of cylinders. Their application to real fabric reinforcement was therefore limited due to conditions that exist in real cases but are often neglected for the sake of simplicity in computation:

(i) Non-uniformity in pore size distribution (from inter-tow to intra-tow)
(ii) Surface effect at the interface between fiber/resin
(iii) Non-isothermal effect throughout the mold during impregnation
(iv) Compaction and deformation of preforms during resin impregnation.

Accordingly, much work has recently been dedicated to dealing with these conditions.

Multilevel analysis of the resin transport process in fibrous preforms consists of

macro-level analysis of inter-tow flow and meso-level study of intra-tow flow [170, 171]. Both experimental and modeling results were reported to cover the wide span of length scales over which flow in porous media can occur in a single fibrous material [174, 184, 185]. Also reported is the idea that many of the discrepancies in the literature in interpreting macroscopic flow behaviors in fibrous materials may be due to neglect of the effects of microscopic flow phenomena [174], especially in the partially-saturated resin close to the flow front, where a transient impregnation process takes place during which micropores are filled by resin [171, 186–189].

Despite the importance of capillary action and surface/interface tension in determining the behavior of resin flow into fibrous materials [167, 170–173, 184, 190–193], they were often ignored or oversimplified in many models so as to avoid complicated computations:

Binetruy [171] focused on modeling the hydrodynamic interactions between flows that occur outside and inside fiber tows during LCM. The geometric configuration chosen to simulate a heterogeneous medium was an axial tow (with micropores inside) embedded in a composite region of higher permeability (including macropores). And the model dealt with both the global motion of resin in the macropores and the impregnation of micropores, simultaneously, by introducing a boundary condition at the tow surface which accounts for interactions between the two flow scales.

Lekakou *et al*. [172] proposed a mathematical model to describe macro and micro infiltration through reinforcements of bimodal porosity distribution in LCM. The model was based on Darcy's law incorporating mechanical, capillary and vacuum pressures:

$$U^{\text{sup}} = \frac{K}{\mu} \nabla (P^{\text{mech}} + P^{V} + P^{c}) \tag{72}$$

where U^{sup} is the superficial velocity, K the permeability tensor, P^{mech}, P^{V} and P^{c} are mechanical injection pressure, vacuum pressure and capillary pressure respectively. The capillary pressure is generally given by the Young–Laplace equation:

$$P^{c} = \frac{4\sigma \cos \theta}{D_e} \tag{73}$$

where σ is the surface tension of the wetting liquid, θ the contact angle between liquid/fiber, and D_e the equivalent wetted pre-diameter, which is again an average property of a fibrous material requiring empirical determination [186, 193].

There are also works incorporating other more realistic conditions, such as the non-isothermal effect [188, 194–196] and preform compaction/deformation [197]. These usually involve complicated equations whose solutions require such numerical techniques as Control Volume (CV) [195, 198–203], Finite Element Methods (FEM) [176, 182, 194–196, 199–212], and the Lattice Boltzmann (LB) Method [175, 213, 214]. Additional attempts include statistical mechanics modeling and simulation techniques [215, 216], which derive macro flow behaviors of resin in fibrous materials from the interaction of the system's micro components, instead of using empirical Darcy's law. These numerical methods and simulation techniques are discussed in the next section.

4.3.2 Numerical Methods and Simulation

Most of the numerical solutions to the behavior of resin during impregnation into fibrous structures are based on Darcy's law in Equation (68). These numerical methods as mentioned above include the Finite Difference Method [217–219], the Boundary Element Method [220–224], the Control Volume Method [195, 198–203], the Finite Element Method [176, 182, 194–196, 199–212, 225–228], or any combination of them [195, 199–203, 217, 225, 228–230].

Both the finite difference and the boundary element methods are based on the moving boundary approach. The discretized domain only covers the section of the mold that is filled with fluid, and is updated at each time-step as the flow front progresses. They have the disadvantage that the mesh needs to be updated at each time step, involving additional computational cost. The complexity in remeshing schemes also occurs when two flow fronts meet and the mesh boundaries need to be merged. In addition, the finite difference method requires use of a boundary-fitted coordinate system to mesh the fluid domain in a computationally efficient manner. As a result, the boundary of the fluid domain has to be continuous. This limits its application in multiple connected domains and in complicated boundary conditions. To overcome these problems, the FEM can be combined with the CV approach, allowing the discretization of the whole mold domain at the onset of the simulation [166]. Accordingly, FEM and CV are reported to be the most versatile and popular ways to solve LCM mold filling problems, because of their simplicity in handling the moving boundary [195, 199–203, 229, 231–239].

A typical FEM for modeling flow within a LCM mold uses Darcy's law as a momentum equation, as shown in Equation (68). And the continuity equation is

$$\frac{\partial \rho}{\partial t} + \nabla \cdot (\rho u) = 0 \tag{74}$$

For an incompressible fluid flow under a quasi-steady state, the transient term on the left-hand side can be removed:

$$\nabla \cdot u = 0 \tag{75}$$

The substitution of Equation (68) into (75) results in the following governing equation:

$$\nabla \cdot \left(\frac{K}{\mu} \cdot \nabla p \right) = 0 \tag{76}$$

As the resin flows through the fibrous media, heat transfer takes place between the mold wall, fiber and resin in the non-isothermal processes. Therefore, a heat transfer model should be applied jointly. It was shown that the thermal equilibrium assumption is valid for slow processes such as LCM in which the resin and fiber have the same temperature at the contact point. Thus, the energy equation governing the heat transfer in fibrous materials being impregnated by resin is:

$$\rho C_p \frac{\partial T}{\partial t} + \rho_r C_{pr} (u \cdot \nabla T) = \nabla \cdot k \nabla T + \varphi \Delta H G \tag{77}$$

where the two terms on the left-hand side of the equation represent the net increase of the system energy, and the two terms on the right-hand side indicate the energy

flow into/out of the boundary and the generated energy, respectively. φ is the porosity of the fibrous material, ΔH the heat of reaction, and G the reaction rate. The effective thermal conductivity k, density ρ and specific heat C_p may be expressed as:

$$k = \frac{k_r k_f}{k_r \omega_f + k_f \omega_r} \quad \rho = \frac{\rho_r \rho_f}{\rho_r \omega_f + \rho_f \omega_r} \quad C_p = C_{pr}\omega_r + C_{pf}\omega_f \tag{78}$$

where ω the is the weight fraction, and subscripts r and f denote resin and fiber, respectively.

In CV/FEM, the plane or space of the mold to be filled is first divided into a finite number of elements by a fixed grid of 2-D or 3-D. Control volumes then are constructed to associate with each mesh node. Take a 2-D model for example, as shown in Fig. 23; this could be achieved by joining the midpoint of each edge of an element to the center of the element [232].

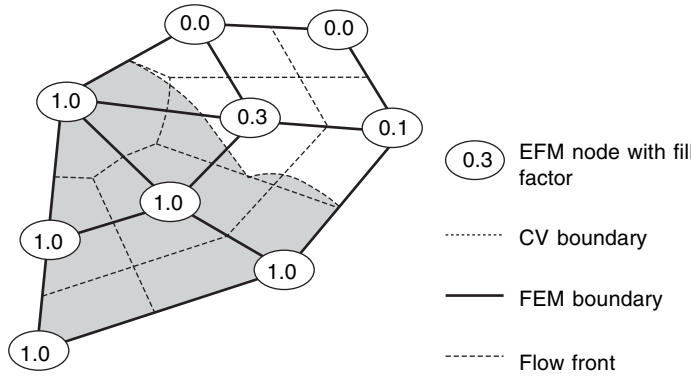

Fig. 23 Finite elements, control volumes and fill factors

The status of each control volume is represented by a nodal fill factor, f, which represents the ratio of volume occupied by the resin to its total pore volume. For an empty control volume, $f = 0$, and for a control volume completely filled with resin $f = 1$. The flow front consists of control volumes that are adjacent to filled control volumes and are not completely filled ($0 < f < 1$). Therefore, the solution domain includes all filled control volumes, where pressure is calculated within using FEM.

There is also research work on mold-filling problems based on FEM [176, 196, 204–212, 225–228]. Due to the amount of computation involved in FEM calculation, some of the work uses commercial FEM software such as ANSYS FLOTRAN [169, 227] and ABAQUS [226].

In addition to the traditional numerical method based on discretization of partial differential equations, there are approaches involving introduction of discrete models, and derivation of the corresponding macroscopic equations through multi-scale analysis. These approaches in dealing with LCM mold-filling processes include the Lattice Boltzmann method [175, 213, 214], the random walk method [215], and the Monte Carlo method [216]. Detailed information about these will be discussed in Section 8.

4.4 Experimental and Characterization Techniques

Usually, objectives of experiment and characterization techniques in the studies of the LCM process include:

(i) measuring the permeability and/or capillary properties of a fibrous structure, and
(ii) recording the flow front and/or void formation during the mold-filling process.

Many researchers have conducted flow experiments to measure the permeabilities of the fiber preforms as a function of the preform architecture and the fiber volume fraction. In-plane permeability can be measured either by a unidirectional flow [180, 240] or by a radial flow [183, 223, 241, 242] method, while transverse permeability can be measured by trans-plane flow methods [243].

If the principle fabric directions can be easily defined in such cases as the unidirectional or bidirectional fabric mats, the in-plane permeability can be easily measured by laying the fabric reinforcement in a rectangular shape flow channel with fibers aligned along or perpendicular to the flow direction. If the principal fabric directions cannot be determined easily, in such cases as random fiber mats, multidirectional mats, and braided preforms, it is necessary to measure the effective permeability for three or more fabric orientations so as to determine the principal permeabilities and the orientation of the principal flow axis relative to the fiber direction.

Among the two most widely used methods of characterizing the flow in LCM, the unidirectional experiment allows the unsaturated flow data to be directly compared to the saturated flow data, providing insight into differences that may be expected during moldings as compared to pure permeability-based flow behavior [174, 244]. The unidirectional flow experiments are typically conducted in flat molds with a transparent top of glass or acrylic sheet, as shown in Fig. 24.

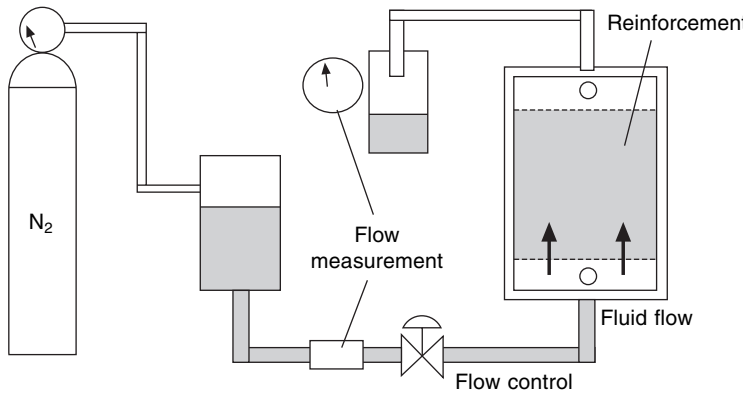

Fig. 24 Unidirectional flow experiments for measuring in-plane permeability

Saturated flow experiments are conducted by forcing a test fluid through the mold and measuring the steady-state relationship between the flow and pressure drop across the length of the mold. Pressures at the mold inlet are measured by transducers mounted at positions on the back face of the mold located at the lower boundary of

the reinforcement. Pressure at the outlet is assumed equal to the ambient atmosphere. For a test fluid with a newtonian rheology, a linear relationship is expected between the steady-state flows and pressure drops. Then the permeability can be derived from Darcy's law [177].

One of the problems of measuring the in-plane permeability by the unidirectional experiment is its sensitivity to edge effect, which is a function of the mold size. Eliminating the edge effect requires either sealing the edge of the preform to the mold side or designing the mold tooling to seal the edge during the closure procedure. Another drawback of the unidirectional flow method is that it is time consuming. Several experiments are necessary to determine the components of permeability tensor. To reduce experiment time, radial experiments have been developed to determine multiple components of permeability in the plane of the sample with a single, fast experiment, thereby avoiding the edge effects. The radial flow experimental setting is similar to that of the unidirectional experiment, except that the inlet is placed at the center of the transparent top, and outlets are drilled at the corners of the mold. With collected data of radial flow rate and pressure drops, the directional in-plane permeabilities as well as the directions of the principal axes can be further derived from analysis based on Darcy's law [183, 223, 241, 242].

In addition to experimental methods involving measurement of flow under external applied pressure, there has been experimental work investigating capillary action during LCM, with similar settings as discussed above except that no external pressure is applied. In this case, the only driving force for the resin impregnation is capillary pressure [167, 191, 245, 246]. The duration of a capillary experiment can be as long as a month to give desirable accuracy [245].

These experimental settings for measuring permeabilities can also be used to visualize flow behaviors during mold filling through the transparent top. Information concerning advancement of the flow front can be obtained either through video techniques [247–249] and/or sensors [249–251], and used to verify the various theories and models of LCM processes [178, 180, 187, 191, 207, 210, 222, 247–253].

4.5 Summary

Because it is a major influence on the quality of products, flowing behavior of resin through fiber network reinforcement in liquid composite molding has been object of a lot of research work.

Resin movement is physically prompted by pressure gradient and capillary action, and is resisted by viscous forces. Fiber preforms with different geometries or fiber arrangements will pose different resistances to the flow. Even in a single fibrous preform, diameters of the flow channels or pores may distribute in different scales: macro-scale pores formed by inter-tow spaces and meso-scale pores formed by intra-tow spaces. This is why pressure experienced by resin/fibrous preforms during LCM processing can usually be separated into two parts: a hydrodynamic part, which contributes mostly to inter-tow flow behavior, and a capillary part, which fulfils the intra-tow impregnation. These two types of flow behaviors cause non-uniformity in the resin progression and lead to void formation after the flow front.

Most of the theories and models in studying LCM processes are based on the empirical Darcy's law. Now, analytical methods have also been developed from

simple 1-dimentional models to 2-D and 3-D tensor analysis and numerical approaches, to better simulate more realistic conditions during LCM processes. In addition to these are approaches involving the introduction of discrete models and derivation of corresponding macroscopic equations through multi-scale analysis. The most frequently used experimental methods of characterization in LCM studies are unidirectional and radial experiments, where, by means of the measurement of fluid flow rate and pressure drop across the sample preform under a steady state, the permeability can be derived from Darcy's law. These experimental techniques can also be employed to validate the various flow theories and models of LCM.

5. FILTRATION AND SEPARATION IN GEOTEXTILES

5.1 Introduction

The ASTM definition for a geotextile is: Any permeable textile material used with soil, rock, earth, or any other geotechnical engineering related materials, as an integral part of a man-made project, structure or system [254]. Geotextiles are permeable fabrics which are able to hold back solid materials while letting water flow through. They have been in extensive use for about 30 years as drainage, separation and filter materials in geotechnical and geo-environmental works, due to their low cost, consistent properties, and ease of placement. Accordingly, considerable work has been carried out on the transport behavior of geotextiles to optimize their performance and efficiency.

5.2 Mechanisms of Filtration and Separation by Fibrous Geo-filters

The basic objective of geotextiles is to allow water to flow through the filter into the drain over the life of the project while retaining soil particles in place and preventing them from migrating through the filter [255]. The performance of geotextiles usually depends on [256]:

(i) Pore structure of the geotextile
(ii) Ability of the soil to retain its own shape or its internal stability
(iii) Flow conditions, i.e. the seepage velocities and hydraulic gradients.

To secure particle retention and maintain the desired flow capacity at the same time, three simple requirements should be satisfied for an effective filter:

(i) If the size of the largest pore in the geotextile filter is smaller than the larger particles of the soil, the soil will not pass the filter. Instead, its larger particles will form a filter bridge (cake) over the hole, and only the smaller ones will be filtered (see Fig. 25) [257].
(ii) If the majority of openings in the geotextile are sufficiently larger than the smaller particles of the soil, then they will be able to pass through the filter, and the geotextile will not clog or blind, as shown in Fig. 26 [257].
(iii) If a large number of openings are present in the geotextile, the proper flow can be maintained even if a portion of the openings become clogged during the design life of the filter.

To be more specific, we speak of five basic filter criteria when selecting or/and designing a geotextile [258, 259]:

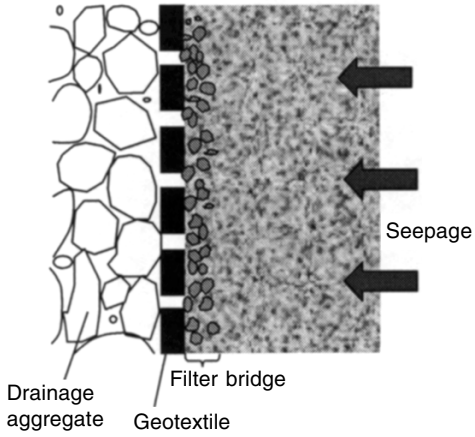

Fig. 25 Filter bridge formation

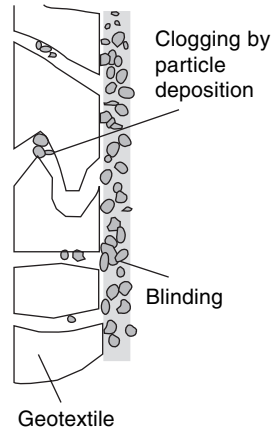

Fig. 26 Clogging and blinding

(i) Good capacity of retention to ensure that no soil particles will migrate through the geotextile,
(ii) Good permeability to allow free flow of liquid through the geotextile,
(iii) Non-clogging, so that the geotextile will adequately meet the permeability and retention criteria throughout the life of the structure.
(iv) Good survivability to ensure that the geotextile is strong enough to survive its installation.
(v) Good durability to ensure that the geotextile is resistant enough to withstand adverse chemical and ultraviolet light exposure for the design life of the project.

Different types of geotextiles have been developed and applied. In general they are made from synthetic fibers such as polypropylene (PP), polyester (PET), and polyamide (nylon), or polyethylene (PE), in either woven or nonwoven forms. A woven geotextile could be manufactured from monofilament, multifilament, and slit-film or fibrillated fibers. A nonwoven geotextile could be fabricated from either continuous filaments or staple fibers. Woven geotextiles have pore sizes within a relatively narrower range than nonwovens because of the limitations in the manufacturing process, including the number of warp and weft yarns used and types of weave.

5.3 Testing and Characterization Techniques

Up to now, most work in the field of geotextiles has been experimental, and most designs have been based on empirical criteria. Current testing and characterization techniques for geotextiles are usually adopted to measure such properties as porosity, pore size and distribution, permittivity, and transmissivity.

5.3.1 Measurement of Pore Size and Pore Size Distribution

Geotextile design, especially for soil retention, is generally based upon relationships developed between an indicative pore size and/or pore size distribution of the geotextile and the grain size of the soil.

In the U.S. most geotextile filter design methods use the apparent opening size (AOS), or O_{95}, as the pore size to control retention. The AOS or O_{95} is defined as the

pore size at which 95% of the pores are smaller than the grain size of the soil. O_{95} is most frequently evaluated by the *dry sieving method*. The method involves sieving uniform and rounded sand particles or glass beads through the geotextile and measuring the particle/bead size at which only 5% or less, by weight, passes through the geotextile, in accordance with the ASTM D4751 standard [260]. In this method, an anti-static spray is usually applied uniformly over the surface of the geotextile specimens to prevent static electricity from being generated during the test. Still, electrostatic effects are reported to occur with fine particles, even with the application of anti-static spray. And, glass beads may stick to geotextile fibers, making the pore effectively smaller, besides agglomerating into a mass that is too large to pass through the geotextile. Also, the dry sieving test is time-consuming, usually requiring two hours for one test [261]. This makes it impractical as a quality control tool in the manufacturing facility and discourages its use by the engineers [257].

In Canadian standards, a *hydrodynamic sieving method* is also used to determine the O_{95} of a geotextile. In the hydrodynamic sieving test, glass bead mixtures are sieved through geotextiles by alternating water flows, which occur as the result of repeated immersion of the geotextile in water [260, 262, 263]. The hydrodynamic sieving test reduces the problem of static. However, it is even more time-consuming, because the initial immersion cycles are very long, and need a long time to stabilize. Another problem is the possible occurrence of blinding during testing [260, 261].

A *wet sieving method* is standardized in Europe for evaluating the O_{95} and O_{90}. It is similar to the dry sieving method except that a continuous water spray is applied to the particles and the geotextile during constant shaking of the sample, and, rather than uniformly sized particles, a mixture of differently sized particles is used for the test. Continuous water spray for the wet sieving method is intended to reduce electrostatic conditions associated with glass beads, while use of a particle mixture decreases the time required to perform a test. Still, it is reported that glass beads tend to agglomerate on the surface of the geotextile due to the meniscus tension of glass beads [260, 261].

The *bubble point method* (ASTM F316) is based on the principle that a porous material will allow a fluid to pass only when the pressure applied exceeds the capillary attraction of the fluid in the largest pore. In this dynamic test, a geotextile specimen is saturated with a fluid before gas pressure on the upstream face of the wetted geotextile is slowly increased. At a critical pressure, the first air bubble(s) will come through the largest constriction(s) in the wetted geotextile. Based on the theory of capillary flow, the diameter of the largest pore can be calculated [264]. The bubble point test is rapid to perform; approximately twenty minutes per test. And it is commented that the bubble point method is advantageous in comparison with other types of tests because it simulates flow of the fluid in the geotextile pore channels, it can be performed efficiently, and the results are repeatable [265, 266].

The *mercury intrusion porosimetry method* applied to geotextiles is a variation of the standard for the determination of pore volume and volume distribution in soil and rock (ASTM D 4404). This static method does not measure pores in a geotextile as continuous pore channels, as in the bubble point test, but as singular pores [267, 268]. This method is based on the Washburn equation, which relates the pressure required to force a non-wetting fluid (mercury) into the pores of a geotextile so that the entire pore opening is filled with mercury. And a relationship can be found between size of

the pores and pressure applied. Then, the pore volume and pore volume distribution of the geotextile can be determined, where pores are assumed to be cylindrical. This test is also quite rapid. However, it gives a pore-size distribution based on total pore volume and gives no information regarding the number of pores and pore constrictions of the geotextile [260, 261].

In another method, *image analysis*, an image of the geotextile is scanned and converted to a digital image that can be enhanced for measurements. Various mathematical morphology algorithms are used. Relevant measurements obtained are porosity, pore size distribution, total area of fibers, percentage of fibers, density of fibers, and distance between fibers [260, 261, 268–271].

5.3.2 Measurement of Hydraulic Behavior of Filtering Materials

Hydraulic behaviors of geotextile filters include their permeability to water and water retention. The former can be characterized by either the cross-plane permittivity test (filtration) or the in-plane transmissivity test (drainage) [272], and the latter is usually represented by a water characteristic curve.

The apparatus for the *permittivity test* under confinement, based on ASTM D 5493, is shown in Fig. 27. A steel piston applies a normal load to a rigid plate on a geotextile specimen, confined between two sets of steel meshes. The meshes serve as a permeable medium that helps to distribute the normal stress uniformly onto the geotextile specimen [272, 273].

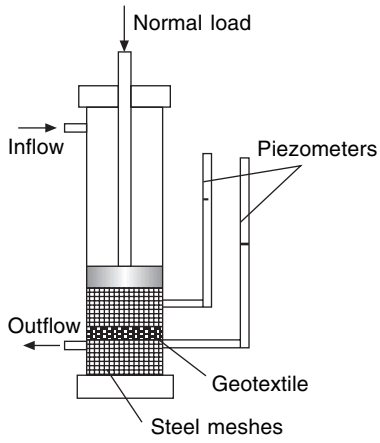

Fig. 27 Permittivity test apparatus

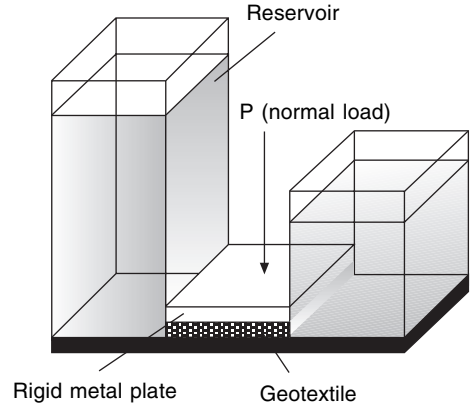

Fig. 28 Transmissivity test equipment

The equipment used for the *transmissivity tests*, based on ASTM D 4716, is shown in Fig. 28. The geotextile specimen is subjected to normal stress applied also by a rigid metal plate [272, 273].

Distilled water is used in both permittivity and transmissivity tests. The recorded pressure gradient is used to determine the in-plane and transverse permeability of the geotextile by means of Darcy's law.

A soil–water characteristic curve has long been used in geotechnical engineering to assess the water retention of unsaturated soils [274–276]. It has been adopted in

recent years also to characterize the water retention behavior of geotextiles [277, 278]. A schematic of a geotextile water characteristic curve is shown in Fig. 29. It describes the water storage capacity of a geotextile subjected to various suctions. It also contains important information regarding the amount of water contained in the pores at any given suction and pore size distribution related to the state of stress in the water–geotextile system.

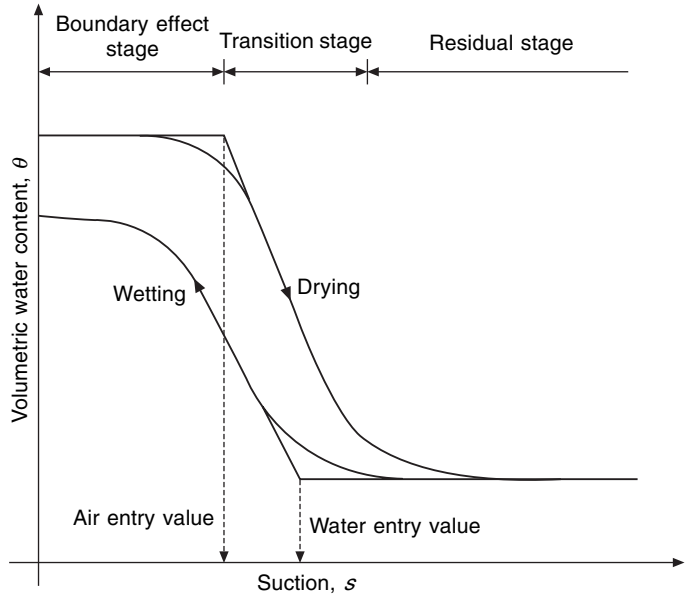

Fig. 29 Schematic of geotextile–water characteristic curve [277]

Water characteristic curves in both drying and wetting phases can be obtained using a hanging column test [279, 280]. A circular shaped geotextile specimen is placed on a ceramic plate and suction is applied by raising or lowering the level of a water tank connected by a tube to one side of the porous plate. Hydraulic equilibrium is achieved at each suction level after approximately 24–48 hours. Then the specimen is weighed to measure water content. Usually a high value of equilibrium suction is initially applied and then incrementally reduced to zero in order to obtain the wetting curve. The drying phase curve is obtained by repeating this procedure in reverse.

5.3.3 Combined Testing Approaches

The above testing approaches involve testing only the porous structure of filtering materials and their permeability to water. To clarify the filtration behavior of a geotextile to a soil specimen, the *gradient ratio test* can be used. According to ASTM D5101, the gradient ratio test apparatus includes a rigid wall permeameter accommodating a cylindrical soil specimen and geotextile specimen, as shown in Fig. 30 [281–283]. Water is passed through the system by applying various total differential heads. Measurements of the hydraulic head are taken at several ports, as shown in Fig. 30, and used to establish the variation of hydraulic gradient through the soil specimen

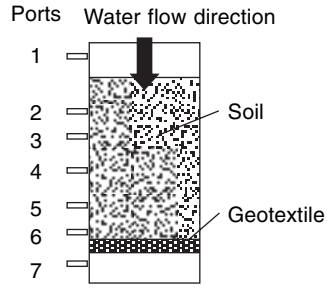

Fig. 30 Gradient ratio test apparatus

and across the geotextile specimen. Flow rates through the system are determined and used to calculate the permeability of the composite system. This method can also lead to an assessment of soil/geotextile compatibility, which is characterized by no unacceptable piping of soil through the geotextile or clogging of soil near the surface of the geotextile [281, 283–285].

In recent years, a device for gradient ratio test under dynamic cyclic flow was introduced to test the performance of geotextiles under cyclic flow instead of a steady state flow, since dynamic cyclic flow is typical in marine protection works [286], and the retention criteria used for geotextile filters in cyclic flow are more restrictive than those for steady state flow [287, 288].

Various laboratory testing and characterization test methods have been compared for studying the behavior of geotextile/soil filtration systems. However, there has not been a consensus on which one of these methods is the most appropriate or accurate [261, 267, 271, 273, 289–291]. In order to develop reliable design criteria, several approaches are often combined to provide more comprehensive information on the performance of a geotextile [271, 287, 291].

In addition to laboratory tests, field tests were also used to assess the performance of geotextiles under conditions of their actual use and operation. Geotextile samples are exhumed from the field testing sites, usually after long-term exposure, and analyzed in the laboratory [291–296].

5.4 Theories and Analytical Approaches

On the topic of filtration and separation in geotextiles, theoretical studies are much less readily available than experimental ones. Further, most of the theories are empirical.

The governing equation of transient flow within a porous geotextile can be derived from both Darcy's law and the continuity condition [277, 297], and expressed as:

$$k_x \frac{\partial^2 h}{\partial x^2} + k_y \frac{\partial^2 h}{\partial y^2} = \frac{\partial \theta}{\partial t} = m_w \gamma_w \frac{\partial h}{\partial t} \tag{79}$$

where h is the total hydraulic head, k_x and k_y the permeability or hydraulic conductivity in unsaturated condition for the two directions respectively, m_w the coefficient of water volume change (slope of the water characteristic curve), γ_w the unit weight of water, and θ the volumetric water content (dimensionless).

In Equation (79), the hydraulic conductivity, k, and the coefficient of water volume change, m_w, are material specifics and functions of the pore pressure. In addition to

experimental approaches for obtaining these parameters, various functions and/or models for water characteristic curves and hydraulic conductivity have been proposed, from unsaturated soils to unsaturated geotextiles. Among these, van Genuchten's equations are some of the most popular mathematical forms [277, 298, 299]:

A three parameter equation is suggested by [298] to describe the relationship between normalized volumetric water content, Θ, and suction, s:

$$\Theta = \frac{\theta - \theta_r}{\theta_s - \theta_r} = \left[\frac{1}{1 + (\alpha(s/\gamma_m))^n}\right]^m \tag{80}$$

where θ, θ_s, θ_r are the water contents at a given suction, saturated water content, and residual water content, respectively, and are defined as shown in Fig. 29. There are also three fitting parameter: α, n and m.

And the hydraulic conductivity function is given as [298]:

$$k_r(\Theta) = \frac{k(\Theta)}{k_{\text{sat}}} = \Theta^{1/2}[1 - (1 - \Theta^{1/m})^m]^2 \tag{81}$$

where k_r, $k(\Theta)$ and k_{sat} are the relative hydraulic conductivity, the hydraulic conductivity at given normalized volumetric and water content, and saturated hydraulic conductivity, respectively.

Several corrections on these equations have been suggested [300, 301], and alternative equations are available [278, 302]. Still, these are quite empirical and must be combined with experiments so as to derive better fitting parameters.

Besides the above mentioned macroscopic descriptions of the transport process in geotextiles, microscopic description of the filtration process has also been investigated by researchers to describe the stochastic nature of particle transport [303], including the Markov process [304] and the Monte Carlo simulation [305].

5.5 Summary

An important textile material, used frequently in civil engineering for separation, filtration and drainage for decades, geotextile has received extensive attention from researchers in their efforts to optimize its design.

A large portion of the research work has been concentrated on testing and experimental characterization of structure and/or hydraulic behavior, including pore size and pore size distribution, permeability, and the soil transport process in geotextiles. Some of the frequently adopted approaches have been standardized, mainly by ASTM. Theoretical work is obviously less available than experimental studies. Furthermore, most of the theories are empirical.

6. AEROSOL FILTRATION BY FIBROUS FILTERS

6.1 Introduction

As one of the commonest methods of separating and removing particles in micro and sub-micro size ranges, aerosol filtration by fibrous filters has found such diverse applications as in the protection of humans and delicate devices from exposure to hazardous fine particles. It has therefore been the object of intense research, both theoretical and experimental.

6.2 Mechanisms of Aerosol Particle Deposition on Fibrous Filters

Deposition of aerosol particles on fibrous filters during aerosol filtration is caused by mechanical capture and/or electrical attraction. Mechanisms of the former comprise direct interception, inertial impaction, diffusion deposition, and gravitational settling [306].

For a simplified analyzing approach, single fiber efficiency, E_s, is defined as the efficiency with which an individual fiber removes particles from an aerosol stream [307]. The overall efficiency of a filter is, clearly, a function of the single fiber efficiency.

Collection by *interception* occurs when a particle follows a gas stream line that happens to come within one particle radius of the surface of a fiber, as shown in Fig. 31(a). The particle hits the fiber and is captured because of its finite size. *Inertial impaction* of a particle on a fiber occurs when a particle, because of its inertia, is unable to adjust quickly enough to the abruptly changing stream lines in the vicinity of a fiber and crosses those stream lines to hit the fiber, as shown in Fig. 31(b). *Diffusion deposition* of a particle happens when the combined action of airflow and Brownian motion brings a small particle into contact with a fiber, as shown in Fig. 31(c).

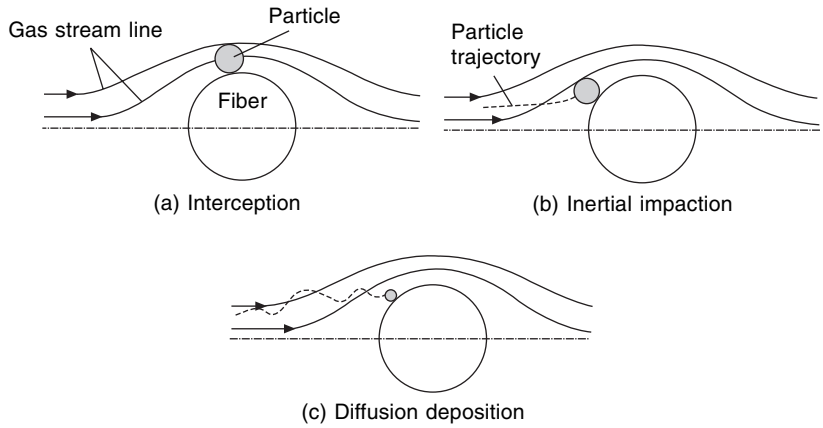

Fig. 31 Mechanical capture of aerosol particles by a single fiber

The relative contributions of diffusion and particle inertia to deposition are functions mainly of particle diameter, gas velocity, and fiber diameter. In general, particle inertia makes a greater contribution for larger particles, while Brownian motion caused by thermal agitation plays a greater role for particles smaller than 0.1μm [306]. For particles in the medium size range, both particle inertia and thermal perturbations are relatively weak. As a consequence, the collection efficiency of a fibrous filter has a minimum value, as shown in Fig. 32 [307].

Application of electrostatic forces can significantly augment the collection efficiency of a fibrous filter. This is particularly useful for improving collection of particles in the medium size range, which are difficult to capture by other mechanisms [308], as shown in Fig. 32. With the help of electrostatic force, a filter can achieve considerable collection efficiency at a lower packing density, thereby lowering resistance to gas

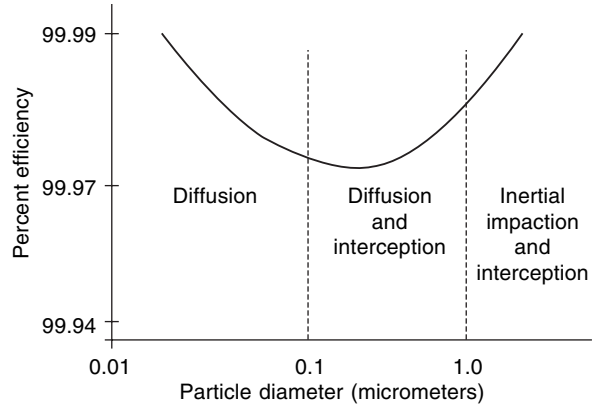

Fig. 32 Filter efficiency versus particle size

flow in the filter. However, the effects are insignificant unless the particles or fibers are highly charged.

External electrostatic forces can be applied to augment the collection efficiency of a filter either by charging the airborne particles or by creating an electric field in the filter [308]. A charged particle polarizes the fiber and, as a result, experiences an image force that is equal to the Columbic force between the charge on the particle and an equal but opposite charge placed inside the fiber at a position corresponding to the optical image of the particle. An external applied electric field polarizes the fiber as well as the particles. The polarized fiber acts as a linear dipole and creates a non-uniform field. The charge on a particle in such a non-uniform electric field encounters another force, in addition to the force exerted by the externally applied field.

A unique property of aerosol particles is that they will attach firmly to any surface (e.g. fibrous filters) they have deposited on. Also, aerosol particles adhere and form agglomerates when they contact one another.

The most important forces for particle adhesion are the van der Waals forces, and the long range forces that exist between molecules [309, 310]. Another force attaching particles to fibers is surface tension of adsorbed liquid films covering the particle [306–308, 311–314]. Accordingly, to some extent, the filter is found to be more efficient when it is operated at high humidities [315]. Electrostatic force also attaches particles to the filter.

6.3 Theories and Analytical Approaches for Aerosol Filtration Through Fibrous Filters

The ability of fibrous filters to collect particles is usually expressed in terms of filtration efficiency, E, the fraction of entering particles that are retained by the filter:

$$E = 1 - \frac{C_{\text{out}}}{C_{\text{in}}} \tag{82}$$

where C_{out} and C_{in} are the outlet and inlet aerosol particle concentration, respectively.

Research has been carried out to determine the efficiency of fibrous filters collecting

aerosol particles by various mechanisms. A classical approach is to derive it from the aerosol filtration efficiency of one single filter element (η), whose size and shape are chosen to best represent the microstructure and porosity of a given filtering material [307, 316]. The single-fiber efficiency is defined as:

$$\eta = \frac{\text{Number of particles collected on unit length}}{\text{Number of particles geometrically incident on unit length}} \tag{83}$$

The single fiber efficiency is the combined effect of the various mechanisms of capture, including direct interception, inertial impaction, diffusion deposition, and gravitational settling.

The most frequently used expression for single-fiber interception efficiency results from the Kuwabara approach [306, 307, 317–320]:

$$\eta_R = \frac{1}{2Ku}\left[2(1 + N_R)\ln(1 + N_R) - (1 + N_R) + \frac{1}{1 + N_R}\right] \tag{84}$$

where interception parameter $N_R = D_p$ (particle diameter)/D_f (fiber diameter), Ku is the Kuwabara hydrodynamic factor that includes the effect of distortion of the flow field around a fiber due to proximity to other fibers. It depends only on solidity of the fibrous filter, α, when the Reynolds number, Re < 1.0:

$$Ku = -\frac{\ln\alpha}{2} - \frac{3}{4} + \alpha - \frac{\alpha^2}{4} \tag{85}$$

Efficiency due to impaction takes into account the inertia of the particles and can be calculated as [318–320]:

$$\eta_I = \left[\frac{\gamma}{\gamma + 0.8} - \frac{2.56 - \log_{10}(Re) - 3.2N_R}{10(\gamma)^{1/2}}\right](1 + N_R) \tag{86}$$

where γ is an inertia parameter and Re the Reynolds number.

As another vital component of aerosol deposition, especially for micro particles, the diffusion behavior of aerosols is calculated with empirical equation [320]:

$$\eta_D = 2.6\left(\frac{1 - \alpha}{Ku}\right)^{1/3} Pe^{-2/3} \tag{87}$$

where Pe is the Peclet number.

In investigational work to validate or check a theoretical prediction, it would be ideal to control the filtration parameters so that only one mechanism acts at a given time. But in real situations several mechanisms usually act together. An accurate description of the filtration process under this situation is not easy due to the possible coupling effects between different mechanisms. The simplest general approach is to assume that the several processes (1, 2…and j, corresponding to direct interception, inertial impaction, diffusion deposition, and/or gravitational settling) work independently, and the total single fiber efficiency is then given as [306, 311, 318]:

$$\eta_{12\ldots j} = 1 - \prod_{i=1}^{j}(1 - \eta_i) \tag{88}$$

If the independent assumption is invalid for, say, two processes acting together, an interaction term η'_{12} should be added:

$$\eta_{12} = \eta_1 + \eta_2 + \eta'_{12}(\mathrm{N}_1, N_2) \tag{89}$$

where N_1 and N_2 are the dimensionless parameters appropriate to the two processes. Studies have been performed to derive the interaction terms between different filtering processes, such as that between diffusion and interception [319], or that between gravity and interception [306].

Clearly, the overall efficiency of a filter, E, is a function of the single-fiber efficiency, η. As η is defined as efficiency on a unit length of a fiber, E can be calculated by summing up the contributions of all the efficient lengths in a filter to yield [321, 322]:

$$E = 1 - \exp\left(\frac{L}{l}\right) \tag{90}$$

where L is the total fiber length in a filter and l the efficient filtration length.

An assumption that all fibers in a filter are the same size and possess the same filtration efficiency will therefore provide [307]:

$$E = 1 - \exp\left[\frac{-4\eta\alpha L}{\pi D_f (1 - \alpha)}\right] \tag{91}$$

where α is the solidity, and L the thickness of the fibrous filter, and D_f is the diameter of the fiber.

However, the arrangement formats of fibers in a filter will always impact on the aerosol filtration since fibers interact during the filtration process. To account for the effect of fiber arrangement, two multifiber models have been used to investigate the interception efficiency of fibrous filters composed of symmetrical arrays of fibers, including parallel arrays and staggered arrays, as shown in Fig. 33 [317, 323]. The fibers in these models are assumed to have identical cross-sectional shapes and sizes, and to be separated from each other by the same horizontal and vertical distances. If the length-to-radius aspect ratio of a fiber is very large, the contributions at the ends of the fibers are negligible. Hence the problem can be simplified as a two-dimensional periodic flow system.

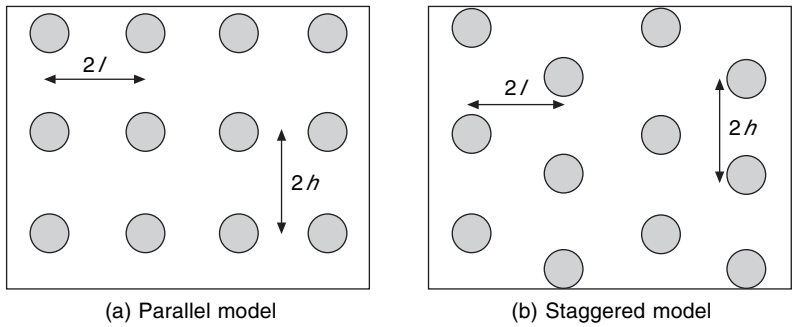

(a) Parallel model (b) Staggered model

Fig. 33 Multifiber model filters

Still, for the multifiber models, calculations have to start from a single-fiber model. And the single fiber efficiency due to interception (Equation 84) is modified to be a function of the fiber separation ratio, *l*/*h*, which is the ratio of horizontal to vertical distance between neighboring fibers. λ, a function of *l*/*h* only, is introduced to account for the effect of fiber separation ratio so that [317]:

$$\eta_R = \frac{\lambda}{2Ku}\left[\begin{array}{l} 2(1+N_R)\ln(1+N_R) - (1+N_R) \\ \quad + \dfrac{1}{1+N_R} + \alpha\left(-2N_R^2 - \dfrac{1}{2}N_R^4 + \dfrac{1}{2}N_R^5 + \ldots\right) \end{array}\right] \tag{92}$$

There are other modifications or approximation versions of Equation (84), trying to account for the nonhomogeneous fiber distribution [318, 319, 324]. However, the most difficult in studying aerosol filtration processes is the description of the heterogeneous fibrous structures. Shapiro [321, 322] introduced an inclusion model, where the filter material is assumed to be a uniform matrix containing a certain volumetric fraction *k* of inclusion of size *a*, as shown in Fig. 34. Both inside and outside the inclusion, the filter structure is assumed to be homogeneous, albeit with different porosities, ε_1 and ε_2, respectively.

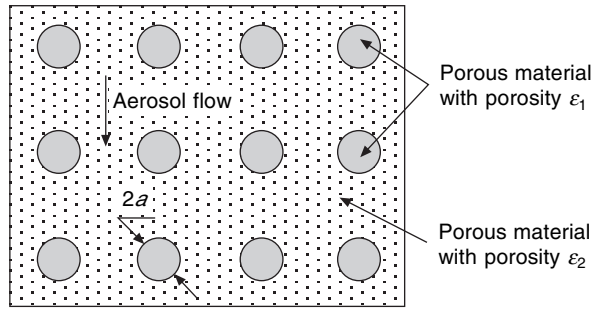

Fig. 34 Schematic of inclusion model

Alternative approaches [318, 324] involve a model where the filter media is represented by a 2-dimensional distribution of cells of varying packing density, as shown in Fig. 35. An assumed packing density distribution function, i.e. log-normal function, or Γ' distribution, is usually used. There are also other ways to subdivide

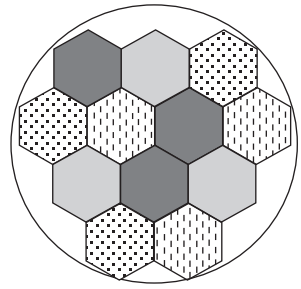

Fig. 35 Filter media represented by a 2D distribution of cells of varying packing density

the model filter into a series of elements with different structural characteristics, defined by local directionally dependent permeability [319, 325].

When the filter structure is defined, the flow field during filtration can be characterized by such constitutive equations as the continuity equation (Equation 93) and Darcy's law (Equation 94):

$$-\nabla \cdot \rho u = \frac{\partial(\rho\varepsilon)}{\partial t} + Q \tag{93}$$

where ρ is the fluid density, u the velocity field, Q the source term.

$$u = -\frac{K}{\mu}\nabla P \tag{94}$$

where K, μ and P are the permeability, fluid viscosity and the pressure, respectively. The permeability of a fibrous filter is usually expressed as a function of porosity, and may be subject to change during the filtration process with the increasing deposition of aerosol particles onto the filter.

The constitutive equations and corresponding boundary conditions can be solved analytically or numerically to give the pressure field and velocity field. These relations, combined with expressions for single-fiber efficiency as shown in Equations (84–89), allow calculation of the efficiency of each element of the filter (local efficiency), as well as their combination or averaging into the overall efficiency of filter materials [318, 326].

In addition to work on the frequently discussed processes involving aerosol filtration, there are studies on such issues as van der Waals forces between particles and fibrous filters [309, 310, 327]. As to electrostatic forces in fibrous filters [314, 328], Wang [308] presented a review discussing the expressions for various electrostatic forces acting on a particle in the vicinity of a fiber.

In the case of non-spherical aerosols, or polydisperse aerosols, the filtration problem can be even more complicated. Asgharian *et al*. [329] investigated the filtration of fibrous aerosols by fibrous filters, where only impaction and interception are considered [330]. The governing equations of motions for translation and rotation of fibrous particles are derived for airflow over a cylindrical object. For agglomerated particles, an equivalent particle diameter is used [331]. And several attempts have been made to address polydisperse aerosols by introducing particle distribution functions [332, 333].

Furthermore, changes in flow field, pressure drop and filter structure caused by particles clogging have be considered [334–339]. The influence of fluctuations on the efficiency of aerosol particle collection with fibrous filters is also investigated [340].

However, all of these models (multifiber, inclusion, cell or other element models) are still far from being as precise as required for describing the heterogeneous structure of a fibrous filter and the stochastic nature of aerosol behavior. Other approaches have therefore been attempted to deal with the problem.

Przekop *et. al*. [341] proposed an approach where the fluid dynamics is described by the lattice Boltzmann (LB) model, while the solid particle motion is modeled by the Cellular Automata (CA) probabilistic model. It is reported that the CA models

keep track of the many-body correlations and provide a description of the fluctuations, while the LB models are believed to be numerically more efficient and offer much more flexibility to adjust the fluid parameters [342, 343].

In other works the stochastic approach based on the Monte Carlo method is applied so as to simulate aerosol filtration through fibrous filters. This approach addresses the stochastic nature of aerosol particle transportation through fibrous filters (random pore sizes, particle sizes [327] and initial positions [344]), and can account for the adhesion forces between different bodies, i.e. particle–particle and particle–fiber.

Theoretically speaking, even today there is only limited understanding about the behavior of aerosol filtration through fibrous filters, due to lack of efficient and precise ways of representing the intricate and heterogeneous filter structure, as well as the combined/coupling effects among different mechanisms of filtration.

6.4 Experimental and Characterization Techniques

Various experimental and characterization techniques have been employed to test the filtration efficiency and/or the transport/deposition behavior of aerosols in fibrous filters. A typical system of an aerosol filtration test is shown in Fig. 36 [306, 316, 345, 346]. Firstly, an aerosol generator is used to produce aerosol particles of desired sizes and distribution. The most popular approach is to produce aerosols from liquid droplets. For monodisperse aerosols, the process starts with the production of liquid droplets of constant size so that, if the liquid is a solution of the material required for the aerosol, the droplet is made to evaporate, leaving the monodisperse aerosol as a solid residue. Size of the particles can be adjusted by altering concentration of the solution [306, 316, 347]. The generated aerosols can then pass through a neutralizer to avoid unwanted electrostatic effects. Then, in the filtration set, the aerosol concentration in both upstream and downstream of the filter is recorded. Two options for collecting these data are shown in Fig. 36. Finally there is an aerosol detector to record the particle numbers/concentration that is passing by. In an electrical aerosol detector, the aerosol is detected first by exposing the particles to unipolar ions in a diffusion charger and then measuring the charge on the particles with an electrometer current sensor [316, 348]. Alternatively, the particle concentration can be measured by optical means, where a laser beam is usually used as the illumination source [349]. The optical approach can also be used to detect the local efficiency in the filter [347].

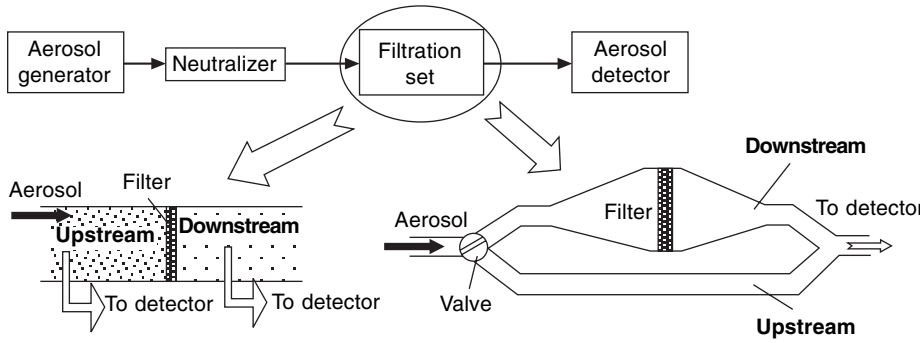

Fig. 36 A typical system for the aerosol filtration test

With this approach, a particle is counted when it passes through the focusing spot of the laser beam. Then it will scatter the light, which is converted to electronic pulses by collection optics.

In addition to the optical detecting approach, deposition distribution of particles on a fibrous filter can be characterized by scanning electron micrograph (SEM) [337, 350], photometer [351], and X-ray computerized tomography (XCT) [318].

6.5 Summary

Deposition of aerosol particles on fibrous filters during aerosol filtration can be caused by mechanical capture and/or electrical attraction. The mechanical capture mechanisms consist of direct interception, inertial impaction, diffusion deposition, and gravitational settling. However, this separation of mechanisms is artificial, as several or all might act simultaneously in practice. This makes it difficult to characterize the aerosol filtration behavior, a result of the combination or coupling of various mechanisms.

To describe the intricate and heterogeneous fibrous structure is another challenge. Traditional approaches to deriving total efficiency of a filter from a representative single-fiber efficiency are limited to empirical expressions. Although there has been work on various numerical and/or stochastic models, available models for describing the heterogeneity of filter structures are far from being realistic.

Various experimental characterization techniques are available to measure filtration efficiency and/or the transport/deposition behavior of aerosols in fibrous filters. A typical system usually includes an aerosol generator, a filtration set and a particle detector.

7. MICRO/NANO-SCALE TRANSPORT PHENOMENA IN FIBROUS STRUCTURES: BIOMEDICAL APPLICATIONS

7.1 Introduction

Transport phenomena occur frequently in biomedical applications, especially on a micro and nano scale. For example, bioartificial kidneys, liver and lung devices usually rely on hollow fiber membranes for transport, filtration and dialysis. Other transport processes through biomembranes are found in drug delivery, blood filtration and separation, extraction/separation of microorganisms, etc. Some of these applications will be discussed in the following sections.

7.2 Mechanisms of Hollow Fiber Membranes

The regular life of human beings depends on the effective functions of all over organs. Some of the organs are involved in complicated processes of metabolism and transfer/exchange of mass/nutrients with other parts of the body. An acute failure of any of these organs will lead to a series of disturbances to the whole system and is likely to be fatal. Accordingly, extracorporeal devices and/or systems have been developed to temporarily assist patients in carrying out usually the most critical functions (mass and nutrient transfer) of these failing organs. Most of these devices are still in their infancy. However, devices based on hollow-fiber bioreactors have been reported to give encouraging results [352–354]. These contain numerous small fibers made from semi-permeable membranes, assembled within a cylindrical shell/

 doi:10.1533/tepr.2006.0002

jacket. The intratubular space of a fiber is called the lumen or capillary space, and the space outside of a fiber is called the extracapillary space. One of the clinical applications of hollow fiber bioreactors is the hemodialyzer, as shown in Fig. 37. The membranes used in clinical dialyzers are made of cellulose or synthetic polymers, and consist of bundles of about 10 000 hollow fibers, each with an internal diameter of around 200μm [355]. Blood is allowed to flow, a few ounces at a time, through the lumen of the hollow fibers. The concentration of the various electrolytes in the blood must be maintained within narrow limits if serious harm to the patient is to be avoided. Therefore, the extracapillary space of the dialyzer is filled with a solution of certain minerals, and its concentration of sodium, potassium, chloride, and other electrolytes is made to approximate to the levels in normal human blood serum. Thus, through the process of dialysis, concentrations of these ions will become nearly equal on both sides of the membrane, and undesirable waste products in the blood are dialyzed out with a constant supply of fresh solution to keep the bath waste level low. The dialyzer is what is known as an *artificial kidney*. The artificial kidney is given the function of ultrafiltration, the removal of excess water from the patient by the pressure differences between the lumen and extracapillary space. If the patient has been suffering from more than the recommended amount of fluid since the previous dialysis, negative pressure (suction) can be applied to the dialysate. In the way described above, blood is taken from the patient's artery through a system of tubes to the artificial kidney for dialysis and ultrafiltration. Eventually, the blood is returned by a tube to the patient's vein [356].

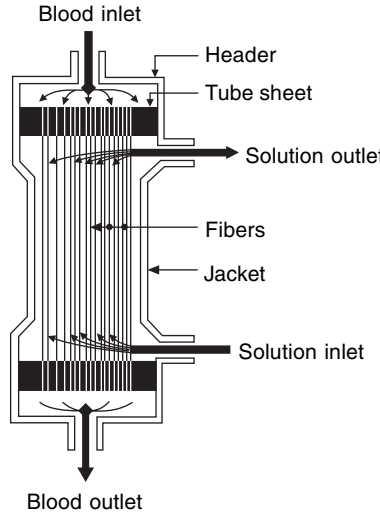

Fig. 37 A typical hollow fiber dialyzer

Recently, tissue engineering researchers have been trying to develop the so-called bioartificial kidneys or bioengineered artificial kidneys. They are supposed to be able to perform, in addition to dialysis and ultrafiltration, such complicated tasks as the metabolic, endocrine and immune roles. These effects may transcend the filtration functions for the survival of patients with renal failure either in the acute or chronic

form [357]. These bioartificial kidneys are similar to the conventional hemodialyzer, except that viable cells are introduced into the extracapillary spaces and are attached to the outer surface of hollow fibers. Alternatively, these cells can be entrapped in gels or immobilized on polymeric microcarriers to avoid blocking the pores and stopping the mass exchange across the membrane. Sources of these viable cells include human kidneys unsuitable for cadaver transplant, and porcine kidney cells. After harvesting, culturing and seeding onto the hollow fibrous bioreactors, they are able to carry out some of the metabolic functions of the kidney [357, 358].

Similarly, hollow-fiber-based bioartificial liver devices can be developed by culturing porcine hepatocytes inside the hollow fibers, while the patient's blood is circulated in the extracapillary space. Toxic components in the blood, which diffuse through the hollow fiber membrane into the luminal space, are metabolized by the entrapped hepatocytes and diffuse either back into the bloodstream or are washed out with the intraluminal stream. Alternatively, the cells can be cultured outside the hollow fiber and the blood goes through the luminal space [354, 359–361].

Another application of hollow fiber bioreactors in extracorporeal devices is artificial lungs or extracorporeal blood oxygenerators, which provide cardiopulmonary bypasses during open-heart surgery. The hollow fiber membranes are used to separate the blood and gas phase. Blood flows outside and across bundles of hollow fibers while gas (usually oxygen or oxygen/nitrogen mixtures) flows inside the fibers. The diffusion of oxygen into and out of the bloodstream is driven by the concentration gradient across the membranes [362–364]. In addition to the hollow fiber modules similar to those shown in Fig. 37, another optional structure for the artificial lung is woven microporous hollow fibers. The resulting fabrics may be wound around a central tube to form a bundle, as shown in Fig. 38 [365].

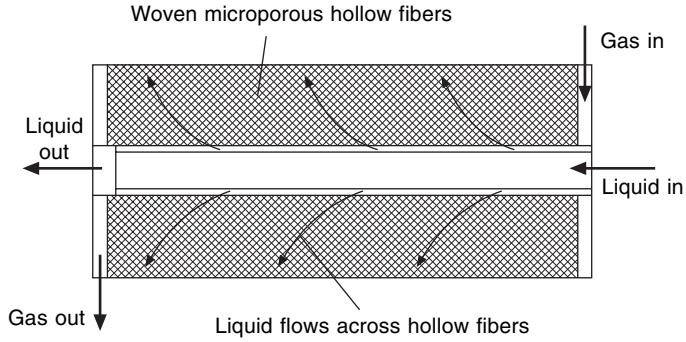

Fig. 38 Hollow fiber woven fabrics for artificial lung

Work has also been reported on hollow fiber bioreactors in developing a bioartificial pancreas for treating diabetes [366–369]. Up to now, however, research work on tissue engineered organs has been carried out mostly in laboratories.

In addition to artificial organs, hollow fibers have been used in such applications as enzyme reactors, cell bioreactors for bacterial and yeast culture [370, 371], and waste treatment [372, 373], and for mass transport and exchange between cultured cells and their environment, due to the much larger surface area of hollow fibers as compared to flat membranes.

7.3 Transport Through Biomembranes

Much work has been done on the analysis and modeling of transport and flow behavior of hollow fiber bioreactors.

Since fluid flow is predominantly in the axial direction in most hollow fiber bioreactors, the transport through hollow fiber biomembranes is usually simplified as an axial flow problem [370]. Typically, Krogh cylinder geometry is assumed [374–376]; that is, each fiber is surrounded by a uniform annulus, as shown in Fig. 39. The outer radius of the annulus is referred to as the Krogh radius, and the Krogh cylinders of adjacent fibers touch one another. The entire axial flow in hollow fiber bundles is then modeled as one lumped fiber surrounded by a uniform Krogh cylinder. This simplification ignores the interstitial space among Krogh cylinders and the likely coupling among different fibers. Transport across the fiber membrane is both diffusive and convective. The diffusive transport is driven by the concentration gradient, while the convective by the pressure gradient across the membrane. When the convective flow is negligible relative to diffusion, due to low membrane permeability or low inlet pressure, the bioreactor is said to be diffusion limited or operating under diffusion control. And the continuity equations for the fiber lumen, the fiber (the radial convection across the fiber wall is negligible), and the extracorporeal spaces can be expressed as follows:

$$2u\left(1-\frac{r^2}{R_L^2}\right)\frac{\partial C}{\partial z}=\frac{D_l}{r}\frac{\partial}{\partial r}\left(r\frac{\partial C}{\partial r}\right) \tag{95}$$

$$\frac{D_f}{r}\frac{\partial}{\partial r}\left(r\frac{\partial C}{\partial r}\right)=0 \tag{96}$$

$$\frac{D_e}{r}\frac{\partial}{\partial r}\left(r\frac{\partial C}{\partial r}\right)=M \tag{97}$$

where u is the dimensionless velocity, R_{L} the fiber lumen radius, C the concentration, M the assumed maximum rate of consumption, D_l, D_f and D_e are effective diffusion coefficients in lumen, fiber and extracapillary spaces, respectively [377, 378]. The diffusion limit assumption is, however, realistic only for earlier generation hollow

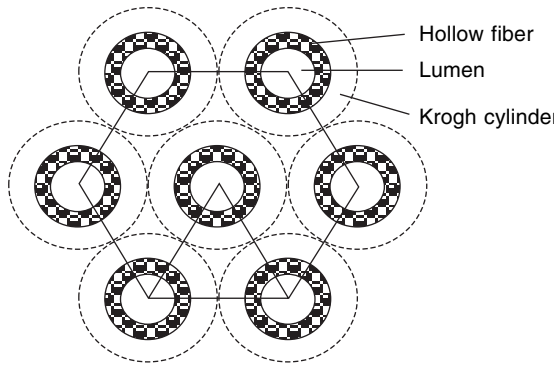

Fig. 39 Krogh cylinder geometry of the hollow fiber bundles

fiber bioreactors constructed of membranes with permeability to relatively small molecules.

The development of hollow fiber cell culture has gradually shifted away from diffusion limited to convection enhanced bioreactors to improve their performance in transporting key nutrients and/or waste, which is critical for their application in bioartificial organs. Assuming that flow is laminar and that entrance effects can be ignored, the continuity and momentum equations (Navier–Stokes equations) for steady-state convective flow in the fiber lumen and extracapillary space are given in dimensionless form as [379]:

$$\frac{\partial U}{\partial Z} + \frac{1}{R}\frac{\partial (RV)}{\partial R} = 0 \tag{98}$$

$$\frac{1}{R}\frac{\partial}{\partial R}\left(R\frac{\partial U}{\partial R}\right) = \frac{\mathrm{d}P}{\mathrm{d}Z} \tag{99}$$

where

$$U = \frac{u}{u_0},\quad V = \frac{vL}{u_0 R_L},\quad P = \frac{pR_L^2}{\mu u_0 L},\quad Z = \frac{z}{L},\quad R = \frac{r}{R_L}$$

where u and v are axial and radial velocities, respectively, μ is the fluid viscosity, p the hydrostatic pressure, u_0 the inlet centerline velocity, and L the fiber length.
The radial velocity through the hollow fiber wall, V_w, is also given by Darcy's law [370, 375, 379]:

$$V_W = \kappa(P_L - P_E) \tag{100}$$

where κ is a dimensionless permeability, P_L and P_E are pressures at lumen and extracorporeal spaces (assumed constant axial lumen and extracapillary pressures), respectively. Boundary conditions for Equations (98), (99) and (100) include symmetry at the lumen centerline, no slippage at both fiber inner and outer wall, matching velocity at both inner and outer fiber wall, etc. As a result, analytical solutions can be obtained for the expressions of lumen and extracorporeal space pressures, and axial and radial velocity profiles [379].

When a radial convective flux is superimposed on diffusion as more permeable membranes are used, the mass transport process is usually represented by a dimensionless coupled convection–diffusion equation [380]:

$$\frac{\partial C}{\partial \tau} + U\frac{\partial C}{\partial Z} + \left(V - \frac{1}{Pe_R R}\right)\frac{\partial C}{\partial R} = \frac{1}{P_e}\frac{\partial^2 C}{\partial R^2} \tag{101}$$

where Pe_R is the Peclet number in the radial direction, $Pe_R = v_w R_L/D$, $\tau = v_w t/R_L$, D is the solute diffusion coefficient, and v_w is the radial velocity at lumen wall.

More complex forms of the above equations are available in various reported models by removing restricted assumptions such as those accounting for the gravitational effect [381], axial variation in lumen and extracapillary pressures [380], non-Newtonian fluid (blood) with a viscosity varying in radial and axial directions [382, 383], cross-flow through hollow fiber bundles (most likely in the case of artificial lung) [365, 384], etc. Accordingly, solutions for these models are usually obtained through the

various numerical methods, such as finite difference methods [376, 385–387], finite element methods [363, 383, 384, 388], and finite volume methods [382, 389].

The actual arrangement of fibers in a typical cartridge is somewhat random [354], and fiber wall thickness is very likely to be polydisperse [390]. Therefore, most of the models for mass transfer and flow in hollow fiber bioreactors provide only a description of flow through some average fiber which is representative of the overall system geometry.

Microscopic simulation methods have also been reported on the study of transport through biological membranes. Molecular dynamics [391, 392] and atomistic molecular dynamics [393] have been used for simulation of transport through biological membrane channels. These simulations, although still subject to the limitations of classical mechanics, consist of integration of equations of motion for a many-body system of interacting particles, and can provide direct information on the structure and dynamics of complex biological systems and a detailed picture of molecular/atomic motions. In addition, stochastic approaches such as the Monte Carlo [394–397] and Cellular Automata [398] methods can reflect random and stochastic effects involved in the diffusion, particle accumulation and bio-reaction processes. Despite large computational cost, these microscopic simulation methods are regarded as highly promising in their application in dealing with the complex, multi-component transport behavior in bioengineered membranes.

7.4 Experimental and Characterization Techniques

Again, various methods have been reported to characterize structures of hollow fiber membranes and mass transfer through membranes in biomedical applications.

7.4.1 Measurement of Diffusion/Hydraulic Permeability of Hollow Fiber Membranes

In contrast to flat membranes, hollow fiber membranes present considerable technical difficulties when their diffusive permeability is to be measured. Specially designed model dialyzers are constructed for this purpose. Each model dialyzer consists of only about one hundredth or even fewer of the fibers for a real one. Advantages of the down-scaled fiber model over a real dialyzer are: (i) All the hollow fibers can be ensured to be non-blocked and non-broken; (ii) interaction among the fibers can be negligible and, (iii) the flow field around the fibers is more visualizable. The transport properties of the hollow fiber membrane can therefore be characterized quantitatively with higher accuracy [399].

Measurement of the hollow fiber diffusion permeability to small molecules is implemented by means of a simple test setting, where a bundle of hollow fibers is installed in a large bath containing circulating saline solution (dialysate), as shown in Fig. 40. Next, the diffusive permeability of the membrane can be derived from concentrations of the test fluid at the dialyzer inlet and outlet [400]. Since it is not always possible to avoid filtration that occurs as a result of pressure during the supply of test fluid, this test may not be suitable for membranes with high hydraulic permeability (due to pressure gradient). Nor is this low-precision method appropriate for solutes of high molecular weight, as concentration differences between the dialyzer inlet and outlet are small [401].

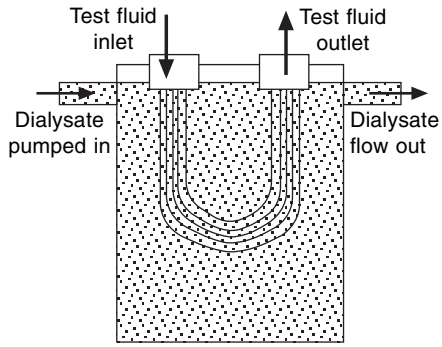

Fig. 40 Hollow fiber diffusive permeability measurement

Higher-precision methods involve usage of an isotope-labeled solute as test fluid. The test hollow fiber is dialyzed for a given period of time, and the amount of residual solute is measured using a scintillation counter [402]. However, radioactive substances require special handling, and quantities must be restricted to prevent overexposure. Their application is therefore limited [403].

Another technique uses optical fibers positioned at either end of a hollow fiber under test to allow continuous measurement of solute concentration in the fiber lumen. In such a test, a laser light beam is emitted from one of these optic fibers into the test solution, and is then caught by the other optic fiber and detected with a silicon photodiode. The time-dependent decay in transmitted light intensity caused by the diffusion of solutes into the lumen is recorded for analysis to give the solute concentration, and further the permeability. This method is independent of convective mass transport and osmotic flow through membranes. Hence its superiority to ordinary techniques with respect to accuracy [403, 404].

Hydraulic permeability, or the filtration coefficient, may be found from a filtration test when $\Delta\pi = 0$, using the relationship:

$$J_V = k(\Delta P - \sigma\Delta\pi) \tag{102}$$

where k is the hydraulic permeability or filtration coefficient, σ is the Staverman reflection coefficient, ΔP is the difference in solution pressure across the membrane, and $\Delta\pi$ is the difference in the osmotic pressure of the solution across the membrane [401].

7.4.2 Pore Size and Pore Size Distribution Measurement

Characterization of pore size and pore size distribution for hollow fiber membranes can be achieved by using direct or indirect methods. The direct physical methods are described as microscopic, bubble point, mercury porosimetry, etc. The last two have been discussed in Section 5. The indirect ones are based on permeation and rejection ratio of membranes to reference molecules and particles [405, 406], including water permeation, gas permeation, and solute transport.

Microscopy observation and image processing of micrographs directly give visual information on membrane morphology such as surface pore shape and size, their distribution, and so on, but cannot efficiently provide information on pore length or

tortuosity. Available microscopy methods include transmission electron microscopy (TEM), scanning electron microscopy (SEM), the field emission scanning electron method (FESEM), and atomic force microscopy (AFM). For both TEM and SEM, an electron beam of high energy is required, often leading to damage of the sample and therefore causing problems to the task of observation. In contrast, FESEM can be performed at low beam energy, while AFM involves no electron beam energy at all. Another problem of the microscopic observation of TEM and SEM is the difficulty in preparing samples. First, sample drying should not lead to collapse of the original structure; next, the dried membrane has to be embedded and sliced, both being intricate processes likely to cause deformation and impairment to the sample. AFM can image non-conducting surfaces in air and even in liquids. It is therefore suggested that, to prevent damage to the sample, it need not be dried and exposed to the vacuum when prepared [406]. Accordingly, AFM is becoming the most popular technique in microscopy observation of pore structures of membranes [407–410]. However, microscopy methods, including AFM, lead only to information on the porous surface structure, and are not able to differentiate between open pores and dead-end pores. It is therefore believed that different testing methods should be combined to give a more comprehensive description of the porous structure of hollow fiber membranes [408].

Indirect testing methods are usually correlated with such permeation parameters as liquid flux, gas flux, and solute flux, and are able to determine the pore size open to flux. The results, therefore, are the lowest boundary of the pore constriction present along the whole path. Also, these methods can be used to characterize bulk pore size of the membrane.

The water permeability method is relatively simple when applied to the indirect evaluation of pore size, where the mean pore radius, r, can be calculated by [411, 412]:

$$r = (8u\Delta xk\tau/A_s) \tag{103}$$

where u is the viscosity of water, Δx the membrane thickness, τ the tortuosity defined by pore length/membrane thickness, A_s the membrane surface porosity, while $k = J/P$, J represents water flux, and P the trans-membrane pressure. For the constant pressure liquid displacement method, CPLM, this pressure is kept at a standard low value to avoid erroneous results (permeability may vary with applied pressure, for example) [413].

Measurement of the flow rate of a gas (usually pure nitrogen) through a porous membrane can also provide a way to determine a mean pore radius of the membrane [406, 408]. The permeation flux through the membrane is measured at different transmembrane pressures. From the lineal plot of the permeability as a function of the mean pressure with intercept B_0 and slope K_0, the mean pore size can be calculated as:

$$r = \frac{16}{3}\left(\frac{B_0}{K_0}\right)\left(\frac{2RT}{\pi M}\right)^{1/2}\mu \tag{104}$$

where R is the gas constant, T the absolute temperature, M the molecular weight of the gas, and μ the gas viscosity.

The solute permeation method is based on both filtration flux, J, and rejection rate, f, during the test. The rejection rate of a membrane to a solute of concentration C_m is defined as

$$f = 1 - \frac{C_f}{C_m} \tag{105}$$

where C_f is the solute concentration after filtration. This parameter represents the membrane selectivity to solute molecules. Several theories have been developed for the modeling of transport of solute molecules through membranes, and different expressions derived to give the relationship between pore size/structure and transport behaviors [401, 406, 407].

However, the indirect methods for measuring porous structure of membranes provide only the mean values. A well accepted theory/model for describing the relationship between transport behavior and pore structure is thus still awaited. For this reason, various characterization approaches are usually combined to give complementary information on the structure of a membrane [405, 408].

7.5 Summary

Development of extracorporeal organs is an encouraging result of the study of micro/nano transport phenomena through membranes. Artificial kidneys using hollow fiber membranes, for example, have been in clinical use to perform the task of hemodialysis for renal failure patients. In addition to success stories reported about work on dialysis and ultrafiltration, under development are such bioengineered artificial organs as bioartificial kidney, liver, lung and pancreas, which are deemed to be able to perform more complicated tasks, including playing the metabolic, endocrine and immune roles. Extensive use of hollow fiber membranes is due to their having much larger surface areas as compared to flat membranes for mass transport and exchange between cultured cells and their environment.

Since fluid flow is predominantly in the axial direction in most hollow fiber bioreactors, the transport through hollow fiber biomembranes is usually simplified into an axial flow problem, thus with an assumed Krogh cylinder geometry. Various theories have been developed on both diffusive and convective transport across the membranes. Still, the actual arrangement of fibers in a typical hollow fiber dialyzer is found to be somewhat random, and fiber wall thickness is polydisperse. Therefore, most of the models for mass transfer and flow in hollow fiber bioreactors provide only descriptions of flow through some ‘average fiber’ representative of the overall system geometry. Several microscopic simulation methods, including the Molecular Dynamics, the Monte Carlo method, and the Cellular Automata method, have been employed in the study of transport through biological membranes. Despite the large computational cost, these methods are highly promising in their application to the complex, multi-component transport behavior in bioengineered membranes.

Various techniques, both experimental and analytical, have been reported to characterize the structure (pore size and pore size distribution) of hollow fiber membranes and mass transfer through membranes in biomedical applications. Most of these are complementary rather than competitive. The various characterization approaches are thus often combined to give more comprehensive information on the structure of a membrane.

8. SCALE EFFECTS AND STATISTICAL MECHANICS MODELS

8.1 Material Scale Effect

The behavior of a material is dependent on, among other intrinsic properties, its own size or dimension. Peirce's weakest link theory of 1926 [414] reveals an early example, and nano-scale material science is now the most definite manifestation on the issue.

In dealing with fluid transport phenomena in fibrous materials, some simple calculations demonstrate the extreme importance of this scale effect. All the transport processes are conducted through material interfaces which are directly related to their surface areas. Let us take a single fiber of length l_f and radius r_f. The ratio of the fiber surface area S and volume V (the specific surface area) is

$$\frac{S}{V} = \frac{2\pi r_f l_f + 2\pi r_f^2}{\pi r_f^2 l_f} = 2\left(\frac{1}{r_f} + \frac{1}{l_f}\right) \tag{106}$$

That is, the fiber surface area relative to its volume increases as the fiber becomes thinner, which thus will significantly influence its transport behavior.

It should be noted that, for a fibrous material of given total volume V_t and volume fraction V_f and supposing there are totally N fibers of identical size, the total surface area of all fibers is $S_t = 2\,N\,\pi r_f l_f + 2N\pi r_f^2$ and the ratio

$$\frac{S_t}{V_t} = \frac{2N\pi r_f l_f + 2N\pi r_f^2}{V_t} = 2V_f\left(\frac{1}{r_f} + \frac{1}{l_f}\right) \tag{107}$$

where the fiber volume fraction is, by definition, $V_f = \dfrac{N\pi r_f^2 l_f}{V_t}$. So we can conclude that for a fibrous assembly of given volume of V_t with a known fiber volume fraction V_f, finer fibers will yield greater specific surface area. However, since $V_f \leq 1$, the specific surface area of a single fiber is always greater than that of a fibrous assembly, or the latter is the upper limit of the former.

8.2 Wetting Behavior of a Single Fiber and a Fiber Bundle

We will restrict our following discussion to the case of non-volatile liquids. According to Brochard [415] we define the complete wetting of a single fiber of radius b as the state when the fiber is covered by a liquid in two forms; the first is the drop-like geometry similar to that shown in Fig. 41(a) and the second is the manchon shape in Fig. 41(b). The latter is less energy demanding and easier to analyze geometrically, and is hence chosen here for study. Let us denote γ_{SV}, γ_{SL} and γ_{LV} the surface tensions of the solid fiber, the solid/liquid interface, and the liquid (or liquid/air). The liquid

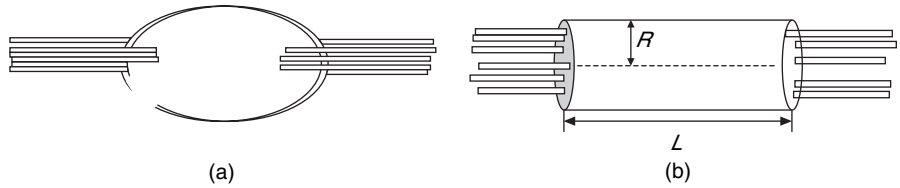

Fig. 41 Two possible liquid covering geometries

film thickness in the manchon is represented by a parameter e. This liquid manchon formation occurs when the so-called Harkinson spreading parameter S [415], defined as

$$S = \gamma_{SO} - \gamma_{SL} - \gamma_{LV} \tag{108}$$

reaches the critical value S_{CF} derived in [415].

$$S_{CF} = \frac{e\gamma_{LV}}{b} \tag{109}$$

That is, the fiber will be covered by a liquid manchon in the case of the following inequality

$$S > S_{CF} = \frac{e\gamma_{LV}}{b} \tag{110}$$

Compared to the wetting of planes, the wetting of individual fibers is a more energy-consuming process according to Young's Equation [416], as for complete wetting of a flat solid it only requires

$$S > 0 \tag{111}$$

In other words, for a plane, the critical spreading parameter S_{CP} holds

$$S_{CP} = 0 \tag{112}$$

From Equations (110) and (111) we see that it is obvious that liquids will wet a solid plane more promptly than wet a fiber.

Next, let us examine the case of a fiber bundle formed by n parallel fibers as seen in Fig. 41, each with a radius b. Two different types of liquid body geometry caused by the liquid/fiber bundle interactions are possible, just like in the individual fiber cases mentioned above; the drop-like geometry shown in Fig. 41(a) and the manchon shape in Fig. 41(b). Let us focus on the second, less energy demanding, case and assume the manchon is a cylindrically symmetric liquid body with an equivalent radius R. The criterion of complete wetting of a vertical fiber bundle dipped partially in a liquid will be derived here by comparison of the surface energy W_m of such a manchon liquid geometry with the surface energy W_b of a dry fiber bundle. For a length L of the dry fiber bundle,

$$W_b = 2\pi bnL\gamma_{SV} \tag{113}$$

whereas the same length of liquid manchon on the fiber bundle has the surface energy

$$W_m = 2\pi bnL\gamma_{SV} + 2\pi RL\gamma_{LV} \tag{114}$$

That is, the energy W_m is composed of both terms of solid/liquid interface and liquid/air interface. The complete wetting sets in when the wet state of the system is energetically more favorable compared with the dry one, i.e. $W_b > W_m$. Or from previous equations

$$\gamma_{SV} - \gamma_{SL} - \frac{R \cdot \gamma_{LV}}{n \cdot b} > 0 \tag{115}$$

Inserting Harkinson spreading coefficient from Equation (108) into Equation (116) yields

$$S > \frac{R - n \cdot b}{n \cdot b} \gamma_{LV} \tag{117}$$

So the critical value S_{Cb} for the complete wetting of the bundle system is

$$S_{Cb} = \frac{R - n \cdot b}{n \cdot b} \gamma_{LV} \tag{118}$$

The radius of the manchon R could be smaller than the total sum of fibers radii nb. Figure 42(c) shows such an example when the cross-section of the seven-fiber bundle is covered by a liquid cylinder. The value of S_{Cb} is clearly only – $4/7\gamma_{LV}$.

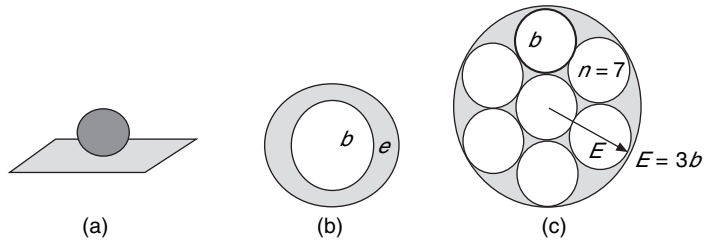

Fig. 42 Wetting of a plane (a), a fiber (b) and a fiber bundle (c)

The above results show the sequence (or ease of wetting) for the same material; a liquid will wet a fiber bundle first, then a sold plane, and finally a single fiber. This, of course, is attributable to the familiar capillary mechanism. However, the above simple analysis also explains the excellent wetting properties of a fiber mass in terms of energy changes; the consequence of the collective behavior of fibers in the bundle allows the manchon energy W_m to increase more rapidly with the fiber number n in the bundle than the dry bundle energy W_b. More importantly, this example shows that hydrophobic fibers can turn into a more hydrophilic material by forming fiber bundles (yarns or fabrics) – one solid explanation for the excellent wetting performance of fibrous materials. Finally, this example also demonstrates the significance of fiber assemblage; when you increase the number of fibers n, the wetting performance improves – another case of scale or size effects.

8.3 Hydrophobicity of Lotus Leaves

The lotus flower is a symbol of purity in many cultures. Even emerging from muddy waters its leaves remain clean and even dry, as shown in Fig. 43. This phenomenon of self-cleaning was studied in the mid-1970s and is connected with a microstructured surface as well as with a coating of a waxy substance. In fact, this unique feature has been found in many other plant leaves (e.g. cabbage, reeds, Indian cress, tulips) and in insect wings (e.g. wings of butterflies and dragonflies) as seen in Fig. 44. This fascinating subject, now termed the 'Lotus-effect' [417], has been researched ever since and increasingly applied in many areas [417–428].

As stated in previous chapters, the wettability of a material depends on the ratio of the surface tensions between water/air, material/water and material/air. The ratio of

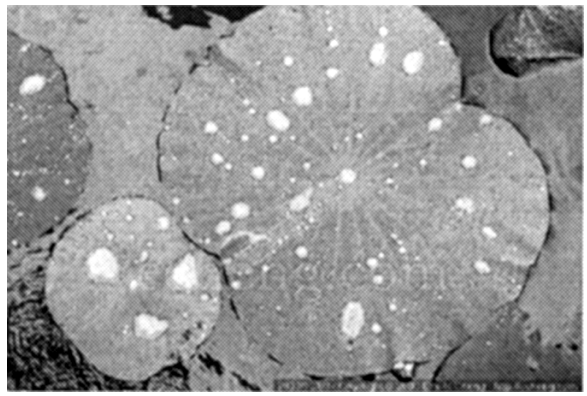

Fig. 43 Self-cleaning lotus leaves

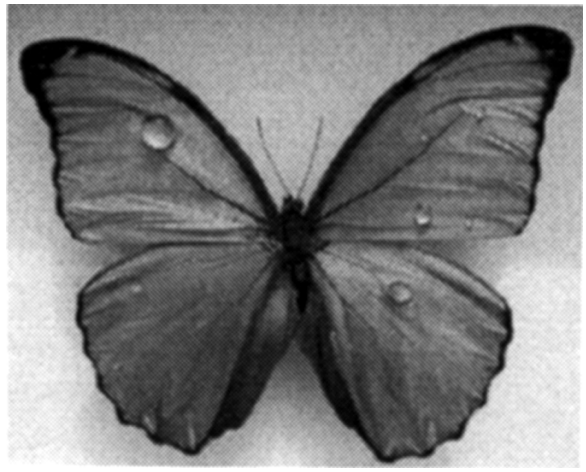

Fig. 44 Water beads atop the wings of the *Morpho sulkowskyi* butterfly [457]

the tensions determines the contact angle of a water droplet to the surface. A contact angle of 0° indicates complete wetting, the water droplet spreading out into a mononuclear film. A contact angle of 180° means complete unwettability, the droplet making contact with the surface in only one point. Materials with a high interfacial tension are more wettable than those with a low interfacial tension. However, at the micro-level, the behaviour of water on a surface is, to a large extent, dependent on the microstructure of the surface. Creating a rough area with an ultra-fine, dense fibril surface will lead to a super-hydrophobic (i.e. extremely unwettable) surface, like the lotus leaves, even in the absence of a waxy coating [418, 419, 422]. In this case air is enclosed between the water droplet and the micro-fibrous surface to minimize the contact area between the leaf and droplet so that the droplet rolls off quickly, as shown in Fig. 45.

This lotus-effect can serve once again as evidence of the scale effect; when one reduces the diameter of the fibers and increases their density (number of fibers per unit area) to a certain degree, a highly wettable surface such as that of a terry towel is turned into an extremely hydrophobic one.

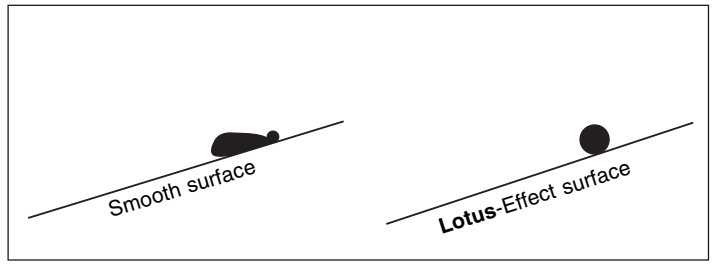

Fig. 45 Illustration of the lotus effect [423]

8.4 Statistical Mechanics Approaches

To capture more detailed fluid transport processes in complex media with intricate geometrical and topological internal structures, we have to resort to other theoretical tools than the differential equation and boundary techniques.

The phenomena of fluid transport through fibrous materials involve a large number of individual particles (in the order of 10^{27} molecules in a liter of water); there is little hope of finding an analytical solution for the motion of all of these particles. Moreover, it is not clear that such a solution, even if it exists, would be of any use because we cannot possibly observe the motion of each of 10^{27} particles. We can, however, observe macroscopic variables, such as particle density, momentum density, or magnetization, and measure their fluctuations and response to external fields. It is these observables that characterize and distinguish the many different thermodynamically stable phases of the matter: liquids flow, solids are rigid; some matter is transparent, other matter is colored; there are insulators, metals and semiconductors, and so on [429].

To study a system with a huge number of constituents, statistics is a powerful tool which derives the system macro-parameters based on an analysis of the collective behaviors of individual constituents of the system. That is, statistical mechanics establishes a connection between microscopic and macroscopic thermodynamic descriptions of a system.

8.5 The Ising Model and its Application in Wetting Studies

Statistical mechanics is the application of statistical probability for dealing with large populations, and it provides a framework for relating the microscopic properties of individual particles to the macroscopic or bulk properties of the materials that can be observed in practice, thus explaining the thermodynamics as a natural result of statistics and mechanics (classical and quantum). In particular, it can be used to calculate the thermodynamic properties of bulk materials from the spectroscopic data of individual molecules. The so-called Ising model is one of the major methods in statistical mechanics and was proposed by Ising in 1925 [430–432], initially as a tool for studying the ferromagnetic phase transition. It was later found that it is also a powerful model for investigation of several other physical phenomena such as liquid–gas transition [433, 434] and order–disorder transition of alloys [435]. In recent years, with more and more attention paid to the wetting process, the Ising model has been proved to be a potent technique in wetting mechanism studies. A series of papers has since been published by Binder, Landau and colleagues [433, 434, 436–448], and

other researchers [449–452] on the investigation of general wetting related problems using the Ising model.

In this section, we will first introduce the various interactions occurring in a liquid–fiber mixture and the energy components associated with these interactions. Then a criterion of energy state exchange according to Kawasaki dynamics [453] will be adopted as a way of describing the liquid–fiber wetting dynamics. Finally, the Monte Carlo stochastic approach will be employed to simulate the liquid wetting process.

Until recently, most of the efforts in examining wetting behavior of fibrous assemblies have been based on the study of macroscopic phenomenon and other empirical methods. Only lately have researchers attempted to apply a stochastic approach to the study of the wetting behavior of fibrous assemblies on a microscopic scale, in order to examine the fundamentals of the phenomenon. Lukas *et al.* [449] first applied the Ising model combined with the Monte Carlo simulation to study liquid–fiber interaction and the resulting wetting behavior of fiber networks. As the wetting behavior of fibrous assemblies can be regarded as the spaces between fibers changing from a gas dominant state to a liquid dominant state, the Ising model is therefore applicable in investigating the wetting behavior of fibrous assemblies.

8.5.1 Theoretical Approach

According to the Ising model, if there is a one-dimensional ferromagnet which has very strong uniaxial anisotropy, the energy of the system, the Hamiltonian, may be described as

$$H = -J \sum_{i=1}^{i-1} s_i s_{i+1} - M \sum_{i=1}^{i} s_i, \quad s_i = \pm 1 \tag{119}$$

where the spin s_i at lattice site i can point up ($s_i = +1$) or down ($s_i = -1$) along the 'easy axis', the exchange energy J represents the interaction between every two nearest neighbors (s_i , s_{i+1}), and M the intensity of the magnetic fields. Then the average macroscopic observable parameters of a system can be further derived from the Hamiltonian via the route of statistical mechanics.

In the field of statistical thermodynamics, the macro characteristics of a system are always a reflection of the interactions and the resulting balance among micro particles or cells which comprise the system. For a system composed of N kinds of subsystems, each with energy e_i (i = 1, 2, 3……N), while the number of subsystems having the energy e_i is m_i, the internal energy of the system is:

$$E = \sum_i m_i e_i \tag{120}$$

The internal energy can be altered by a change either of m_i or e_i

$$dE = \sum e_i dm_i + \sum m_i de_i \tag{121}$$

The first term in Equation (121) represents the energy change due to the redistribution of the subsystems among the energy e_i, which is equal to the variation of the Hamiltonian dH. The second term represents the energy change due to the change of the subsystems' energies. The alteration of energies of the subsystems can be thermal-dynamically

driven by extrinsic work, such as work of interfacial tensions or work of pressure. Considering only the work of interfacial tension E_γ for spontaneous wetting without pressure applied, Equation (120) can be written as

$$dE = dH + dE_\gamma \tag{122}$$

The interface between the system and the environment regarding the wetting ensemble includes that between fibers and gas with interfacial tension γ_{fg}, that between liquid and gas with interfacial tension γ_{lg}, and that between fiber and liquid, γ_{fl}. Assuming that wetting is a spreading process, the variation of energy per unit area during spreading should be

$$dE_\gamma = \gamma_{fl} + \gamma_{lg} - \gamma_{fg} = \gamma_{lg}(1 - \cos\theta) \tag{123}$$

From the above analyses, the statistical genesis of the process of liquid wetting fibrous assemblies can be regarded as the interactions and the resulting balance among fiber and liquid cells that comprise the ensemble.

Consider a two-dimensional Ising model: the field is divided into a lattice frame of $L \times L$ square cells, as shown in Fig. 46. The total Hamiltonian of the system is considered as a sum of all the contributions of the cell energies in the lattice. When only the interactions between nearest neighbors are considered, the Hamiltonian can be expressed as:

$$H = -\left(B_0 \sum_i s_i F_i + B_1 \sum_{i,j} s_i F_j\right) - C \sum_{i,j} s_i s_j + G_g \sum_i s_i y \tag{124}$$

where the first term in the bracket represents the interaction between liquid and fiber substrate spins that coexist in one cell while the second term in the bracket represents those in the neighboring cells, and the coefficient $B_i\,(i = 0,1)$ is the adhesive energy of interaction between fiber and liquid. The second term represents the interaction between liquid spins, and C is the cohesive energy of liquid. The last term represents the energy of a liquid spin in the gravitational field, of which G_g is the intensity of the gravity field and y the y-coordinate of the cell in the lattice.

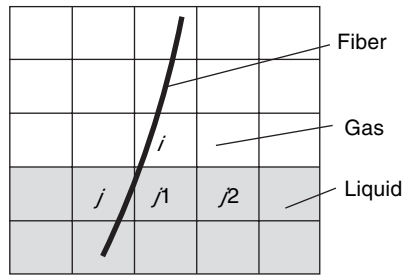

Fig. 46 Two-dimensional Ising model

Different from Equation (119) for the case of a ferromagnet, where the Ising variables are scheduled to be $s_i = 1$ or -1 depending on the spin pointing up or down, new sets of variables $s_i = 1$ or 0, $F_i = 1$ or 0 are adopted to study the wetting dynamics. As known, the exchange energies associated with the magnetic moment of a pair of

neighboring cells bearing the same spin variable, either 1 or –1, are identical; whereas the pair with opposite spin variables takes a negative value in reference to the former. However, in the case of the wetting process, as cohesion energy is involved only in the interaction between liquid cells, it is not expected to see a pair of empty cells having identical interaction energy as the pair of liquid filled cells, so the spin variable system 1 and –1 can no longer be maintained. This argument provides the basis for adopting the variable as 1 and 0. Reasoning in the same way, similar conclusion can be drawn for the other energy terms.

The Hamiltonian of a single cell j, referring to Fig. 46, is calculated as an example shown in Table 2. The total Hamiltonian for the system is the summation of all the Hamiltonians from the $L \times L$ cells.

Table 2 Hamiltonian of a single cell j

s_j	y	F_j	$B_0 \times s_j F_j$	$B_1 \times \sum s_j F_j$	$C \times \sum s_j s_j$
1	6	1	$B_0 \times 1$	$B_1 \times 2$	$C \times 5$
		$H_j = -(B_0 \times 1 + B_1 \times 2) - C \times 5 + G_g \times 1 \times 6$			

The coefficients in Equation (124) are further discussed with a rationale that follows. Assuming that the van de Waals forces dominate the interactions between fiber and liquid, according to the Lifshitz theory [454], the interaction energy per unit area between two surfaces can be expressed as

$$W_{1,2} = \frac{-h_{1,2}}{12\,\pi\,D^2} \tag{125}$$

where $h_{1,2}$ is the Hamaker constant and D the distance between the surfaces. An approximate expression for the Hamaker constant of two bodies (1 and 2) interacting across a medium 3, none of them being a conductor, is

$$h_{1,2} = \frac{3hv_e\,(n_1^2 - n_3^2)(n_2^2 - n_3^2)}{8\sqrt{2}\,(n_1^2 + n_3^2)^{1/2}\,(n_2^2 + n_3^2)^{1/2}[(n_1^2 + n_3^2)^{1/2} + (n_2^2 + n_3^2)^{1/2}]} \tag{126}$$

$$+ \frac{3}{4}kT\,\frac{\varepsilon_1 - \varepsilon_3}{\varepsilon_1 + \varepsilon_3}\,\frac{\varepsilon_2 - \varepsilon_3}{\varepsilon_2 + \varepsilon_3}$$

where h is the Planck's constant, v_e is the main electronic adsorption frequency in the UV (assumed to be the same for the three bodies, and typically around 3×10^{15} s^{-1}), and n_i is the refractive index of phase i, ε_i is the static dielectric constant of phase i, k is the Boltzmann constant, and T the absolute temperature.

The constants k_1 and k_2 are used to represent the ratios of C/B_0 and B_1/B_0, respectively,

$$k_1 = \frac{C}{B_0} = \frac{W_{1,2}}{W_{1,1}} = \frac{h_{1,2}}{h_{1,1}}, \quad k_2 = \frac{B_1}{B_0} = \frac{\pi\,dal}{a^2} = \frac{\pi\,dl}{a} \tag{127}$$

and the ratio B_1/B_0 is equal to the ratio of the adhesive surface areas in each case. The area for coefficient B_1 is calculated as the total surface of l individual filaments (with diameter d) in the yarn within a cubic cell (with side length a), assuming that the

filaments within the yarn are evenly packed and straight along the axis of the yarn, and the area for coefficient B_0 is calculated as the area of the cell. The value of B_0 is determined by simulation to accommodate the experimental data. And the values of C and B_1 are then determined by Equation (127).

For a thermodynamic system such as the one we are dealing with, the macro behavior of the system is not governed by the internal energy alone, due to the existence of the stochastic thermal agitation. Therefore, a probabilistic approach is added here to reflect this influence.

Let us consider the Ising model as a thermodynamics system connected with a thermodynamics reservoir, and energy exchange can occur between them. The system, together with the reservoir, forms a canonical assembly that is governed by the Boltzmann distribution of the state probability ratio

$$\frac{P(H_1)}{P(H_2)} = \Lambda = \exp\left(-\frac{1}{\tau}\Delta H\right) \tag{128}$$

where the parameter τ is proportional to the absolute temperature, and Λ is the ratio of $P(H_1)$ and $P(H_2)$. $P(H_k)$, ($k = 1$ and 2) is the probability that the system exists with configuration associated with energy H_k. Λ is then a measure of the likelihood for the system to change its configuration, through spin exchange, from the state with energy H_1 to the state with energy H_2. The energy difference $H_1 - H_2$ denoted by ΔH is the difference of the total system energy before and after the spin exchange. The dynamics are realized by spin exchange that occurs over distances and this kind of dynamics is in the literature described as Kawasaki dynamics [453]. Two cells are randomly chosen on the interface between fluid and air. One of them has the spin variable $s_i = + 1$ and the other $s_j = 0$. A random number $r \in [0, 1]$ is then generated. In the case r is less than the probability for spin exchange that is given by the Boltzmann law, i.e.

$$r < \Lambda = \exp\left(-\frac{1}{\tau}\Delta H\right) \tag{129}$$

these two spins will exchange their position.

The implication of the connection between the energy state and the spin exchange probability in Equation (129) is very important. Since the probability Λ cannot be greater than 1, the case where $\Delta H < 0$ is not viable, and no spin exchange will take place under this condition since it represents a transition from a lower energy state to a higher one. When $\Delta H = 0$ so that $\Lambda = 1 > r \leq 1$, the spin exchange is possible but with a very small probability (only occurring when $r = 1$). Whereas when $\Delta H > 0$ and $r \leq \Lambda < 1$, spin exchange is encouraged and most likely to occur.

The total energy E is then used in the Monte Carlo simulation to predict the wetting behavior of a liquid in fiber assemblies. The procedures of the simulation are as follows:

(i) Initial configuration is created by developing the lattice, above which the fibrous assembly is laid. The initial values of both F (1 or 0) and s (1 or 0) for each cell are also determined. A cell i is considered to be covered with fiber ($F = 1$) if the distance between the cell center and the fiber axis is smaller than the fiber radius.

(ii) Scanning the liquid–fiber interface. A cell i in the lattice is randomly selected. If there is one or more nearest neighbor cells whose values of s are different from cell i, cell i is supposed to be on the interface. As shown in Fig. 46, empty cell i is next to three liquid cells and five empty cells, each liquid cell, j, $j1$ and $j2$ having the opportunity to exchange spin values with cell i, but with different probabilities.

(iii) Cell i can be paired with j, $j1$ or $j2$. For each pair, ΔE, which is the energy difference between the configurations before and after the exchange of spin values of the two cells, can be calculated by Equation (128). Then the pair with the lowest value of ΔE is selected as the most probable exchange. Next, if the random number r selected between 0 and 1 satisfies Equation (129), the exchange of the two spins will take place. Otherwise select the pair with the lowest least value of ΔE.

8.5.2 Model Predictions and Experimental Verification [449–452]

To testify the validity of the model described here, a set of wicking experiments was performed. Experiments were carried out at room temperature. Test samples included three types of polypropylene filament yarns with the same yarn count but different fineness of constituent filaments. Their specifications are listed in Table 3. The samples were extracted with acetone in a Soxhlet extractor for 2 hours to remove surfactant. Then the yarns were twisted to 5 turns/10 cm to ensure a uniform cross section along the length of the sample, with the filaments in the sample evenly packed. Such a weak twist maintains the validity of the assumption of a straight state of filaments within the samples. Each sample was hung vertically by a clamp and the free end was dipped into a bath containing a 1% solution of methylene blue. A small weight was attached to the free end of the sample by means of a hook, to maintain the sample in a vertical state. The traveling height of the liquid was measured during wicking tests. To obtain the wetting rate, the time required for the dye solution to travel upwards along the sample was recorded.

Table 3 Specifications of PP yarn samples

Sample	Yarn count (tex)	Yarn diameter (mm)	Filament fineness (dtex)	No. of filaments in a yarn	Filament diameter (μm)
1	13.4	0.282	2.25	60	18
2	13.4	0.290	1.5	90	14.6
3	13.4	0.322	0.6	224	9.2

In the simulation, the plane is divided into 9×150 square cells. For the convenience of calculating the weight (from the volume) of the liquid in a cell and the interfacial area between two cells, each cell is supposed to be a cube. The dimension of a cell are determined according to the dimension of the test samples. For example, in the case of Sample 1, the width of a cell is equal to the diameter of the yarn. Thus, each cell represents a volume of $0.282 \times 0.282 \times 0.282$ mm^3.

Let each Monte Carlo step represent 1 second. The parameters needed in the

simulation are listed in Table 4. The experimental as well as the simulation results of the wetting rate are shown in Fig. 47. The constant B_0 is chosen as 3.72. The constants k_1 and k_2 are calculated by Equation (127) as

$k_1 = 1.34$, $k_2 = 12.0$ (for Sample 1); $k_2 = 14.2$ (for Sample 2); $k_2 = 20.1$ (for Sample 3) and $\beta = \frac{1}{4}$

Table 4 Parameters for fiber and liquid at room temperature (20°C) [449–452]

	ρ (g/cm^3)	γ_{lg} (10^{-3}N/m)	γ_{fg} (10^{-3}N/m)	n_i	ε_i	θ
PP	0.905	—	29.4	1.490	2.2	86°
Water	0.998	72.75	—	1.333	80	

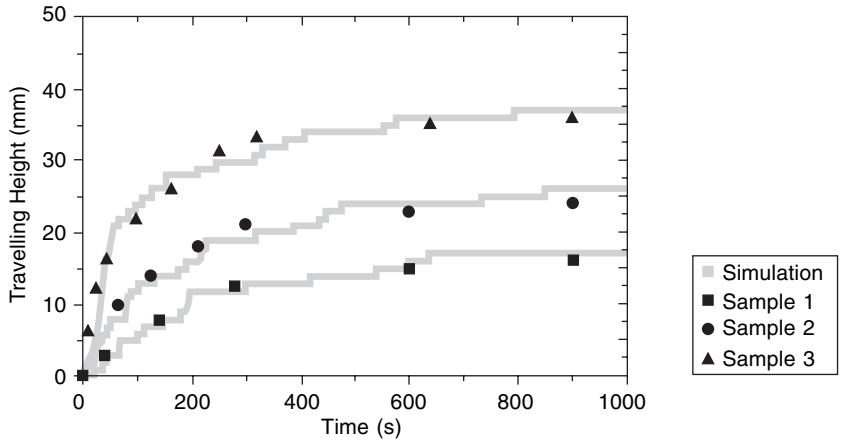

Fig. 47 Ascending height of liquid versus time

The results of the experiments and the simulations show considerable agreement. Keeping the yarn count as constant, with the decrease of filament diameter in the yarn the total surface area of a unit length of the yarn increases, which in turn causes an increase in the interaction area of fiber and liquid and in the interaction energy, resulting in better wettability of the yarn. This outcome also agrees well with the phenomena reported in various references.

Both the experiments and simulations show that climbing height rises substantially at first and then slows down, asymptotically approaching a plateau where the effect of gravity on the liquid column cannot be ignored. It reveals that the Washburn Equation is limited in predicting the wicking properties of fibrous assemblies.

The dimension of the cells in the lattice frame can be further refined, for example, to be equal to the diameter of a single fiber or filament in a yarn, so as to increase the precision of the simulation as well as to demonstrate the simulation of the wetting process of the yarns in more detail. The wicking process of a filament tow is shown in Fig. 48. These filaments are depicted as a set of sine curves with different phases

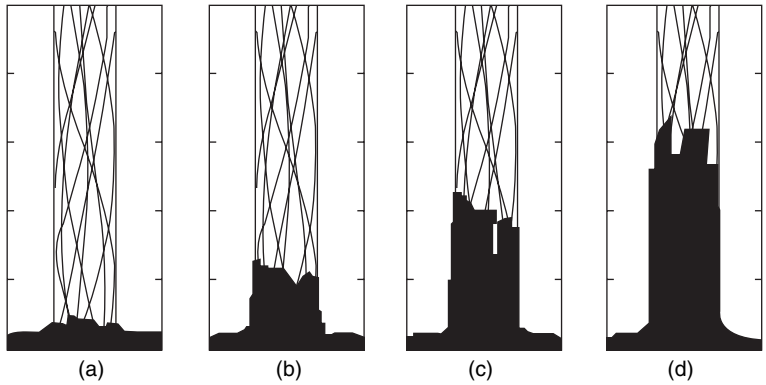

Fig. 48 Wetting process in a tow of filaments, after, (a) 5 Monte Carlo steps, (b) 25 Monte Carlo steps, (c) 50 Monte Carlo steps, (d) 100 Monte Carlo steps

responsive to being twisted. The lattice size is 100×40. The width of each cell is equal to the diameter of a filament d. The parameters are chosen as:

$$B_0 = 3.72,\ k_1 = 1.34,\ k_2 = 14.2,\ d = 9.2\ \mu\text{m and } \beta = {}^1/_4$$

It can be seen that the traveling rates of liquid vary in different areas. This agrees with the fact that the liquid front in a tow is not always a straight line in experiments. The liquid tends to rise more rapidly in areas where packing densities are higher. In areas where packing densities are quite low, empty holes tend to form, indicating an imperfect wetting state. The simulation also shows that the traveling rate of the liquid slows down with time, and the width of the liquid column decreases with height due to the balance of surface tension and gravity.

The above example indicates that the method described in the study is useful when applied to predict wicking behavior of various yarns. The model can easily be modified to adapt to investigations of more complicated cases, such as the wetting process of a liquid on a more complex pattern of structures, various types of fabrics or nonwovens, or the flow behavior of fluid through porous media. The model can be modified to adapt to wetting processes of liquid on more complex patterns of structures by altering the initial configuration of fiber assemblies and inputting parameters of different fiber types and liquids. The simulation results can be further improved by expanding the model into a three-dimensional one.

The fiber assembly for the wetting simulation is created in the following way. The fibers are considered straight and identical in length and radius, and both values as well as the total fiber number are given as the input parameters for simulation. The distribution of fibers in the Ising model lattice are specified using the center along a fiber length as the location parameter, and, for the planar fiber network case, using an angular variable $0 \le \phi \le \pi$ as the direction parameter defined as the angle of the fiber with respect to the vertical direction y.

In this way, more trials have been run using our prototype algorithm. One result of the liquid wetting simulation in a fiber network is shown in Fig. 49. The fibers are considered as randomly distributed.

To show the behavior of liquid transport through fibrous structures in more detail,

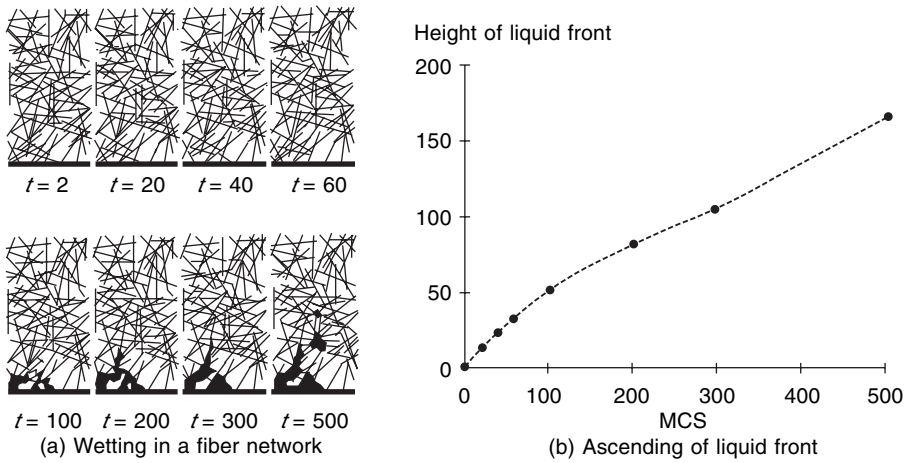

Fig. 49 Wetting process in a random fiber network

results of a computer simulation for a dynamic process of spreading a liquid drop on a fiber are shown in Fig. 50 [429], depicting the changing shape of the liquid drop after several different time periods.

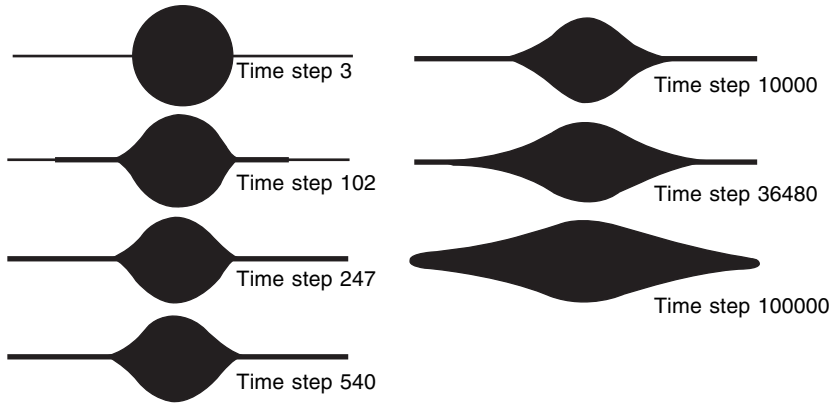

Fig. 50 A 2-D simulation of a liquid drop spreading on a fiber

Figure 51 [430] shows the 3-D computer simulation output of the transient process of a liquid body in interaction with a partially dipped fiber.

8.6 From Statistical Mechanics to Macro Properties of Fibrous Materials

Next is a simulation on the influence of fiber orientation on the dynamics of liquid wetting and wicking into a fibrous mass. Fiber declination β from the vertical axis H is varied with a step of 10°, so the simulation was carried out for 11 different fibrous systems with $\beta = 0°$, 10°, 20°…90°, plus $\beta = 45°$.

Results of this process are provided in Fig. 52; each picture is a paired wetting pattern of a side view and a top view (a cross section) , of the fibrous mass at a given β value. The horizontal cross-sections are all cut at the distance of 100 cells from the

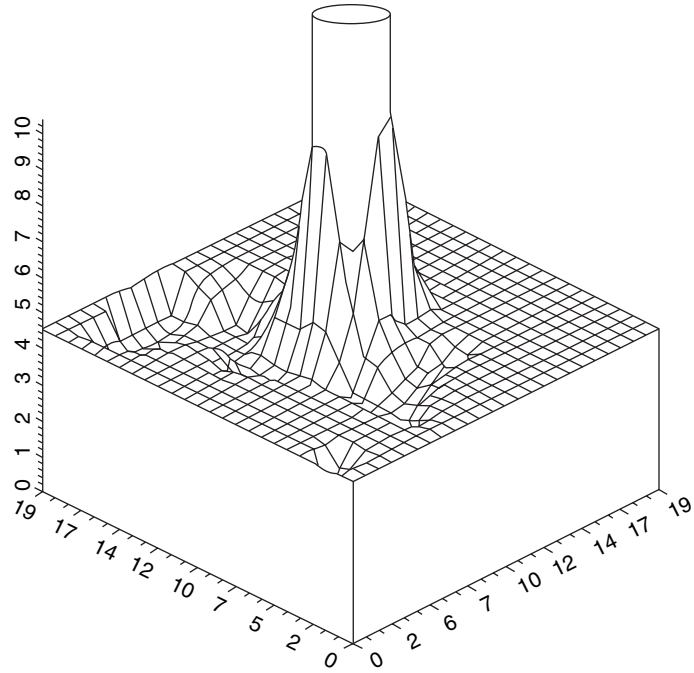

Fig. 51 Simulation of the transient process of liquid climbing along a single fiber

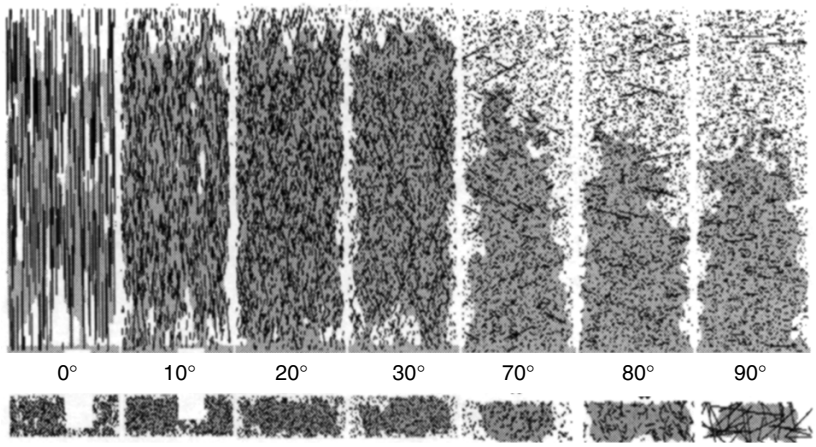

Fig. 52 Wetting patterns (vertical and horizontal cross-sections) of a fiber mass with different β after 600 Monte Carlo steps

liquid surface. Two extreme behaviors can be seen. The first is the plane of $\beta = 0°$ where the ascending liquid moves at a highest rate but is most scattered. The other one is in parallel or $\beta = 90°$ with the lowest wetting rate, but the liquid pattern is most heavily aggregated.

Figure 53 gives the simulated relationship of mass m (number of liquid cells) absorbed by fiber vs. (a) time (Monte Carlo steps, MCS) and (b) β, respectively. It is

 doi:10.1533/tepr.2006.0002

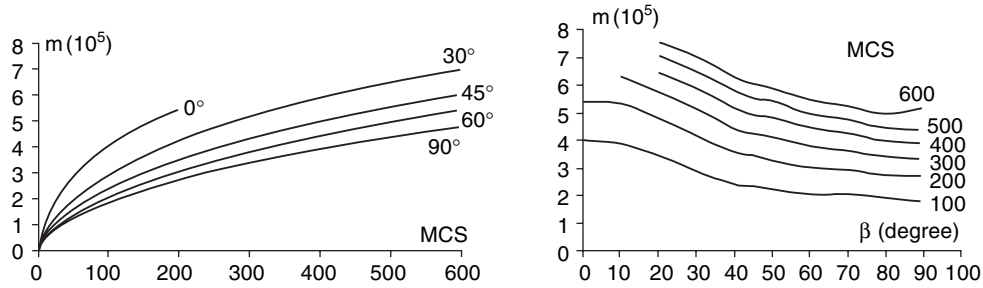

Fig. 53 (a) Liquid taken by specimen vs. MCS (b) Liquid taken by specimen vs. β

clear that after a short time, i.e. *MCS* <200, the absorbed liquid body in general is more voluminous for a smaller angle β because apparently, the fiber assemblies with smaller β values start with greater wicking rates and therefore the liquid climbs faster. Nevertheless, this trend remains true in our calculation only for those with $\beta \geq 20°$, whareas in the cases $\beta < 20°$, the climbing of the liquid stagnates and becomes independent of the time; the smaller the β value, the earlier the climbing stops.

The discussions above reveal that there will be one or a range of optimal combinations of β and MCS at which the fiber mass will absorb the maximum amount of liquid, a result of optimal wicking rate and wicking duration as shown in Fig. 53 (b); when $\beta = 20°$, the greater the MCS value, the more liquid absorbed.

From the point of view of statistical thermodynamics, the wetting behavior is the reflection of the interactions and the resulting balance among fiber and liquid cells that comprise the system. A statistical model, the two-dimensional Ising model combined with the Monte Carlo simulation, is applied to describe the wetting process, which is regarded as a process where spaces between fibers change from a gas dominant to a liquid dominant state. Such change is driven by the difference in energy between the two states, affected by the random thermal fluctuations, and is finally terminated by the balance of surface tension and gravity.

The examples here are just the results of some preliminary trials, only to show the usefulness of the present method. We have also expanded this model in predicting the fiber pull-out process [455] and tear fracture of a coated fabric [456].

From the above contents, several advantages can be found for the proposed approach. First, the Ising model can describe a complex physical phenomenon in a very simple binary form, yet still be able to account for all the mechanisms involved and yield realistic results. This makes the model a very attractive, practical and powerful tool to study the phenomenon of liquid transport in fiber networks, and the very complex wetting processes can be realistically simulated without employing intricate mathematical operations. Also, the constants associated with the energy terms have clear physical meanings, and they, in fact, represent the properties of the media involved. Thus, by adjusting the values of these constants, we can carry out a series of parametric studies of the influence of these properties on a specific problem under investigation. The proposed simulation technique will enable us to obtain information about the nature and mechanisms of the fiber mass wetting behavior. All the important interactions and factors have been included in terms of the energies they contribute to the whole process. The results from this project including the computer software

will provide guidance to some important practical issues and a powerful tool for understanding and monitoring the key factors in improving the quality of various products.

Needless to say, for a phenomenon as complex as wetting in fibrous materials, much remains to know and be done.

9. REFERENCES

[1] Ambarzumian, V.A., Diffuse reflection of light by a foggy medium. *Comptes Rendus (Doklady) de l'Acadimie des Sciences de l'URSS*, 1943. **38**: p. 229–232.
[2] Ambarzumian, V.A., *Theoretical Astrophysics*. 1958, New York: Pergarnon Press.
[3] Wing, M.G., *An Introduction to Transport Theory*. 1962, New York: John Wiley & Sons, Inc.
[4] Bear, J., *Introduction to Modeling of Transport Phenomena in Porous Media*. 1995: Kluwer Academic.
[5] Bird, R.B., Stewart, W.E. and Lightfoot, E.N., *Transport Phenomena*. 1980, New York: John Wiley.
[6] Gekas, V., *Transport Phenomena of Foods and Biological Materials*. 1986: CRC Publishing Inc.
[7] Heuer, A.H., *Mass Transport Phenomena in Ceramics*. 1975, New York: Plenum Pub. Corp.
[8] Mashelkar, R.A., Mujumdar, A.S. and Kamal, R. (Eds), *Transport Phenomena in Polymeric Systems*. 1989, New York: Prentice Hall.
[9] Slattery, J.C., *Interfacial Transport Phenomena*. 1991, New York: Springer Verlag.
[10] Smith, H. and Jensen, H., *Transport Phenomena*. 1989, Oxford: Clarendon Press.
[11] van Heuven, J.W., *Transport Phenomena*. 1999, New York: John Wiley & Sons.
[12] Ziman, J.M., *Electrons and Phonons: The Theory of Transport Phenomena in Solids*. 1979: Oxford: Oxford University Press.
[13] Morgenstern, I., Binder, K. and Hornreich, R.M., Two-dimensional Ising Model in Random Magnetic Fields. *Physical Review B*, 1981. **23**(1): p. 287–297.
[14] Schmid, F. and Binder, K. Modeling Order–Disorder and Magnetic Transitions in Iron–Aluminum Alloys. *Journal of Physics–Condensed Matter*, 1992. **4**(13): p. 3569–3588.
[15] Oner, D. and McCarthy, T.J., Ultrahydrophobic surfaces. Effects of topography length scales on wettability. *Langmuir*, 2000, **16**(20): p. 7777–7782.
[16] Fohr, J.P., Couton, D. *et al*., Dynamic heat and water transfer through layered fabrics. *Textile Research Journal*, 2002. **72**: p. 1–12.
[17] Cox. H.L., The Elasticity and Strength of Paper and Other Fibrous Materials. *Br. J. Appl. Phy*., 1952. **3**: p. 72.
[18] Corte, H. and Kallmes, O., *Statistical Geometry of a Fibrous Network, Formation and Structure of Paper*, ed. F. Bolom. Vol. 1. 1962, London: *Tech. Sect. Brit*. Papers and Board Makers Assn. 13.
[19] Kallmes, O. and Corte, H., The structure of paper: I. The statistical geometry of an ideal two-dimensional fiber network. *Tappi*, 1960. **43**: p. 737.
[20] Kallmes, O. and Bernier, G., The structure of paper: IV. The bonding states of fibers in randomly formed papers. *Tappi*, 1963. **46**: p. 493.
[21] Kallmes, O., Corte, H. and Bernier, G., The structure of paper: V. The free fiber length of a multiplanar sheet. *Tappi*, 1963. **46**: p. 108.
[22] Kallmes, O., *A Comprehensive View of the Structure of Paper*. Theory and Design of Wood and Fiber Composite Materials, ed. B.A. Jayne. 1972, Syracuse: Syracuse University Press. 157.
[23] Gurnagul, N. *et al*., The Mechanical Permanence of Paper - a Literature Review. *Journal of Pulp and Paper Science*, 1993. **19**(4): p. J160–J166.
[24] Michell, A.J., Seth, R.S. and Page, D.H., The Effect of Press Drying on Paper Structure. *Paperi Ja Puu-Paper and Timber*, 1983. **65**(12): p. 798.
[25] Page, D.H., The meaning of Nordman bond strength. *Nordic Pulp & Paper Research Journal*, 2002. **17**(1): p. 39–44.
[26] Page, D.H., A Quantitative Theory of the Strength of Wet Webs. *Journal of Pulp and Paper Science*, 1993. **19**(4): p. J175–J176.
[27] Page, D.H. and Howard, R.C., The Influence of Machine Speed on the Machine-direction Stretch of Newsprint. *Tappi Journal*, 1992. **75**(12): p. 53–54.
[28] Page, D.H. and Seth, R.S., A Note on the Effect of Fiber Strength on the Tensile-strength of Paper. *Tappi Journal*, 1988. **71**(10): p. 182–183.
[29] Page, D.H. and Seth, R.S., The Elastic-modulus of Paper. 3. The Effects of Dislocations, Microcompressions, Curl, Crimps, and Kinks. *Tappi*, 1980. **63**(10): p. 99–102.
[30] Page, D.H. and Seth, R.S., The Elastic-modulus of Paper. 2. The Importance of Fiber Modulus, Bonding, and Fiber Length. *Tappi*, 1980. **63**(6): p. 113–116.
[31] Page, D.H. and Seth, R.S., Structure and the Elastic-Modulus of Paper. *Abstracts of Papers of the American Chemical Society*, 1980. **179**(MAR): p. 27-CELL.
[32] Page, D.H., Seth, R.S. and Degrace, J.H., Elastic-modulus of Paper. 1. Controlling Mechanisms. *Tappi*, 1979. **62**(9): p. 99–102.

[33] Schulgasser, K. and Page, D.H., The Influence of Transverse Fiber Properties on the Inplane Elastic Behavior of Paper. *Composites Science and Technology*, 1988. **32**(4): p. 279–292.
[34] Seth, R.S. and Page, D.H., The problem of using Page's equation to determine loss in shear strength of fiber–fiber bonds upon pulp drying. *Tappi Journal*, 1996. **79**(9): p. 206–210.
[35] Seth, R.S. and Page, D.H. Fracture Resistance – Failure Criterion for Paper. *Tappi*, 1975. **58**(9): p. 112–117.
[36] Perkins, R.W. and Mark, R.E., Effects of Fiber Orientation Distribution on the Mechanical Properties of Paper. *Paperi Ja Puu-Paper and Timber*, 1983. **65**(12): p. 797–797.
[37] Perkins, R.W. and Mark, R.E., A Study of the Inelastic Behavior of Paper. *Paperi Ja Puu-Paper and Timber*, 1983. **65**(12): p. 797–798.
[38] Perkins, R.W. and Mark, R.E., Structural Theory of Elastic Behavior of Paper. *Tappi*, 1976. **59**(12): p. 118–120.
[39] Perkins, R.W. and Mark, R.E., *Concerning Micromechanics Models for the Elastic Behavior of Paper*. Mechanics of Cellulosic and Polymeric Materials, ed. R.W. Perkins. 1989, New York: The American Society of Mechanical Engineering. 23.
[40] Ramasubramanian, M.K. and Perkins, R.W., Computer-simulation of the Uniaxial Elastic–Plastic Behavior of Paper. *Journal of Engineering Materials and Technology-Transactions of the Asme*, 1988. **110**(2): p. 117–123.
[41] Castagnede, B., Ramasubramanian, M.K. and Perkins, R.W., Measurement of Lateral Contraction Ratios for a Machine-made Paper and Their Computation Using a Numerical Simulation. *Comptes Rendus De L Academie Des Sciences Serie Ii*, 1988. **306**(2): p. 105–108.
[42] Deng, M. and Dodson, C.T.J., Random Star Patterns and Paper Formation. *Tappi Journal*, 1994. **77**(3): p. 195–199.
[43] Deng, M. and Dodson, C.T.J., Paper: An Engineered Stochastic Structure. 1994, Atlanta: TAPPI Press.
[44] Dodson, C.T.J., Fiber crowding, fiber contacts, and fiber flocculation. *Tappi Journal*, 1996. **79**(9): p. 211–216.
[45] Dodson, C.T.J., The Effect of Fiber Length Distribution on Paper Formation. *Journal of Pulp and Paper Science*, 1992. **18**(2): p. J74–J76.
[46] Dodson, C.T.J. and Fekih, K., The Effect of Fiber Orientation on Paper Formation. *Journal of Pulp and Paper Science*, 1991. **17**(6): p. J203–J206.
[47] Dodson, C.T.J., Oba, Y. and Sampson, W.W., Bivariate normal thickness–density structure in real near-planar stochastic fiber networks. *Journal of Statistical Physics*, 2001. **102**(1–2): p. 345–353.
[48] Dodson, C.T.J. and Sampson, W.W., Spatial statistics of stochastic fiber networks. *Journal of Statistical Physics*, 1999. **96**(1–2): p. 447–458.
[49] Dodson, C.T.J. and Schaffnit, C., Flocculation and Orientation Effects on Paper-Formation Statistics. *Tappi Journal*, 1992. **75**(1): p. 167–171.
[50] Schaffnit, C. and Dodson, C.T.J., A New Analysis of Fiber Orientation Effects on Paper Formation. *Paperi Ja Puu-Paper and Timber*, 1994. **76**(5): p. 340–346.
[51] Scharcanski, J. and Dodson, C.T.J. Simulating colloidal thickening: Virtual papermaking. *Simulation*, 2000. **74**(4): p. 200–206.
[52] Scharcanski, J. and Dodson, C.T.J., Neural network model for paper-forming process. *Ieee Transactions on Industry Applications*, 1997. **33**(3): p. 826–839.
[53] Scharcanski, J., Dodson, C.T.J. and Clarke, R.T., Simulating effects of fiber crimp, flocculation, density, and orientation on structure statistics of stochastic fiber networks. *Simulation–Transactions of the Society for Modeling and Simulation International*, 2002. **78**(6): p. 389–395.
[54] van Wyk, C.M., Note on the compressibility of wool. *Journal of Textile Institute*, 1946. **37**: p. 282.
[55] Komori, T. and Itoh, M., Theory of the General Deformation of Fiber Assemblies. *Textile Research Journal*, 1991. **61**(10): p. 588–594.
[56] Komori, T. and Itoh, M., A Modified Theory of Fiber Contact in General Fiber Assemblies. *Textile Research Journal*, 1994. **64**(9): p. 519–528.
[57] Komori, T. and Itoh, M. Analyzing the compressibility of a random fiber mass based on the modified theory of fiber contact. *Textile Research Journal*, 1997. **67**(3): p. 204–210.
[58] Komori, T., Itoh, M. and Takaku, A., A Model Analysis of the Compressibility of Fiber Assemblies. *Textile Research Journal*, 1992. **62**(10): p. 567–574.
[59] Komori, T. and Makishima, K., Estimation of Fiber Orientation and Length in Fiber Assemblies. *Textile Research Journal*, 1978. **48**(6): p. 309–314.
[60] Komori, T. and Makishima, K., Numbers of Fiber to Fiber Contacts in General Fiber Assemblies. *Textile Research Journal*, 1977. **47**(1): p. 13–17.
[61] Lee, D.H and Lee, J.K., Initial Compressional Behavior of Fiber Assembly, in *Objective Measurement: Applications to Product Design and Process Control*, (Kawabata, S., Postle, R. and Niwa, M., Editors). 1985, The Textile Machinery Society of Japan: Osaka. p. 613.
[62] Chen, C.C. and Duckett, K.E., The Direction Distribution on Cross–contacts Points in *Anisotropic Fiber Assemblies*. *Textile Res. J*., 1979. **49**: p. 379.

[63] Duckett, K.E. and Chen, C.C., *Discussion of Cross-point Theories of van Wyk. Journal of the Textile Institute*, 1978. **69**(2–3): p. 55–59.
[64] Beil, N.B. and Roberts, W.W., Modeling and computer simulation of the compressional behavior of fiber assemblies - I: Comparison to van Wyk's theory. *Textile Research Journal*, 2002. **72**(4): p. 341–351.
[65] Carnaby, G.A. and Pan, N., Theory of the Compression Hysteresis of Fibrous Assemblies. *Textile Research Journal*, 1989. **59**(5): p. 275–284.
[66] Pan, N. and Carnaby, G.A., Theory of the Shear Deformation of Fibrous Assemblies. *Textile Research Journal*, 1989. **59**(5): p. 285–292.
[67] Pan, N., A Modified Analysis of the Microstructural Characteristics of General Fiber Assemblies. *Textile Research Journal*, 1993. **63**(6): p. 336–345.
[68] Pan, N., *et al*., Micromechanics of a planar hybrid fibrous network. *Textile Research Journal*, 1997. **67**(12): p. 907–925.
[69] Narter, M.A., Batra, S.K. and Buchanan, D.R., Micromechanics of three-dimensional fibre webs: constitutive equations. *Proceedings of the Royal Society of London Series a–Mathematical Physical and Engineering Sciences*, 1999. **455**(1989): p. 3543–3563.
[70] Pan, N., Theoretical Determination of the Optimal Fiber Volume Fraction and Fiber-matrix Property Compatibility of Short Fiber Composites. *Polymer Composites*, 1993. **14**(2): p. 85–93.
[71] Pan, N., Analytical Characterization of the Anisotropy and Local Heterogeneity of Short-fiber Composites – Fiber Fraction as a Variable. *Journal of Composite Materials*, 1994. **28**(16): p. 1500–1531.
[72] Gates, D.J. and Westcott, M., Predicting fiber contact in a three-dimensional model of paper. *Journal of Statistical Physics*, 1999. **94**(1–2): p. 31–52.
[73] Parkhouse J. and Kelly, A., The random packing of fibers in three dimensions. *Proc: Math. and Phy. Sci. Roy. Soc*., 1995. **A 451**: p. 737.
[74] Pan, N., Fiber Contact in Fiber Assemblies. *Textile Research Journal*, 1995. **65**(10): p. 618–618.
[75] Ogston, A.G., The Spaces in a Uniform Random Suspension of Fibers. *Trans. Faraday Soc*., 1958. **54**: p. 1754–1757.
[76] Komori, T. and Makishima, K., Geometrical Expressions of Spaces in Anisotropic Fiber Assemblies. *Textile Res. J*., 1979. **49**: p. 550–555.
[77] Kendall, M.G. and Moran, P.A.P., *Geometrical Probability*. 1963, London: Charles Griffin and Co. Ltd. 37.
[78] Pan, N., Development of a Constitutive Theory for Short fiber Yarns Part III: Effects of Fiber Orientation and Fiber Bending Deformation. *Textile Research Journal*, 1993. **63**: p. 565–572.
[79] Mardia, K.V., *Statistics of Directional Data*. 1972, New York: Academic Press. p. 57.
[80] Sayers, C.M., Elastic Anisotropy of Short–fiber Reinforced Composites. *Int. J. Solids and Structures*, 1992. **29**: p. 2933–2944.
[81] Tournier, J.D., *et al*., Direct estimation of the fiber orientation density function from diffusion-weighted MRI data using spherical deconvolution. *Neuroimage*, 2004. **23**(3): p. 1176–1185.
[82] Kim, H.S., Relationship between fiber orientation distribution function and mechanical anisotropy of thermally point-bonded nonwovens. *Fibers and Polymers*, 2004. **5**: p. 177–181.
[83] de Gennes, P.G., Wetting – Statics and Dynamics. *Reviews of Modern Physics*, 1985. **57**(3): p. 827–863.
[84] de Gennes, P.-G., Brochard-Wyart, F. and Quere, D., Capillarity and Wetting Phenomena: Drops, Bubbles, Pearls, Waves. 2004, New York: Springer.
[85] Kissa, E., Wetting and wicking. *Textile Research Journal*, 1996. **66**(10): p. 660–668.
[86] Adamson, A.W. and Gast, A.P., *Physical Chemistry of Surfaces*. 6th ed. 1997, New York: Wiley.
[87] Fowkes, F.M., Zisman, W.A. and American Chemical Society. Division of Colloid and Surface Chemistry., Contact angle, wettability and adhesion. *The Kendall award symposium honoring William A. Zisman, Los Angeles, Calif., April 2–3, 1963*. 1964, Washington,: American Chemical Society. ix, 389.
[88] Zisman, W.A., Contact angle, wettability and adhesion, in *Advances in Chemistry Series*, F.M. Fowkes, Editor. 1964: Washington, D. C: American Chemical Society.
[89] Israelachvili, J.N., *Intermolecular and Surface Forces*. 2nd ed. 1991, London ; San Diego, CA: Academic Press. xxi, 450.
[90] Hamaker, H.C., The London van der Waals attraction between spherical particles. *Physica*, 1937. **4**(10): p. 1058–1072.
[91] Wennerstrom, H., The van der Waals interaction between colloidal particles and its molecular interpretation. *Colloids and Surfaces a-Physicochemical and Engineering Aspects*, 2003. **228**(1–3): p. 189–195.
[92] Garbassi, F., Morra, M. and Occhiello, E., *Polymer Surfaces : From Physics to Technology*. Rev. and updated ed. 1998, Chichester, England; New York: Wiley.
[93] Wu, S., *Polymer Interface and Adhesion*. 1982, New York: M. Dekker.
[94] Good, R.J., Contact-angle, Wetting, and Adhesion – A Critical Review. *Journal of Adhesion Science and Technology*, 1992. **6**(12): p. 1269–1302.
[95] Washburn, E.W., The dynamics of capillary flow. *Physical Review*, 1921. **17**: p. 273–283.
[96] Minor, F.W., The migration of liquids in textile assemblies, Part II. *Textile Research Journal*, 1959. **29**: p. 931.

[97] Minor, F.W., The migration of liquids in textile assemblies, Part III. *Textile Research Journal*, 1959. **29**: p. 941.
[98] Hodgson, K.T. and Berg, J.C., The Effect of Surfactants on Wicking Flow in Fiber Networks. *Journal of Colloid and Interface Science*, 1988. **121**(1): p. 22–31.
[99] Chwastiak, S., A wicking method for measuring wetting properties of carbon yarns. *Journal of Colloid and Interface Science*, 1973. **42**(2): p. 298–309.
[100] Good, R.J. and Lin, N.J. Rate of Penetration of a Fluid into a Porous Body 2. Verification of Generalization of Washburn Equation, for Organic Liquids in Glass Capillaries. *Journal of Colloid and Interface Science*, 1976. **54**(1): p. 52–58.
[101] Joos, P., Vanremoortere, P. and Bracke, M. The Kinetics of Wetting in a Capillary. *Journal of Colloid and Interface Science*, 1990. **136**(1): p. 189–197.
[102] Marmur, A., Penetration and Displacement in Capillary Systems of Limited Size. *Advances in Colloid and Interface Science*, 1992. **39**: p. 13–33.
[103] Marmur, A. and Cohen, R.D., Characterization of porous media by the kinetics of liquid penetration: The vertical capillaries model. *Journal of Colloid and Interface Science*, 1997. **189**(2): p. 299–304.
[104] Lukas, D., Glazyrina, E. and Pan, N., Computer simulation of liquid wetting dynamics in fiber structures using the Ising model. *Journal of the Textile Institute*, 1997. **88**(2): p. 149–161.
[105] Lukas, D. and Pan, N., Wetting of a fiber bundle in fibrous structures. *Polymer Composites*, 2003. **24**(3): p. 314–322.
[106] Zhong, W., Ding, X. and Tang, Z.L., Modeling and analyzing liquid wetting in fibrous assemblies. *Textile Research Journal*, 2001. **71**(9): p. 762–766.
[107] Zhong, W., Ding, X. and Tang, Z.L., Statistical modeling of liquid wetting in fibrous assemblies. *Acta Physico-Chimica Sinica*, 2001. **17**(8): p. 682–686.
[108] Zhong, W., Ding, X. and Tang, Z.L., Analysis of fluid flow through fibrous structures. *Textile Research Journal*, 2002. **72**(9): p. 751–755.
[109] Quere, D. and Di Meglio, J.M., The Meniscus on a Fiber. *Advances in Colloid and Interface Science*, 1994. **48**: p. 141–150.
[110] Chibowski, E. and Gonzalezcaballero, F., Theory and Practice of Thin-layer Wicking. *Langmuir*, 1993. **9**(1): p. 330–340.
[111] Sauer, B.B. and Carney, T.E., Dynamic Contact-angle Measurements on Glass Fibers – Influence of Fiber Diameter on Hysteresis and Contact Line Pinning. *Langmuir*, 1990. **6**(5): p. 1002–1007.
[112] Clanet, C. and Quere, D., Onset of menisci. *Journal of Fluid Mechanics*, 2002. **460**: p. 131–149.
[113] Schneemilch, M., *et al*., Dynamic wetting and dewetting of a low-energy surface by pure liquids. *Langmuir*, 1998. **14**(24): p. 7047–7051.
[114] Seveno, D. and De Coninck, J., Possibility of different time scales in the capillary rise around a fiber. *Langmuir*, 2004. **20**(3): p. 737–742.
[115] Blake, T.D., *et al*., Contact angle relaxation during droplet spreading: Comparison between molecular kinetic theory and molecular dynamics. *Langmuir*, 1997. **13**(7): p. 2164–2166.
[116] de Ruijter, M.J., Blake, T.D. and De Coninck, J., Dynamic wetting studied by molecular modeling simulations of droplet spreading. *Langmuir*, 1999. **15**(22): p. 7836–7847.
[117] Nederveen, C.J., Absorption of Liquid in Highly Porous Nonwovens. *Tappi Journal*, 1994. **77**(12): p. 174–180.
[118] Ibbett, R.N. and Hsieh, Y.L., Effect of fiber swelling on the structure of lyocell fabrics. *Textile Research Journal*, 2001. **71**(2): p. 164–173.
[119] Schuchardt, D.R. and Berg, J.C., Liquid Transport in Composite Cellulose-Superabsorbent Fiber Networks. *Wood and Fiber Science*, 1991. **23**(3): p. 342–357.
[120] Marmur, A., Kinetics of penetration into uniform porous media: Testing the equivalent-capillary concept. *Langmuir*, 2003. **19**(14): p. 5956–5959.
[121] Staples, T.L. and Shaffer, D.G., Wicking flow in irregular capillaries. *Colloids and Surfaces a-Physicochemical and Engineering Aspects*, 2002. **204**(1–3): p. 239–250.
[122] Brochard, F., Spreading of Liquid-drops on Thin Cylinders – the Manchon Droplet Transition. *Journal of Chemical Physics*, 1986. **84**(8): p. 4664–4672.
[123] Neimark, A.V., Thermodynamic equilibrium and stability of liquid films and droplets on fibers. *Journal of Adhesion Science and Technology*, 1999. **13**(10): p. 1137–1154.
[124] McHale, G., *et al*., Estimation of contact angles on fibers. *Journal of Adhesion Science and Technology*, 1999. **13**(12): p. 1457–1469.
[125] McHale, G., *et al*., Wetting of a high-energy fiber surface. *Journal of Colloid and Interface Science*, 1997. **186**(2): p. 453–461.
[126] Quere, D., Fluid coating on a fiber. *Annual Review of Fluid Mechanics*, 1999. **31**: p. 347–384.
[127] Bauer, C., Bieker, T. and Dietrich, S. Wetting-induced effective interaction potential between spherical particles. *Physical Review E*, 2000. **62**(4): p. 5324–5338.
[128] Bieker, T. and Dietrich, S., Wetting of curved surfaces. *Physica A*, 1998. **259**(3–4): p. 466–467.
[129] Carroll, B.J., Accurate Measurement of Contact-angle, Phase Contact Areas, Drop Volume, and Laplace Excess Pressure in Drop-on-Fiber Systems. *Journal of Colloid and Interface Science*, 1976. **57**(3): p. 488–495.

[130] Carroll, B.J., The Equilibrium of Liquid-drops on Smooth and Rough Circular Cylinders. *Journal of Colloid and Interface Science*, 1984. **97**(1): p. 195–200.
[131] Carroll, B.J., Direct Measurement of the Contact-angle on Plates and on Thin Fibers – Some Theoretical Aspects. *Journal of Adhesion Science and Technology*, 1992. **6**(9): p. 983–994.
[132] McHale, G. and Newton, M.I., Global geometry and the equilibrium shapes of liquid drops on fibers. *Colloids and Surfaces a-Physicochemical and Engineering Aspects*, 2002. **206**(1–3): p. 79–86.
[133] Carroll, B.J., Equilibrium Conformations of Liquid-drops on Thin Cylinders under Forces of Capillarity – A Theory for the Roll-up Process. *Langmuir*, 1986. **2**(2): p. 248–250.
[134] Kumar, A. and Hartland, S., Measurement of Contact Angles from the Shape of a Drop on a Vertical Fiber. *Journal of Colloid and Interface Science*, 1990. **136**(2): p. 455–469.
[135] Mullins, B.J., et al., Effect of fiber orientation on fiber wetting processes. *Journal of Colloid and Interface Science*, 2004. **269**(2): p. 449–458.
[136] Yoshikawa, S. *et al*., Experimental-study of Flow Mechanics in a Hollow-fiber Membrane Module for Plasma Separation. *Journal of Chemical Engineering of Japan*, 1992. **25**(5): p. 515–521.
[137] Ghali, K., Jones, B. and Tracy, J., Experimental Techniques for Measuring Parameters Describing Wetting and Wicking in Fabrics. *Textile Research Journal*, 1994. **64**(2): p. 106–111.
[138] Mao, N. and Russell, S.J., Anisotropic liquid absorption in homogeneous two–dimensional nonwoven structures. *Journal of Applied Physics*, 2003. **94**(6): p. 4135–4138.
[139] Dimitrov, A.S. *et al*., Contact-angle Measurements with Sessile Drops and Bubbles. *Journal of Colloid and Interface Science*, 1991. **145**(1): p. 279–282.
[140] Butt, H.-J., Graf, K. and Kappl, M., Physics and Chemistry of Interfaces. 2003, Weinheim: Wiley-VCH. xii, 361.
[141] Bascom, W.D., The Wetting Behavior of Fibers, in *Modern Approaches to Wettability: Theory and Applications*, Malcolm E. Schrader and G. Loeb, Editors. 1992, Plenum Press: New York. p. 359–373.
[142] Lee, Y.N. and Chiao, S.M., Visualization of dynamic contact angles on cylinder and fiber. *Journal of Colloid and Interface Science*, 1996. **181**(2): p. 378–384.
[143] Le, C.V., Ly, N.G. and Stevens, M.G., Measuring the contact angles of liquid droplets on wool fibers and determining surface energy components. *Textile Research Journal*, 1996. **66**(6): p. 389–397.
[144] Gu, Y.G. and Li, D.Q., Measurements of contact angles between an oil-water interface and a fiber by the ACDPAC technique. *Journal of Colloid and Interface Science*, 1998. **206**(1): p. 288–296.
[145] Gu, Y.G., Li, D.Q. and Cheng, P., A novel contact angle measurement technique by analysis of capillary rise profile around a cylinder (ACRPAC). *Colloids and Surfaces a-Physicochemical and Engineering Aspects*, 1997. **122**(1–3): p. 135–149.
[146] Wei, Q.F. *et al*., Dynamic wetting of fibers observed in an environmental scanning electron microscope. *Textile Research Journal*, 2003. **73**(6): p. 557–561.
[147] Tao, W.Y. and Collier, B.J., The Environmental Scanning Electron-microscope – A New Tool for Textile Studies. *Textile Chemist and Colorist*, 1994. **26**(2): p. 29–31.
[148] Hartland, S., *Surface and Interfacial Tension : Measurement, Theory, and Applications*. 2004, New York; Basel: Marcel Dekker.
[149] Rhee, H., Young, R.A. and Sarmadi, A.M., The Effect of Functional Finishes and Laundering on Textile Materials. 1. Surface Characteristics. *Journal of the Textile Institute*, 1993. **84**(3): p. 394–405.
[150] Herb, C.A., Buckner, J.L. and Overton, J.R., The Effect of Cross-sectional Geometry on the Accuracy of the Fiber-wetting Balance. *Journal of Colloid and Interface Science*, 1983. **94**(1): p. 14–24.
[151] Sauer, B.B. and Kampert, W.C., Influence of viscosity on forced and spontaneous spreading: Wilhelmy fiber studies including practical methods for rapid viscosity measurement. *Journal of Colloid and Interface Science*, 1998. **199**(1): p. 28–37.
[152] Wagner, H.D., Spreading of Liquid Droplets on Cylindrical Surfaces – accurate Determination of Contact-angle. *Journal of Applied Physics*, 1990. **67**(3): p. 1352–1355.
[153] Harnett, P.R. and Mehta, P.N., A Survey and Comparison of Laboratory Test Methods for Measuring Wicking. *Textile Research Journal*, 1984. **54**(7): p. 471–478.
[154] Rhee, H., Young, R.A. and Sarmadi, A.M., The Effect of Functional Finishes and Laundering on Textile Materials. 2. Characterization of Liquid Flow. *Journal of the Textile Institute*, 1993. **84**(3): p. 406–418.
[155] Perwuelz, A., Mondon, P. and Caze, C., Experimental study of capillary flow in yarns. *Textile Research Journal*, 2000. **70**(4): p. 333–339.
[156] Ferrero, F., Wettability measurements on plasma treated synthetic fabrics by capillary rise method. *Polymer Testing*, 2003. **22**(5): p. 571–578.
[157] Volkov, V.A., Bulushev, B.V. and Ageev, A.A., Determination of the capillary size and contact angle of fibers from the kinetics of liquid rise along the vertical samples of fabrics and nonwoven materials. *Colloid Journal*, 2003. **65**(4): p. 523–525.
[158] Ansari, N. and Kish, M.H., The wicking of water in yarn as measured by an electrical resistance technique. *Journal of the Textile Institute*, 2000. **91**(3): p. 410–419.
[159] Ito, H. and Muraoka, Y., Water Transport Along Textile Fibers as Measured by an Electrical Capacitance Technique. *Textile Research Journal*, 1993. **63**(7): p. 414–420.

[160] Hoffmann, K.H. and Schreiber, M., Computational physics : selected methods, simple exercises, serious applications. 1996, Berlin; New York: Springer.
[161] van Remoortere, P., et al., Wetting behavior of a Lennard–Jones system. *Journal of Chemical Physics*, 1999. **110**(5): p. 2621–2628.
[162] Manna, S.S., Herrmann, H.J. and Landau, D.P. A Stochastic Method to Determine the Shape of a Drop on a Wall. *Journal of Statistical Physics*, 1992. **66**(3–4): p. 1155–1163.
[163] Lukkarinen, A., Kaski, K. and Abraham, D.B., Mechanisms of Fluid Spreading – Ising Model Simulations. *Physical Review E*, 1995. **51**(3): p. 2199–2202.
[164] Advani, S.G. and Sozer, E.M., *Process Modeling in Composites Manufacturing*. Manufacturing engineering and materials processing. 2003, New York: Marcel Dekker.
[165] Fong, L. and Advani, S.G., Resin Transfer Molding, in *Handbook of Composites*, S.T. Peters, Editor. 1998, Chapman & Hall: London.
[166] Advani, S.G., *Flow and Rheology in Polymer Composites Manufacturing*. 1994, Amsterdam; New York: Elsevier.
[167] Kotomin, S.V. and Avdeev, N.N., Wetting of synthetic fibers by thermoplastic melts during capillary impregnation of filaments. *Colloid Journal*, 1999. **61**(3): p. 306–313.
[168] Kang, M.K., Lee, W.I. and Hahn, H.T., Formation of microvoids during resin-transfer molding process. *Composites Science and Technology*, 2000. **60**(12–13): p. 2427–2434.
[169] Dimitrovova, Z. and Advani, S.G., Mesolevel analysis of the transition region formation and evolution during the Liquid Composite Molding process. *Computers & Structures*, 2004. **82**(17–19): p. 1333–1347.
[170] Binetruy, C., Hilaire, B. and Pabiot, J., The influence of fiber wetting in resin transfer molding: Scale effects. *Polymer Composites*, 2000. **21**(4): p. 548–557.
[171] Binetruy, C., Hilaire, B. and Pabiot, J., The interactions between flows occurring inside and outside fabric tows during RTM. *Composites Science and Technology*, 1997. **57**(5): p. 587–596.
[172] Lekakou, C. and Bader, M.G., Mathematical modelling of macro- and micro-infiltration in resin transfer moulding (RTM). *Composites Part A-Applied Science and Manufacturing*, 1998. **29**(1–2): p. 29–37.
[173] Patel, N. and Lee, L.J., Effects of Fiber Mat Architecture on Void Formation and Removal in Liquid Composite Molding. *Polymer Composites*, 1995. **16**(5): p. 386–399.
[174] Parnas, R.S. *et al*., The Interaction between Microscopic and Macroscopic Flow in RTM Preforms. *Composite Structures*, 1994. **27**(1–2): p. 93–107.
[175] Spaid, M.A.A. and Phelan, F.R., Modeling void formation dynamics in fibrous porous media with the lattice Boltzmann method. *Composites Part A-Applied Science and Manufacturing*, 1998. **29**(7): p. 749–755.
[176] Larsson, R., Wysocki, M. and Toll, S., Process-modeling of composites using two-phase porous media theory. *European Journal of Mechanics A-Solids*, 2004. **23**(1): p. 15–36.
[177] Parnas, R.S., *Liquid Composite Molding*. 2000, Munich: Hanser Gardner Publications. 170.
[178] Coulter, J.P. and Guceri, S.I., Resin Impregnation During Composites Manufacturing – Theory and Experimentation. *Composites Science and Technology*, 1989. **35**(4): p. 317–330.
[179] Gutowski, T.G. *et al*., Consolidation Experiments for Laminate Composites. *Journal of Composite Materials*, 1987. **21**(7): p. 650–669.
[180] Gebart, B.R., Permeability of Unidirectional Reinforcements for RTM. *Journal of Composite Materials*, 1992. **26**(8): p. 1100–1133.
[181] Cai, Z. and Berdichevsky, A.L., An Improved Self-consistent Method for Estimating the Permeability of a Fiber Assembly. *Polymer Composites*, 1993. **14**(4): p. 314–323.
[182] Berdichevsky, A.L. and Cai, Z., Preform Permeability Predictions by Self-consistent Method and Finite-element Simulation. *Polymer Composites*, 1993. **14**(2): p. 132–143.
[183] Montgomery, S.M., Miller, B. and Rebenfeld, L., Spatial-distribution of Local Permeabilities in Fibrous Networks. *Textile Research Journal*, 1992. **62**(3): p. 151–161.
[184] Patel, N., Rohatgi, V. and Lee, L.J., Micro Scale Flow Behavior and Void Formation Mechanism During Impregnation through a Unidirectional Stitched Fiberglass Mat. *Polymer Engineering and Science*, 1995. **35**(10): p. 837–851.
[185] Chan, A.W. and Morgan, R.J. Tow Impregnation During Resin Transfer Molding of Bidirectional Nonwoven Fabrics. *Polymer Composites*, 1993. **14**(4): p. 335–340.
[186] Dungan, F.D. and Sastry, A.M., Saturated and unsaturated polymer flows: Microphenomena and modeling. *Journal of Composite Materials*, 2002. **36**(13): p. 1581–1603.
[187] Pillai, K.M., Governing equations for unsaturated flow through woven fiber mats. Part 1. Isothermal flows. *Composites Part A-Applied Science and Manufacturing*, 2002. **33**(7): p. 1007–1019.
[188] Pillai, K.A. and Munagavalasa, M.S., Governing equations for unsaturated flow through woven fiber mats. Part 2. Non-isothermal reactive flows. *Composites Part A-Applied Science and Manufacturing*, 2004. **35**(4): p. 403–415.
[189] Slade, J., Pillai, K.M. and Advani, S.G., Investigation of unsaturated flow in woven, braided and stitched fiber mats during mold-filling in resin transfer molding. *Polymer Composites*, 2001. **22**(4): p. 491–505.

[190] Chen, Y.T., Macosko, C.W. and Davis, H.T., Wetting of Fiber Mats for Composites Manufacturing 2. Air Entrapment Model. *Aiche Journal*, 1995. **41**(10): p. 2274–2281.
[191] Batch, G.L., Chen, Y.T. and Macosko, C.W., Capillary impregnation of aligned fibrous beds: Experiments and model. *Journal of Reinforced Plastics and Composites*, 1996. **15**(10): p. 1027–1051.
[192] Patel, N. and Lee, L.J., Modeling of void formation and removal in liquid composite molding 1. Wettability analysis. *Polymer Composites*, 1996. **17**(1): p. 96–103.
[193] Young, W.B., The effect of surface tension on tow impregnation of unidirectional fibrous preform in resin transfer molding. *Journal of Composite Materials*, 1996. **30**(11): p. 1191–1209.
[194] Chan, A.W. and Hwang, S.T., Modeling Nonisothermal Impregnation of Fibrous Media with Reactive Polymer Resin. *Polymer Engineering and Science*, 1992. **32**(5): p. 310–318.
[195] Young, W.B., 3–Dimensional Nonisothermal Mold Filling Simulations in Resin Transfer Molding. *Polymer Composites*, 1994. **15**(2): p. 118–127.
[196] Ngo, N.D. and Tamma, K.K. Non-isothermal '2-D flow/3-D thermal' developments encompassing process modelling of composites: Flow/thermal/cure formulations and validations. *International Journal for Numerical Methods in Engineering*, 2001. **50**(7): p. 1559–1585.
[197] Endruweit, A., Gehrig, S. and Ermanni, P., Mechanisms of hydrodynamically induced in-plane deformation of reinforcement textiles in resin injection processes. *Journal of Composite Materials*, 2003. **37**(18): p. 1675–1692.
[198] Acheson, J.A., Simacek, P. and Advani, S.G., The implications of fiber compaction and saturation on fully coupled VARTM simulation. *Composites Part A-Applied Science and Manufacturing*, 2004. **35**(2): p. 159–169.
[199] Lim, S.T. and Lee, W.I., An analysis of the three-dimensional resin-transfer mold filling process. *Composites Science and Technology*, 2000. **60**(7): p. 961–975.
[200] Mohan, R.V., Ngo, N.D. and Tamma, K.K., Three-dimensional resin transfer molding: Isothermal process modeling and explicit tracking of moving fronts for thick geometrically complex composites manufacturing applications - Part 1. *Numerical Heat Transfer Part A-Applications*, 1999. **35**(8): p. 815–838.
[201] Shojaei, A., Ghaffarian, S.R. and Karimian, S.M.H., Simulation of the three-dimensional non-isothermal mold filling process in resin transfer molding. *Composites Science and Technology*, 2003. **63**(13): p. 1931–1948.
[202] Shojaei, A., Ghaffarian, S.R. and Karimian, S.M.H., Three-dimensional process cycle simulation of composite parts manufactured by resin transfer molding. *Composite Structures*, 2004. **65**(3–4): p. 381–390.
[203] Young, W.B., Thermal Behaviors of the Resin and Mold in the Process of Resin Transfer Molding. *Journal of Reinforced Plastics and Composites*, 1995. **14**(4): p. 310–332.
[204] Chang, C.Y. and Hourng, L.W., Study on void formation in resin transfer molding. *Polymer Engineering and Science*, 1998. **38**(5): p. 809–818.
[205] Chang, C.Y. and Hourng, L.W., Numerical simulation for the transverse impregnation in resin transfer molding. *Journal of Reinforced Plastics and Composites*, 1998. **17**(2): p. 165–182.
[206] Chang, C.Y. and Shih, M.S., Numerical simulation on the void distribution in the fiber mats during the filling stage of RTM. *Journal of Reinforced Plastics and Composites*, 2003. **22**(16): p. 1437–1454.
[207] Golestanian, H. and El-Gizawy, A.S., Physical and numerical modeling of mold filling in resin transfer molding. *Polymer Composites*, 1998. **19**(4): p. 395–407.
[208] Henne, M. *et al*., A new kinetic and viscosity model for liquid composite molding simulations in an industrial environment. *Polymer Composites*, 2004. **25**(3): p. 255–269.
[209] Ngo, N.D. and Tamma, K.K., Computational developments for simulation based design: Multi-scale physics and flow/thermal/cure/stress modeling, analysis, and validation for advanced manufacturing of composites with complex microstructures. *Archives of Computational Methods in Engineering*, 2003. **10**(1–2): p. 3–206.
[210] Ngo, N.D. and Tamma, K.K., An integrated comprehensive approach to the modeling of resin transfer molded composite manufactured net-shaped parts. *Cmes-Computer Modeling in Engineering & Sciences*, 2004. **5**(2): p. 103–133.
[211] Ranganathan, S., Phelan, F.R. and Advani, S.G., A generalized model for the transverse fluid permeability in unidirectional fibrous media. *Polymer Composites*, 1996. **17**(2): p. 222–230.
[212] Young, W.B. and Lai, C.L., Analysis of the edge effect in resin transfer molding. *Composites Part a-Applied Science and Manufacturing*, 1997. **28**(9–10): p. 817–822.
[213] Belov, E.B. *et al*., Modelling of permeability of textile reinforcements: lattice Boltzmann method. *Composites Science and Technology*, 2004. **64**(7–8): p. 1069–1080.
[214] Spaid, M.A.A. and Phelan, F.R., Lattice Boltzmann methods for modeling microscale flow in fibrous porous media. *Physics of Fluids*, 1997. **9**(9): p. 2468–2474.
[215] Shih, M.S., Hourng, L.W. and Chang, C.Y., Random walk approach on the study of void distribution during the resin transfer molding process. *Journal of Reinforced Plastics and Composites*, 2004. **23**(6): p. 651–680.
[216] Zhong, W., Xing, M.Q. and Chen, S.C., A statistic model of mold filling through fibrous structures. *Journal of Composite Materials*, 2004. **38**(17): p. 1545–1557.

[217] Kuan, Y.D. and El-Gizawy, A.S., Numerical characterization of mold injection in resin transfer molding process. *Advances in Polymer Technology*, 2000. **19**(3): p. 173–179.
[218] Trochu, F. and Gauvin, R., Limitations of a Boundary-fitted Finite-difference Method for the Simulation of the Resin Transfer Molding Process. *Journal of Reinforced Plastics and Composites*, 1992. **11**(7): p. 772–786.
[219] Xue, X., Zhang, Y.B. and Hansen, P.N., Simulation and prediction of flow patterns in mold filling. *Transactions of Nonferrous Metals Society of China*, 2001. **11**(5): p. 743–747.
[220] Papathanasiou, T.D. and Lee, P.D., Morphological effects on the transverse permeability of arrays of aligned fibers. *Polymer Composites*, 1997. **18**(2): p. 242–253.
[221] Papathanasiou, T.D., On the effective permeability of square arrays of permeable fiber tows. *International Journal of Multiphase Flow*, 1997. **23**(1): p. 81–92.
[222] Um, M.K. and Lee, W.I., A Study on the Mold Filling Process in Resin Transfer Molding. *Polymer Engineering and Science*, 1991. **31**(11): p. 765–771.
[223] Um, M.K. and Lee, S.K., A study on the determination of in-plane permeability of fiber preforms. *Polymer Composites*, 1999. **20**(6): p. 771–779.
[224] Yoo, Y.E. and Lee, W.I., Numerical simulation of the resin transfer mold filling process using the boundary element method. *Polymer Composites*, 1996. **17**(3): p. 368–374.
[225] Chung, S.T. and Kwon, T.H., Coupled analysis of injection molding filling and fiber orientation, including in-plane velocity gradient effect. *Polymer Composites*, 1996. **17**(6): p. 859–872.
[226] Antonelli, D. and Farina, A., Resin transfer moulding: mathematical modelling and numerical simulations. *Composites Part a-Applied Science and Manufacturing*, 1999. **30**(12): p. 1367–1385.
[227] Dimitrovova, Z. and Faria, L., Finite element modeling of the resin transfer molding process based on homogenization techniques. *Computers & Structures*, 2000. **76**(1–3): p. 379–397.
[228] Han, K.H. and Im, Y.T., Numerical simulation of three-dimensional fiber orientation in injection molding including fountain flow effect. *Polymer Composites*, 2002. **23**(2): p. 222–238.
[229] Najmi, L.A. and Lee, D.Y., Modeling of Mold Filling Process for Powder Injection-molding. *Polymer Engineering and Science*, 1991. **31**(15): p. 1137–1148.
[230] Chung, S.T. and Kwon, T.H., Numerical-simulation of Fiber Orientation in Injection Molding of Short-fiber-reinforced Thermoplastics. *Polymer Engineering and Science*, 1995. **35**(7): p. 604–618.
[231] Pillai, K.M. and Advani, S.G., Numerical simulation of unsaturated flow in woven fiber preforms during the resin transfer molding process. *Polymer Composites*, 1998. **19**(1): p. 71–80.
[232] Simacek, P. and Advani, S.G., A numerical model to predict fiber tow saturation during liquid composite molding. *Composites Science and Technology*, 2003. **63**(12): p. 1725–1736.
[233] Dai, F.H., Zhang, B.M. and Du, S.Y., Analysis of upper- and lower-limits of fill time in resin transfer mold filling simulation. *Journal of Composite Materials*, 2004. **38**(13): p. 1115–1136.
[234] Shojaei, A., Ghaffarian, S.R. and Karimian, S.M.H., Numerical simulation of three-dimensional mold filling in resin transfer molding. *Journal of Reinforced Plastics and Composites*, 2003. **22**(16): p. 1497–1529.
[235] Kim, S.K., Opperer, J.G. and Daniel, I.M., Gas flow method for detecting local preform defects by inverse estimation of space-varying permeability. *Journal of Composite Materials*, 2003. **37**(15): p. 1367–1383.
[236] Shojaei, A., Ghaffarian, S.R. and Karimian, S.M.H., Numerical analysis of controlled injection strategies in resin transfer molding. *Journal of Composite Materials*, 2003. **37**(11): p. 1011–1035.
[237] Kim, B.Y., Nam, G.J. and Lee, J.W., Optimization of filling process in RTM using a genetic algorithm and experimental design method. *Polymer Composites*, 2002. **23**(1): p. 72–86.
[238] Mohan, R.V., Ngo, N.D. and Tamma, K.K., On a pure finite-element-based methodology for resin transfer mold filling simulations. *Polymer Engineering and Science*, 1999. **39**(1): p. 26–43.
[239] Lin, M., Hahn, H.T. and Huh, H., A finite element simulation of resin transfer molding based on partial nodal saturation and implicit time integration. *Composites Part A-Applied Science and Manufacturing*, 1998. **29**(5–6): p. 541–550.
[240] Wang, T.J., Wu, C.H. and Lee, L.J., Inplane Permeability Measurement and Analysis in Liquid Composite Molding. *Polymer Composites*, 1994. **15**(4): p. 278–288.
[241] Chick, J.P. *et al*., Material characterization for flow modeling in structural reaction injection molding. *Polymer Composites*, 1996. **17**(1): p. 124–135.
[242] Adams, K.L., Russel, W.B. and Rebenfeld, L., Radial Penetration of a Viscous Liquid into a Planar Anisotropic Porous Medium. *International Journal of Multiphase Flow*, 1988. **14**(2): p. 203–215.
[243] Wu, C.H., Wang, T.J. and Lee, L.J., Trans-plane Fluid Permeability Measurement and its Applications in Liquid Composite Molding. *Polymer Composites*, 1994. **15**(4): p. 289–298.
[244] Parnas, R.S., et al., Permeability characterization 1. A proposed standard reference fabric for permeability. *Polymer Composites*, 1995. **16**(6): p. 429–445.
[245] Amico, S.C. and Lekakou, C., Axial impregnation of a fiber bundle. Part 1: Capillary experiments. *Polymer Composites*, 2002. **23**(2): p. 249–263.
[246] Amico, S. and Lekakou, C., An experimental study of the permeability and capillary pressure in resin-transfer moulding. *Composites Science and Technology*, 2001. **61**(13): p. 1945–1959.

[247] Chen, Y.T., Davis, H.T. and Macosko, C.W., Wetting of Fiber Mats for Composites Manufacturing 1. Visualization Experiments. *Aiche Journal*, 1995. **41**(10): p. 2261–2273.
[248] Richardson, M.O.W. and Zhang, Z.Y., Experimental investigation and flow visualisation of the resin transfer mould filling process for non-woven hemp reinforced phenolic composites. *Composites Part A-Applied Science and Manufacturing*, 2000. **31**(12): p. 1303–1310.
[249] Bickerton, S. *et al*., Design and application of actively controlled injection schemes for resin-transfer molding. *Composites Science and Technology*, 2001. **61**(11): p. 1625–1637.
[250] Schwab, S.D., Levy, R.L. and Glover, G.G., Sensor system for monitoring impregnation and cure during resin transfer molding. *Polymer Composites,* 1996. **17**(2): p. 312–316.
[251] Skordos, A.A., Karkanas, P.I. and Partridge, I.K., A dielectric sensor for measuring flow in resin transfer moulding. *Measurement Science & Technology*, 2000. **11**(1): p. 25–31.
[252 Seo, J.W. and Lee, W.L. A Model of the Resin Impregnation in Thermoplastic Composites. *Journal of Composite Materials*, 1991. **25**(9): p. 1127–1142.
[253] Babu, B.Z. and Pilla, K.M., Experimental investigation of the effect of fiber-mat architecture on the unsaturated flow in liquid composite molding, *Journal of Composite Materials*, 2004, **38**(1), p. 57–59.
[254] Suits, L.D., The Use of Geotextiles in Transportation Facilities. *ACS Symposium Series*, 1991. **457**: p. 358–375.
[255] Barksdale, R.D., Geotextiles and Geogrids in Pavements - Introduction. *Geotextiles and Geomembranes*, 1989. **8**(3): p. 161–163.
[256] Elsharief, A.M. and Lovell, C.W., A probabilistic retention criterion for nonwoven geotextiles. *Geotextiles and Geomembranes*, 1996. **14**(11): p. 601–617.
[257] Christopher, B.R. and Fischer, G.R., Geotextile Filtration Principles, Practices and Problems. *Geotextiles and Geomembranes*, 1992. **11**(4–6): p. 337–353.
[258] Bhatia, S.K. and Smith, J.L., Geotextile characterization and pore-size distribution: Part I. A review of manufacturing processes. *Geosynthetics International*, 1996. **3**(1): p. 85–105.
[259] Watson, P.D.J. and John, N.W.M. Geotextile filter design and simulated bridge formation at the soil–geotextile interface. *Geotextiles & Geomembranes*, 1999. **17**(5): p. 265–280.
[260] Bhatia, S.K. and Smith, J.L., Geotextile characterization and pore-size distribution: Part II. A review of test methods and results. *Geosynthetics International*, 1996. **3**(2): p. 155–180.
[261] Bhatia, S.K., Smith, J.L. and Christopher, B.R., Geotextile characterization and pore-size distribution: Part III. Comparison of methods and application to design. *Geosynthetics International*, 1996. **3**(3): p. 301–328.
[262] Fourie, A.B. and Addis, P., The effect of in-plane tensile loads on the retention characteristics of geotextiles. *Geotechnical Testing Journal*, 1997. **20**(2): p. 211–217.
[263] Vermeersch, O.G. and Mlynarek. J., Determination of the pore size distribution of nonwoven geotextiles by a modified capillary flow porometry technique. in *Proceedings of the 1995 Symposium on Recent Developments in Geotextile Filters and Prefabricated Drainage Geocomposites*. Denver, CO, USA: ASTM Special Technical Publication. No. 1281 May 1996. ASTM, Conshohocken, PA, USA.
[264] Bhatia, S.K. and Smith, J.L., Application of the Bubble Point Method to the Characterization of the Pore-size Distribution of Geotextiles. *Geotechnical Testing Journal*, 1995. **18**(1): p. 94–105.
[265] Fischer, G.R., Holtz, R.D. and Christopher, B.R., Evaluating geotextile pore structure, in *Recent developments in geotextile filters and prefabricated drainage geocomposites*, S.K. Bhatia and L.D. Suits, Editors. 1996, American Society for Testing Materials, ASTM STP 1281. p. 3–18.
[266] Fischer, G.R., Holtz, R.D. and Christopher, B.R., Evaluating geotextile pore structure, in *Proceedings of the 1995 Symposium on Recent Developments in Geotextile Filters and Prefabricated Drainage Geocomposites*. Denver, CO, USA: ASTM Special Technical Publication. No. 1281, May 1996. ASTM, Conshohocken, PA, USA.
[267] Bhatia, S.K. and Smith, J.L., Comparative Study of Bubble Point Method and Mercury Intrusion Porosimetry Techniques for Characterizing the Pore Size Distribution of Geotextiles. *Geotextiles and Geomembranes*, 1994. **13**(10): p. 679–702.
[268] Elsharief, A.M. and Lovell. C.W., Determination and comparisons of the pore structure of nonwoven geotextiles, in *Proceedings of the 1995 Symposium on Recent Developments in Geotextile Filters and Prefabricated Drainage Geocomposites*. Denver, CO, USA: ASTM Special Technical Publication No. 1281, May 1996. ASTM, Conshohocken, PA, USA.
[269] Aydilek, A.H., Oguz, S.H. and Edil, T.B., Digital image analysis to determine pore opening size distribution of nonwoven geotextiles. *Journal of Computing in Civil Engineering*, 2002. **16**(4): p. 280–290.
[270] Aydilek, A.H. and Edil, T.B., Evaluation of woven geotextile pore structure parameters using image analysis. *Geotechnical Testing Journal*, 2004. **27**(1): p. 99–110.
[271] Chin, Y.M. and Nikraz. H.R., Empirical approach to filtration criteria for non-woven geotextiles, in *Proceedings of the 1995 Symposium on Recent Developments in Geotextile Filters and Prefabricated Drainage Geocomposites*. Denver, CO, USA: ASTM Special Technical Publication No. 1281, May 1996. ASTM, Conshohocken, PA, USA.
[272] Lee, I.M., Kim, J.H. and Reddi, L.N., Clogging phenomena of the residual soil-geotextile filter system. *Geotechnical Testing Journal*, 2002. **25**(4): p. 379–390.

[273] Palmeira, E.M. and Gardoni, M.G., Drainage and filtration properties of non-woven geotextiles under confinement using different experimental techniques. *Geotextiles and Geomembranes*, 2002. **20**(2): p. 97–115.
[274] Barlow, K. and Nash, D., Investigating structural stability using the soil water characteristic curve. *Australian Journal of Experimental Agriculture*, 2002. **42**(3): p. 291–296.
[275] Cabral, A.R. *et al*., Determination of the soil water characteristic curve of highly compressible materials: Case study of pulp and paper by-product. *Geotechnical Testing Journal*, 2004. **27**(2): p. 154–162.
[276] Rassam, D.W. and Williams, D.J., A dynamic method for determining the soil water characteristic curve for coarse-grained soils. *Geotechnical Testing Journal*, 2000. **23**(1): p. 67–71.
[277] Iryo, T. and Rowe, R.K., On the hydraulic behavior of unsaturated nonwoven geotextiles. *Geotextiles and Geomembranes*, 2003. **21**(6): p. 381–404.
[278] Knight, M.A. and Kotha, S.M., Measurement of geotextile-water characteristic curves using a controlled outflow capillary pressure cell. *Geosynthetics International*, 2001. **8**(3): p. 271–282.
[279] Klute, A., Water retention: laboratory methods, in *Methods of soil analysis, Part. 1, Agronomy monograph No. 9, 2nd Edition*, A.L. Page, R.H. Miller, and D.R. Keeney, Editors. 1986, American Society of Agronomy–Soil Science of America: Madison. p. 635–662.
[280] Stormont, J.C. and Ramos, R., Characterization of a fiberglass geotextile for unsaturated in-plane water transport. *Geotechnical Testing Journal*, 2004. **27**(2): p. 214–219.
[281] Fannin, R.J., Vaid, Y.P. and Shi, Y.C., A Critical Evaluation of the Gradient Ratio Test. *Geotechnical Testing Journal*, 1994. **17**(1): p. 35–42.
[282] Fischer, G.R., Mare, A.D. and Holtz, R.D., Influence of procedural variables on the gradient ratio test. *Geotechnical Testing Journal*, 1999. **22**(1): p. 22–31.
[283] Palmeira, E.M., Fannin, R.J. and Vaid, Y.P., A study on the behaviour of soil-geotextile systems in filtration tests. *Canadian Geotechnical Journal*, 1996. **33**(6): p. 899–912.
[284] Christopher, B.R. and Wood. P.D., Evaluation of the U.S. army corps of engineer gradient ratio test, in *Second International Conference on Geotextiles*. 1982. Las Vegas.
[285] Rao, G.V., Gupta, K.K. and Pradhan, M.P.S., Long-term filtration behaviour of soil-geotextile system. *Geotechnical Testing Journal*, 1992. **15**(3): p. 238–247.
[286] Hameiri, A. and Fannin, R.J., A cyclic gradient ratio test device. *Geotechnical Testing Journal*, 2002. **25**(3): p. 266–276.
[287] Luettich, S.M., Giroud, J.P. and Bachus, R.C., Geotextile Filter Design Guide. *Geotextiles and Geomembranes*, 1992. **11**(4–6): p. 355–370.
[288] Chew, S.H. *et al*., Erosion stability of punctured geotextile filters subjected to cyclic wave loadings – a laboratory study. *Geotextiles and Geomembranes*, 2003. **21**(4): p. 221–239.
[289] Shan, H.Y., Wang, W.L. and Chou, T.C., Effect of boundary conditions on the hydraulic behavior of geotextile filtration system. *Geotextiles and Geomembranes*, 2001. **19**(8): p. 509–527.
[290] Gardoni, M.G. and Palmeira, E.M., Microstructure and pore characteristics of synthetic filters under confinement. *Geotechnique*, 2002. **52**(6): p. 405–418.
[291] Aydilek, A.H. and Edil, T.B., Filtration performance of woven geotextiles with wastewater treatment sludge. *Geosynthetics International*, 2002. **9**(1): p. 41–69.
[292] Narejo, D.B., Opening size recommendations for separation geotextiles used in pavements. *Geotextiles and Geomembranes*, 2003. **21**(4): p. 257–264.
[293] Palmeira, E.M. and Gardoni, M.G., The influence of partial clogging and pressure on the behaviour of geotextiles in drainage systems. *Geosynthetics International*, 2000. **7**(4–6): p. 403–431.
[294] Fannin, R.J. and Sigurdsson, O., Field observations on stabilization of unpaved roads with geosynthetics. *Journal of Geotechnical Engineering-ASCE*, 1996. **122**(7): p. 544–553.
[295] Al-Qadi, I.L. and Appea, A.K., Eight-year field performance of secondary road incorporating geosynthetics at subgrade-base interface. *Soil Mechanics* 2003, 2003(1849): p. 212–220.
[296] Wilson-Fahmy, R.F., Koerner, G.R. and Koerner, R.M., Geotextile filter design critique, in *Proceedings of the 1995 Symposium on Recent Developments in Geotextile Filters and Prefabricated Drainage Geocomposites*. Denver, CO, USA: ASTM Special Technical Publication, No. 1281 May 1996. ASTM, Conshohocken, PA, USA.
[297] Corbet, S. and King, J., eds. *Geotextiles in filtration and drainage*. 1993, Thomas Telford: London.
[298] van Genuchten, M.T., A closed form equation predicting the hydraulic conductivity of unsaturated soils. *Soil Science Society of America Journal*, 1980. **44**: p. 892–898.
[299] Sillers, W.S. and Fredlund, D.G., Statistical assessment of soil-water characteristic curve models for geotechnical engineering. *Canadian Geotechnical Journal*, 2001. **38**(6): p. 1297–1313.
[300] Fayer, M.J. and Simmons, C.S., Modified soil water retention functions for all matric suctions. *Water Resources Research*, 1995. **31**: p. 1233–1238.
[301] Fredlund, D.G. and Xing, A.Q., Equations for the Soil–Water Characteristic Curve. *Canadian Geotechnical Journal*, 1994. **31**(4): p. 521–532.
[302] Fredlund, D.G., Xing, A.Q. and Huang, S.Y., Predicting the Permeability Function for Unsaturated Soils Using the Soil–Water Characteristic Curve. *Canadian Geotechnical Journal*, 1994. **31**(4): p. 533–546.

[303] Putnam, D.D. and Burns, M.A., Predicting the filtration of noncoagulating particles in depth filters. *Chemical Engineering Science*, 1997. **52**(1): p. 93–105.
[304] Leichkis, I.M., Filtration on Precoat Filters as a Markov Process. *Chemical Engineering and Processing*, 1993. **32**(5): p. 301–310.
[305] Destephen, J.A. and Choi, K.J., Modelling of filtration processes of fibrous filter media. *Separations Technology*, 1996. **6**(1): p. 55–67.
[306] Brown, R.C., *Air filtration: An integrated approach to the theory and applications of fibrous filters*. 1st ed. 1993, Oxford; New York: Pergamon Press.
[307] Hinds, W.C., *Aerosol technology: properties, behavior, and measurement of airborne particles*. 1982, New York: J. Wiley.
[308] Wang, C.S., Electrostatic forces in fibrous filters – a review. *Powder Technology*, 2001. **118**(1–2): p. 166–170.
[309] Kirsh, V.A., The effect of van der Waals' forces on aerosol filtration with fibrous filters. *Colloid Journal*, 2000. **62**(6): p. 714–720.
[310] Kirsh, V.A., Gravitational deposition of aerosol particles on a fibrous filter with account for the effect of van der Waals force. *Colloid Journal*, 2001. **63**(1): p. 68–73.
[311] Raynor, P.C. and Leith, D., The influence of accumulated liquid on fibrous filter performance. *Journal of Aerosol Science*, 2000. **31**(1): p. 19–34.
[312] Chernyakov, A.L. and Kirsch, A.A., Growth in hydrodynamic resistance of aerosol fibrous filter during deposition of liquid dispersed phase. *Colloid Journal*, 1999. **61**(6): p. 791–796.
[313] Gradon, L., Influence of Electrostatic Interactions and Slip Effect on Aerosol Filtration Efficiency in Fiber Filters. *Industrial & Engineering Chemistry Research*, 1987. **26**(2): p. 306–311.
[314] Thorpe, A. and Brown, R.C., Performance of electrically augmented fibrous filters, measured with monodisperse aerosols. *Aerosol Science and Technology*, 2003. **37**(3): p. 231–245.
[315] Emi, H., Fundamentals of Particle Separation and Air Filters. *Journal of Aerosol Science*, 1991. **22**: p. S727–S730.
[316] Lee, K.W. and Liu, B.Y.H., Experimental Study of Aerosol Filtration by Fibrous Filters., *Aerosol Science and Technology*, 1982. **1**(1): p. 35–46.
[317] Liu, Z.G. and Wang, P.K., Pressure drop and interception efficiency of multifiber filters. *Aerosol Science and Technology*, 1997. **26**(4): p. 313–325.
[318] Maschio, C. and De Arruda, A.C.F., Modeling of the efficiency of fibrous filters through numerical simulation and X-ray tomography. *Advanced Powder Technology*, 2001. **12**(3): p. 311–329.
[319] Schweers, E. and Loffler, F., Realistic Modeling of the Behavior of Fibrous Filters through Consideration of Filter Structure. *Powder Technology*, 1994. **80**(3): p. 191–206.
[320] Gougeon, R., Boulaud, D. and Renoux, A., Comparison of data from model fiber filters with diffusion, interception and inertial deposition models. *Chemical Engineering Communications*, 1996. **151**: p. 19–39.
[321] Shapiro, M., An analytical model for aerosol filtration by nonuniform filter media. *Journal of Aerosol Science*, 1996. **27**(2): p. 263–280.
[322] Shapiro, M., Kettner, I.J. and Brenner, H., Transport Mechanics and Collection of Submicrometer Particles in Fibrous Filters. *Journal of Aerosol Science*, 1991. **22**(6): p. 707–722.
[323] Liu, Z.L.G. and Wang, P.K., Numerical investigation of viscous flow fields around multifiber filters. *Aerosol Science and Technology*, 1996. **25**(4): p. 375–391.
[324] Dhaniyala, S. and Liu, B.Y.H., Theoretical modeling of filtration by nonuniform fibrous filters. *Aerosol Science and Technology*, 2001. **34**(2): p. 170–178.
[325] Dhaniyala, S. and Liu, B.Y.H., An asymmetrical, three-dimensional model for fibrous filters. *Aerosol Science and Technology*, 1999. **30**(4): p. 333–348.
[326] Quintard, M. and Whitaker, S., Aerosol filtration: An analysis using the method of volume averaging. *Journal of Aerosol Science*, 1995. **26**(8): p. 1227–1255.
[327] Destephen, J.A. and Choi, K.J., Modelling of filtration processes of fibrous filter media. *Separations Technology*, 1996. **6**(1): p. 55–67.
[328] Cao, Y.H., Cheung, C.S. and Yan, Z.D., Numerical study of an electret filter composed of an array of staggered parallel rectangular split-type fibers. *Aerosol Science and Technology*, 2004. **38**(6): p. 603–618.
[329] Asgharian, B. and Cheng, Y.S., The filtration of fibrous aerosols. *Aerosol Science and Technology*, 2002. **36**(1): p. 10–17.
[330] Podgorski, A., Gradon, L. and Grzybowski, P., Theoretical Study on Deposition of Flexible and Stiff Fibrous Aerosol Particles on a Cylindrical Collector. *Chemical Engineering Journal and the Biochemical Engineering Journal*, 1995. **58**(2): p. 109–121.
[331] Lange, R., Fissan, H. and Schmidt-Ott, A., Predicting the collection efficiency of agglomerates in fibrous filters. *Particle & Particle Systems Characterization*, 1999. **16**(2): p. 60–65.
[332] Kwon, S.B., Kim, H.T. and Lee, K.W., Analytic solutions to diffusional deposition of polydisperse aerosols in fibrous filters. *Aerosol Science and Technology*, 2002. **36**(6): p. 742–747.
[333] Kim, H.T. *et al*., Diffusional filtration of polydispersed aerosol particles by fibrous and packed-bed filters. *Filtration & Separation*, 2000. **37**(6): p. 37–42.

[334] Karadimos, A. and Ocone, R., The effect of the flow field recalculation on fibrous filter loading: a numerical simulation. *Powder Technology*, 2003. **137**(3): p. 109–119.
[335] Podgorski, A., Balazy, A. and Trzeciak, T.M., Deposition of fractal-like aerosol aggregates in fibrous filters. *Inzynieria Chemiczna I Procesowa*, 2004. **25**(3): p. 1521–1526.
[336] Contal, P. *et al*., Clogging of fibre filters by submicron droplets. Phenomena and influence of operating conditions. *Journal of Aerosol Science*, 2004. **35**(2): p. 263–278.
[337] Thomas, D. *et al*., Clogging of fibrous filters by solid aerosol particles – Experimental and modelling study. *Chemical Engineering Science*, 2001. **56**(11): p. 3549–3561.
[338] Calle, S. *et al*., Changes in the performances of filter media during clogging and cleaning cycles. *Annals of Occupational Hygiene*, 2001. **45**(2): p. 115–121.
[339] Kirsch, V.A., Method for the calculation of an increase in the pressure drop in an aerosol filter on clogging with solid particles. *Colloid Journal*, 1998. **60**(4): p. 439–443.
[340] Chernyakov, A.L., The influence of fluctuations on the efficiency of aerosol particle collection with fibrous filters. *Colloid Journal*, 2004. **66**(3): p. 355–366.
[341] Przekop, R., Moskal, A. and Gradon, L., Lattice-Boltzmann approach for description of the structure of deposited particulate matter in fibrous filters. *Journal of Aerosol Science*, 2003. **34**(2): p. 133–147.
[342] Masselot, A. and Chopard, B., A lattice Boltzmann model for particle transport and deposition. *Europhysics Letters*, 1998. **42**(3): p. 259–264.
[343] Chopard, B. and Masselot, A., Cellular automata and lattice Boltzmann methods: A new approach to computational fluid dynamics and particle transport. *Future Generation Computer Systems*, 1999. **16**(2–3): p. 249–257.
[344] Elshobokshy, M.S., Alsanea, S.A. and Adnan, A.M., Computer-simulation of Monodisperse Aerosol Collection in Fibrous Filters. *Aerosol Science and Technology*, 1994. **20**(2): p. 149–160.
[345] Wake, D. *et al*., Performance of respirator filters and surgical masks against bacterial aerosols. *Journal of Aerosol Science*, 1997. **28**(7): p. 1311–1329.
[346] Qian, Y.G. *et al*., Particle reentrainment from fibrous filters. *Aerosol Science and Technology*, 1997. **27**(3): p. 394–404.
[347] Dhaniyala, S. and Liu, B.Y.H., Experimental investigation of local efficiency variation in fibrous filters. *Aerosol Science and Technology*, 2001. **34**(2): p. 161–169.
[348] Alonso, M. and Endo, Y., Dispersion of aerosol particles undergoing Brownian motion. *Journal of Physics A-Mathematical and General*, 2001. **34**(49): p. 10745–10755.
[349] Chen, C.C. *et al*., Experimental study on the loading characteristics of needlefelt filters with micrometer-sized monodisperse aerosols. *Aerosol Science and Technology*, 2001. **34**(3): p. 262–273.
[350] Penicot, P. *et al*., Clogging of HEPA fibrous filters by solid and liquid aerosol particles: An experimental study. *Filtration & Separation*, 1999. **36**(2): p. 59–64.
[351] Kopp, C., Petzold, A. and Niessner, R., Investigation of the specific attenuation cross-section of aerosols deposited on fiber filters with a polar photometer to determine black carbon. *Journal of Aerosol Science*, 1999. **30**(9): p. 1153–1163.
[352] Clark, W.R., Hemodialyzer membranes and configurations: A historical perspective. *Seminars in Dialysis*, 2000. **13**(5): p. 309–311.
[353] Sueoka, A. and Takakura, K., Hollow Fiber Membrane Application for Blood Treatment. *Polymer Journal*, 1991. **23**(5): p. 561–571.
[354] Tzanakakis, E.S., *et al*., Extracorporeal tissue engineered liver-assist devices. *Annual Review of Biomedical Engineering*, 2000. **2**: p. 607–632.
[355] Klein, E., Ward, R.A. and Lacey, R.E., Membrane processes: dialysis and electrodialysis, in *Handbook of Separation Process Technology*, R.W. Rousseau, Editor. 1987, Wiley: New York. p. 954–981.
[356] Noordwijk, J.V., Dialysing for life: The development of the artificial kidney. 2001, Dordrecht; Boston: Kluwer Academic Publishers. xii, 114.
[357] Fissell, W.H. *et al*., The role of a bioengineered artificial kidney in renal failure. *Bioartificial Organs III: Tissue Sourcing, Immunoisolation, and Clinical Trials*, 2001. **944**: p. 284–295.
[358] Saito, A., Development of bioartificial kidneys. *Nephrology*, 2003. **8**: p. S10–S15.
[359] Dixit, V. and Gitnick, G., The bioartificial liver: State-of-the-art. *European Journal of Surgery*, 1998. **164**: p. 71–76.
[360] Nagamori, S. *et al*., Developments in bioartificial liver research: Concepts, performance, and applications. *Journal of Gastroenterology*, 2000. **35**(7): p. 493–503.
[361] Zhang, Y.H. Singh, V.K. and Yang, V.C., Novel approach for optimizing the capacity and efficacy of a protamine filter for clinical extracorporeal heparin removal. *Asaio Journal*, 1998. **44**(5): p. M368–M373.
[362] Dierickx, P.W. *et al.*, Mass transfer characteristics of artificial lungs. *Asaio Journal*, 2001. **47**(6): p. 628–633.
[363] Dierickx, P.W., de Wachter, D.S. and Verdonck, P.R., Two-dimensional finite element model for oxygen transfer in cross-flow hollow fiber membrane artificial lungs. *International Journal of Artificial Organs*, 2001. **24**(9): p. 628–635.
[364] Tatsumi, E. *et al*., Preprimed artificial lung for emergency use. *Artificial Organs*, 2000. **24**(2): p. 108–113.

[365] Wickramasinghe, S.R., Garcia, J.D. and Han, B.B., Mass and momentum transfer in hollow fibre blood oxygenators. *Journal of Membrane Science*, 2002. **208**(1–2): p. 247–256.
[366] Chae, S.Y., Kim, S.W. and Bae, Y.H., Bioactive polymers for biohybrid artificial pancreas. *Journal of Drug Targeting*, 2001. **9**(6): p. 473–484.
[367] Morita, S., An experimental study on the bioartificial pancreas using polysulfone hollow fibers. *Japanese Journal of Transplantation*, 1998. **33**(3): p. 169–180.
[368] Boyd, R.F. *et al*., Solute washout experiments for characterizing mass transport in hollow fiber immunoisolation membranes. *Annals of Biomedical Engineering*, 1998. **26**(4): p. 618–626.
[369] Velez, G.M. *et al*., Mass transfer in hollow fiber-type artificial pancreas devices. *Faseb Journal*, 1997. **11**(3): p. 1676–1676.
[370] Brotherton, J.D. and Chau, P.C., Modeling of axial-flow hollow fiber cell culture bioreactors. *Biotechnology Progress*, 1996. **12**(5): p. 575–590.
[371] Rios, G.M. *et al*., Progress in enzymatic membrane reactors – a review. *Journal of Membrane Science*, 2004. **242**(1–2): p. 189–196.
[372] Marrot, B. *et al*., Industrial wastewater treatment in a membrane bioreactor: A review. *Environmental Progress*, 2004. **23**(1): p. 59–68.
[373] Visvanathan, C., Ben Aim, R. and Parameshwaran, K., Membrane separation bioreactors for wastewater treatment. *Critical Reviews in Environmental Science and Technology*, 2000. **30**(1): p. 1–48.
[374] Patzer, J.F., Oxygen consumption in a hollow fiber bioartificial liver – revisited. *Artificial Organs*, 2004. **28**(1): p. 83–98.
[375] Labecki, M., Piret, J.M. and Bowen, B.D., 2-Dimensional Analysis of Fluid Flow in Hollow Fiber Modules. *Chemical Engineering Science*, 1995. **50**(21): p. 3369–3384.
[376] Niranjan, S.C. *et al*., Analysis of Factors Affecting Gas Exchange in Intravascular Blood-Gas Exchanger. *Journal of Applied Physiology*, 1994. **77**(4): p. 1716–1730.
[377] Schonberg, J.A. and Belfort, G., Enhanced Nutrient Transport in Hollow Fiber Perfusion Bioreactors – A Theoretical Analysis. *Biotechnology Progress*, 1987. **3**(2): p. 80–89.
[378] Chresand, T.J., Gillies, R.J. and Dale, B.E., Optimum Fiber Spacing in a Hollow Fiber Bioreactor. *Biotechnology and Bioengineering*, 1988. **32**(8): p. 983–992.
[379] Kelsey, L.J., Pillarella, M.R. and Zydney, A.L., Theoretical Analysis of Convective Flow Profiles in a Hollow Fiber Membrane Bioreactor. *Chemical Engineering Science*, 1990. **45**(11): p. 3211–3220.
[380] Moussy, Y., Bioartificial kidney. I. Theoretical analysis of convective flow in hollow fiber modules: Application to a bioartificial hemofilter. *Biotechnology and Bioengineering*, 2000. **68**(2): p. 142–152.
[381] Labecki, M., Piret, J.M. and Bowen, B.D., Effects of free convection on three-dimensional protein transport in hollow-fiber bioreactors. *Aiche Journal*, 2004. **50**(8): p. 1974–1990.
[382] Eloot, S., *et al*., Computational flow modeling in hollow-fiber dialyzers. *Artificial Organs*, 2002. **26**(7): p. 590–599.
[383] Dierickx, P.W.T., De Wachter, D. and Verdonck, P.R., Blood flow around hollow fibers. *International Journal of Artificial Organs*, 2000. **23**(9): p. 610–617.
[384] Thundyil, M.J. and Koros, W.J., Mathematical modeling of gas separation permeators for radial crossflow, countercurrent, and cocurrent hollow fiber membrane modules. *Journal of Membrane Science*, 1997. **125**(2): p. 275–291.
[385] Tsuji, M. and Sakai, K., Theoretical comparison of filtration by the renal glomerulus and artificial membranes. *Asaio Journal*, 1999. **45**(1): p. 98–103.
[386] Chatterjee, A. *et al*., Modeling of a radial flow hollow fiber module and estimation of model parameters using numerical techniques. *Journal of Membrane Science*, 2004. **236**(1): p. 1–16.
[387] Secchi, A.R., Wada, K. and Tessaro, I.C., Simulation of an ultrafiltration process of bovine serum albumin in hollow-fiber membranes. *Journal of Membrane Science*, 1999. **160**(2): p. 255–265.
[388] Dulong, J.L. *et al*., A novel model of solute transport in a hollow-fiber bioartificial pancreas based on a finite element method. *Biotechnology and Bioengineering*, 2002. **78**(5): p. 576–582.
[389] Hilke, R. *et al*., The duomodule. Part 1: Hydrodynamic investigations. *Journal of Membrane Science*, 1999. **154**(2): p. 183–194.
[390] Crowder, R.O. and Cussler, E.L., Mass transfer in hollow-fiber modules with non-uniform hollow fibers. *Journal of Membrane Science*, 1997. **134**(2): p. 235–244.
[391] Nonner, W. and Eisenberg, B., Electrodiffusion in ionic channels of biological membranes. *Journal of Molecular Liquids*, 2000. **87**(2–3): p. 149–162.
[392] Crozier, P.S. *et al*., Molecular dynamics simulation of continuous current flow through a model biological membrane channel. *Physical Review Letters*, 2001. **86**(11): p. 2467–2470.
[393] Saiz, L., Bandyopadhyay, S. and Klein, M.L., Towards an understanding of complex biological membranes from atomistic molecular dynamics simulations. *Bioscience Reports*, 2002. **22**(2): p. 151–173.
[394] Arnold, A., Paris, M. and Auger, M., Anomalous diffusion in a gel-fluid lipid environment: A combined solid-state NMR and obstructed random-walk perspective. *Biophysical Journal*, 2004. **87**(4): p. 2456–2469.
[395] Weiss, M., Hashimoto, H. and Nilsson, T., Anomalous protein diffusion in living cells as seen by fluorescence correlation spectroscopy. *Biophysical Journal*, 2003. **84**(6): p. 4043–4052.

[396] Milon, S. *et al*., Factors influencing fluorescence correlation spectroscopy measurements on membranes: simulations and experiments. *Chemical Physics*, 2003. **288**(2–3): p. 171–186.
[397] Saxton, M.J., Single-particle tracking: The distribution of diffusion coefficients. *Biophysical Journal*, 1997. **72**(4): p. 1744–1753.
[398] Kier, L.B., Cheng, C.K. and Testa, B., Cellular automata models of biochemical phenomena. *Future Generation Computer Systems*, 1999. **16**(2–3): p. 273–289.
[399] Li, M. *et al*., An experimental investigation of hollow fiber flow in dialyzer. *International Journal of Nonlinear Sciences and Numerical Simulation*, 2002. **3**(3–4): p. 261–265.
[400] Klein, E. *et al*., Transport and Mechanical Properties of Hemodialysis Hollow Fibers. *Journal of Membrane Science*, 1976. **1**(4): p. 371–396.
[401] Sakai, K., Determination of Pore-size and Pore-size Distribution.2. Dialysis Membranes. *Journal of Membrane Science*, 1994. **96**(1–2): p. 91–130.
[402] Sakai, K. *et al*., Determination of Pore Radius of Hollow-fiber Dialysis Membranes Using Tritium-labeled Water. *Journal of Chemical Engineering of Japan*, 1988. **21**(2): p. 207–210.
[403] Kanamori, T. *et al*., An Improvement on the Method of Determining the Solute Permeability of Hollow-fiber Dialysis Membranes Photometrically Using Optical Fibers and Comparison of the Method with Ordinary Techniques. *Journal of Membrane Science*, 1994. **88**(2–3): p. 159–165.
[404] Ohmura, T. *et al*., New method of determining the solute permeability of hollow-fiber dialysis membranes by means of laser lights traveling along optic fibers. *ASAIO Transactions*, 1989. **35**(3): p. 601–603.
[405] Zhao, C.S., Zhou, X.S. and Yue, Y.L., Determination of pore size and pore size distribution on the surface of hollow-fiber filtration membranes: A review of methods. *Desalination*, 2000. **129**(2): p. 107–123.
[406] Nakao, S., Determination of Pore-size and Pore-size Distribution.3 Filtration Membranes. *Journal of Membrane Science*, 1994. **96**(1–2): p. 131–165.
[407] Khayet, M., Khulbe, K.C. and T., Matsuura, Characterization of membranes for membrane distillation by atomic force microscopy and estimation of their water vapor transfer coefficients in vacuum membrane distillation process. *Journal of Membrane Science*, 2004. **238**(1–2): p. 199–211.
[408] Khayet, M. and Matsuura, T., Determination of surface and bulk pore sizes of flat-sheet and hollow-fiber membranes by atomic force microscopy, gas permeation and solute transport methods. *Desalination*, 2003. **158**(1–3): p. 57–64.
[409] Hayama, M., Kohori, F. and Sakai, K., AFM observation of small surface pores of hollow-fiber dialysis membrane using highly sharpened probe. *Journal of Membrane Science*, 2002. **197**(1–2): p. 243–249.
[410] Feng, C.Y. *et al*., Structural and performance study of microporous polyetherimide hollow fiber membranes made by solvent-spinning method. *Journal of Membrane Science*, 2001. **189**(2): p. 193–203.
[411] Sakai, K. *et al*., Comparison of Methods for Characterizing Microporous Membranes for Plasma Separation. *Journal of Membrane Science*, 1987. **32**(1): p. 3–17.
[412] Ishikiriyama, K. *et al*., Pore-size Distribution Measurements of Poly(Methyl Methacrylate) Hydrogel Membranes for Artificial Kidneys Using Differential Scanning Calorimetry. *Journal of Colloid and Interface Science*, 1995. **173**(2): p. 419–428.
[413] Lee, Y. *et al*., Modified liquid displacement method for determination of pore size distribution in porous membranes. *Journal of Membrane Science*, 1997. **130**(1–2): p. 149–156.
[414] Peirce, F.T., Tensile Tests for Cotton Yarns, Part V: The Weakest Link Theorems on the Strength of Long and Composite Specimens. *J. Textile Inst*., 1926. **17**: p. T355–368.
[415] Brochard, F., Spreading of Liquid Drops on Thin Cylinders – the Manchon Droplet Transition. *Journal of Chemical Physics*, 1986. **84**(8): p. 4664–4672.
[416] Young, T., An Essay on the Cohesion of Fluids. *Philosophical Transactions of the Royal Society of London*, 1805. **95**: p. 65–87.
[417] Marmur, A., The lotus effect: Superhydrophobicity and metastability. *Langmuir*, 2004. **20**(9): p. 3517–3519.
[418] Rosario, R. *et al*., Lotus effect amplifies light-induced contact angle switching. *Journal of Physical Chemistry B*, 2004. **108**(34): p. 12640–12642.
[419] Otten, A. and Herminghaus, S., How plants keep dry: A physicist's point of view. *Langmuir*, 2004. **20**(6): p. 2405–2408.
[420] Oner, D. and McCarthy, T.J., Ultrahydrophobic surfaces. Effects of topography length scales on wettability. *Langmuir*, 2000. **16**(20): p. 7777–7782.
[421] Noga, G.J., Knoche, M., Wolter, M. and Barthlott, W., Changes in leaf micromorphology induced by surfactant application. *Ang. Bot.*, 1987. **61**: p. 521–528.
[422] Jiang, L., Zhao, Y. and Zhai, J., A lotus-leaf-like superhydrophobic surface: A porous microsphere/nanofiber composite film prepared by electrohydrodynamics. *Angewandte Chemie-International Edition*, 2004. **43**(33): p. 4338–4341.
[423] Holloway, P.J., Surface factors affecting the wetting of leaves. *Pestic. Sci.*, 1970. **1**: p. 156–163.
[424] Feng, L. *et al*., Super-hydrophobic surfaces: From natural to artificial. *Advanced Materials*, 2002. **14**(24): p. 1857–1860.
[425] Extrand, C.W., Criteria for ultralyophobic surfaces. *Langmuir*, 2004. **20**(12): p. 5013–5018.

[426] Barthlott, W. and Neinhuis, C., Self-cleaning biological surfaces. *Planta*, 1997. **202**: p. 18.
[427] Ball, P., Engineering – Shark skin and other solutions. *Nature*, 1999. **400**(6744): p. 507.
[428] Anon., Lessons from lotus leaves. *Chemical & Engineering News*, 2004. **82**(23): p. 30.
[429] Chaikin, P.M. and Lubensky T.C., Principles of Condensed Matter Physics. 1995, Cambridge: Cambridge University Press.
[430] Ising, E., A contribution to the theory of ferromagnetism. *Z. Physik.*, 1925: p. 253.
[431] Cipra, B.A., An Introduction to the Ising Model. *Amer. Math. Monthly*, 1987. **94**: p. 937–959.
[432] McCoy, B.M. and Wu, T.T., The two-dimensional Ising model. 1973, Cambridge: Harvard University Press.
[433] Albano, E.V. *et al*., Critical Wetting in the Square Ising Model with a Boundary Field. *Journal of Statistical Physics*, 1990. **61**(1–2): p. 161–178.
[434] Binder, K. and Landau, D.P., Wetting Versus Layering near the Roughening Transition in the 3-Dimensional Ising Model. *Physical Review B*, 1992. **46**(8): p. 4844-4854.
[435] Miga, S. *et al*., Ageing in the ferroic random-field Ising model system strontium–barium niobate. *Physical Review B*, 2004. **70**(13).
[436] Albano, E.V., Binder, K. and Paul, W., Monte Carlo studies of d = 2 Ising strips with long-range boundary fields. *Journal of Physics-Condensed Matter*, 2000. **12**(12): p. 2701–2723.
[437] Albano, E.V. *et al*., Study of the dynamical approach to the interface localization–delocalization transition of the confined Ising model. *Journal of Physics-Condensed Matter*, 2004. **16**(23): p. 3853–3867.
[438] Anisimov, M.A. *et al*., Shape of cross-over between mean-field and asymptotic critical behavior in a three-dimensional Ising lattice. *Physics Letters A*, 1999. **261**(1–2): p. 89–93.
[439] Binder, K., How Monte Carlo simulations can clarify complex problems in statistical physics. *International Journal of Modern Physics B*, 2001. **15**(9): p. 1193–1211.
[440] Binder, K., Applications of Monte Carlo methods to statistical physics. *Reports on Progress in Physics*, 1997. **60**(5): p. 487–559.
[441] Binder, K., Ferrenberg, A.M. and Landau, D.P., Wetting and Capillary Condensation of Lattice Gases in Thin-film Geometry. *Berichte Der Bunsen-Gesellschaft–Physical Chemistry Chemical Physics*, 1994. **98**(3): p. 340–345.
[442] Binder, K., Landau, D. and Muller, M., Monte Carlo studies of wetting, interface localization and capillary condensation. *Journal of Statistical Physics*, 2003. **110**(3–6): p. 1411–1514.
[443] Binder, K. and Schroder, K., Phase-transitions of a Nearest-neighbor Ising Model Spin Glass. *Physical Review B*, 1976. **14**(5): p. 2142–2152.
[444] Frisch, H.L., Kimball, J.C. and Binder, K., Surface critical behaviour near the uniaxial Lifshitz point of the axial next-nearest-neighbour Ising model. *Journal of Physics-Condensed Matter*, 2000. **12**(1): p. 29–42.
[445] Morgenstern, I., Binder, K. and Hornreich, R.M., Two-Dimensional Ising Model in Random Magnetic Fields. *Physical Review B*, 1981. **23**(1): p. 287–297.
[446] Parry, A.O., Evans, R. and Binder, K., Critical Amplitude Ratios for Critical Wetting in 3 Dimensions – Observation of Nonclassical Behavior in the Ising Model. *Physical Review B*, 1991. **43**(13): p. 11535–11538.
[447] Patrykiejew, A. and Binder, K., Dynamics of Multilayer Adsorption – A Monte-Carlo Simulation. *Surface Science*, 1992. **273**(3): p. 413–426.
[448] Schmid, F. and Binder, K., Modeling Order–Disorder and Magnetic Transitions in Iron Aluminum Alloys. *Journal of Physics–Condensed Matter*, 1992. **4**(13): p. 3569–3588.
[449] Lukas, D., Glazyrina, E. and Pan, N., Computer simulation of liquid wetting dynamics in fiber structures using the Ising model. *Journal of the Textile Institute*, 1997. **88**(2): p. 149–161.
[450] Lukas, D. and Pan, N., Wetting of a fiber bundle in fibrous structures. *Polymer Composites*, 2003. **24**(3): p. 314–322.
[451] Zhong, W., Ding, X. and Tang, Z.L., Modeling and analyzing liquid wetting in fibrous assemblies. *Textile Research Journal*, 2001. **71**(9): p. 762–766.
[452] Zhong, W., Ding, X. and Tang, Z.L., Statistical modeling of liquid wetting in fibrous assemblies., *Acta Physico-Chimica Sinica*, 2001. **17**(8): p. 682–686.
[453] Abraham, D.B. and Newman, C.M., Lecture Notes in Physics. *Lecture Notes in Physics*, 1988. **354**: p. 13.
[454] Israelachvili, J.N., *Intermolecular & Surface Forces*. 1985, London: Academic Press.
[455] Zhong, W. and Pan, N., *A* computer simulation of single fiber pull out process in a composite. *Journal of Composite Materials*, 2003. **37**(21): p. 1951–1969.
[456] Zhong, W., Pan, N. and Lukas, D., Stochastic modelling of tear behaviour of coated fabrics. *Modelling and Simulation in Materials Science and Engineering*, 2004. **12**(2): p. 293–309.
[457] Gu *et al*., *Angewandte Chemie*, International Edition, http://www.sciencenews.org/articles/20030301/fob4.asp